DANISH METEOROLOGICAL INSTITUTE

SCIENTIFIC REPORT

02-14

Energetic Electron Precipitation Studied by Atmospheric X-Rays

By

Tina Christensen

COPENHAGEN 2002

Danish Meteorological Institute, Solar-Terrestrial Physics Division,
Lyngbyvej 100, DK-2100 Copenhagen Ø, Denmark

ISSN-Nr. 0905-3263
ISSN-Nr. 1399-1949 (Online)
ISBN-Nr. 87-7478-468-4

Energetic Electron Precipitation Studied by Atmospheric X-Rays

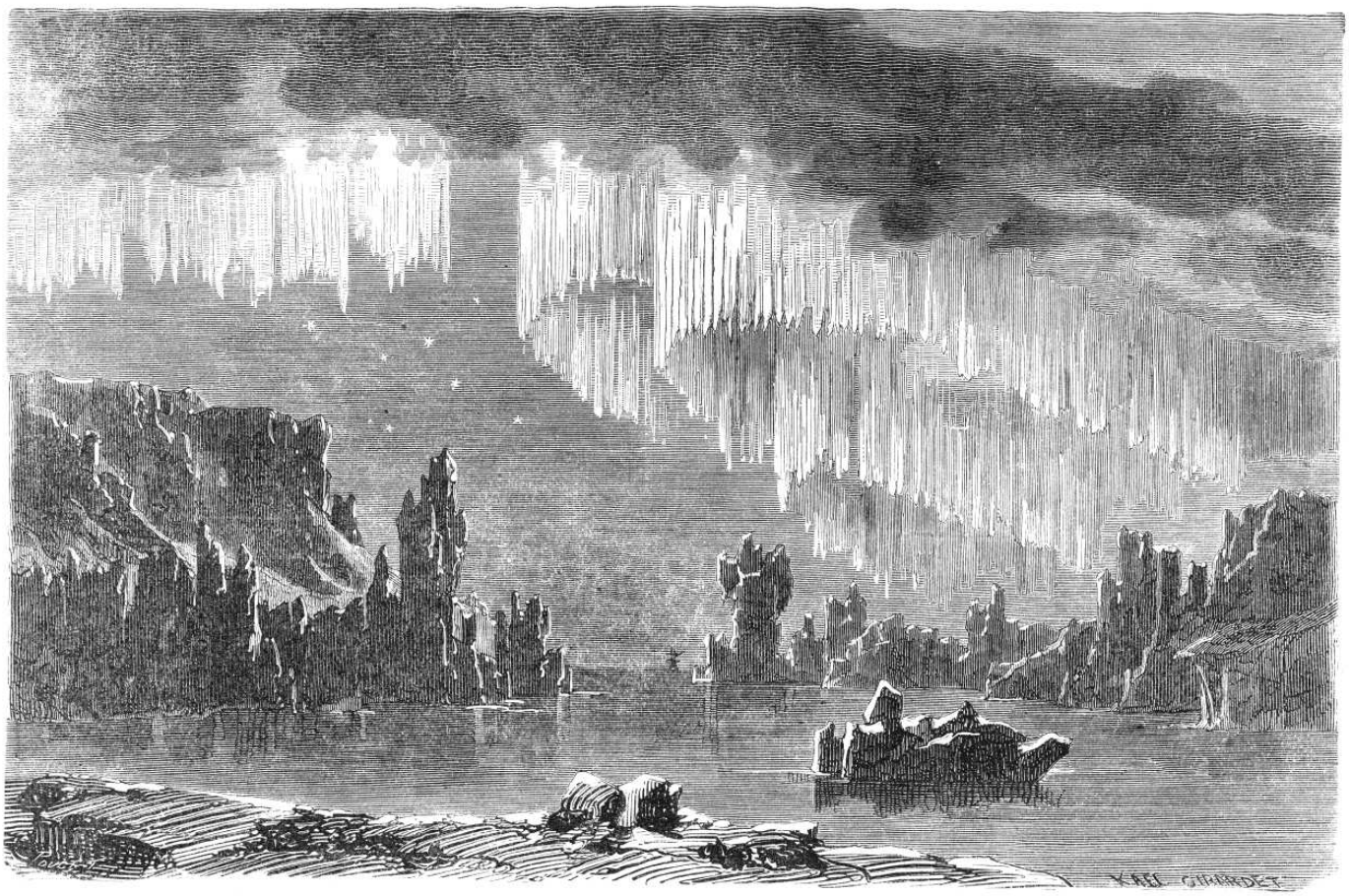

Tina Christensen
Ph.D. Thesis
Niels Bohr Institute for Astronomy, Physics and Geophysics
Faculty of Science
Copenhagen University

The research was carried out at
Solar-Terrestrial Physics Division
Danish Meteorological Institute

The cover illustration is from Paulsen (1879).

Keep me from going to sleep too soon
Or if I go to sleep too soon
Come wake me up. Come any hour
of night. Come whistling up the road
Stomp on the porch. Bang in the door
Make me get out of bed and come
And let you in and light a light.
Tell me the northern lights are on
And make me look. Or tell me clouds
Are doing something to the moon.
See that I see. Talk to me
'Till I'm half as wide awake
As you are.

Robert Francis

Contents

Acknowledgements

I gratefully acknowledge the easy access to a multitude of data sources from satellites as well as ground-based installations provided through CDAWeb (Coordinated Data Analysis Web) by NASA Goddard Space Flight Center and the principle investigators of the respective instruments. Likewise I gratefully acknowledge the web pages of NASA's National Space Science Data Center providing access to model runs of Tsyganenko's geomagnetic models and calculations of corrected geomagnetic coordinates.

Magnetometer data used in the equivalent drift maps were compiled by Peter Stauning and data were provided by Børre Holmeslet, Auroral Observatory, Tromsø Norway, Lorne McKee, Geological Survey of Canada and Ole Rasmussen and Børge Pedersen, Danish Meteorological Institute and WDC-C1. WIND data were obtained from CDAWeb and provided by R. Lepping at NASA/GSFC (Magnetic Field Investigation) and R. Lin at UC Berkeley (3D Plasma Analyzer). LANL energetic particle data were provided by G. Reeves, Los Alamos National Laboratory, USA. Geotail data were obtained from CDAWeb and provided by S. Kokubun at STELAB, Nagoya University, Japan. The final hourly D_{st} index was provided by WDC-C2 for geomagnetism, Kyoto University, Japan. The K_p index was provided by GeoForschungsZentrum Potsdam, Germany via WDC-C2, Kyoto, Japan.

I would like to thank my supervisors Klaus Mosegaard at the Geophysical Department of the Niels Bohr Institute at the University of Copenhagen and Peter Stauning at the Solar-Terrestrial Physics Department of the Danish Meteorological Institute. Peter Stauning originally employed me on a research grant with the project title 'Atmospheric X-ray Investigations' and suggested that this project could be a Ph.D. study. He subsequently obtained a grant from Forskerakademiet for this purpose, supported by Klaus Mosegaard.

Throughout my stay at University of Bergen, Norway, in January 2000 I met great hospitality from staff and students at the Space Physics Department. I would

like to specially thank Elisabeth Thorsen and Arve Aksnes for PIXIE data processing at this occasion, and Johan Stadsnes and Nikolai Østgaard for fruitful discussions.

During my four-month sojourn in the spring of 2001 at the Institute for Physical Science and Technology, University of Maryland, College Park, USA, I received great hospitality from Professor Ted Rosenberg. I am grateful for the discussions of my work in which also Dan Detrick participated. I thank Jim Etter for providing data plots and imaging riometer data presentation software.

In June 2001 I spent a week at NASA Goddard Space Flight Center in Greenbelt, Maryland. I would like to express my sincere thanks to Nikolai Østgaard for many rewarding and inspiring discussions and for providing processed PIXIE data and deduced electron spectra. I am greatly indebted to Rich Vondrak for inviting me to Goddard and for partaking in discussions of my research project and providing valuable input.

I would like to thank Glynn Germany at Center for Space Plasma, Aeronomy, and Astrophysics Research, University of Alabama in Huntsville, USA, for providing processed Polar/UVI data and for deriving electron spectra.

I am very grateful for the model calculations provided by Dan Detrick and Arve Aksnes of expected instrument response based on incident electron spectra.

I thank Regner Trampedach for making his bibliography style files for LaTeX available.

I am extremely grateful for the good service provided by May-Britt Raarup Bundsgaard and Elisabeth M. Boelskifte at the well-stocked library at DMI.

Special thanks go to Lars Tøffner-Clausen, Kim Bisgaard and Freddy Christiansen at the Solar-Terrestrial Physics Division at the Danish Meteorological Institute for numerous advice on UNIX and IDL, and for weird and wonderful discussions about life in general and science in particular.

I would like to express my deep thanks to my family and friends for support and patience throughout this project. And to Jakob Grue Simonsen for being Jakob; for being witty, warm and wonderful.

I acknowledge financial support from the Danish Meteorological Institute and research grants from Forskerakademiet and ESA følgeforskning.

Preface

In this thesis the remote sensing technique of atmospheric X-rays is used to study energetic electron precipitation. A deconvolution scheme for deriving energy spectra of precipitating electrons is presented and validated. When this work was initiated it was with the possible prospect of a 2003 launch of a Danish Earth-observing micro satellite flying an X-ray imager. In the end this satellite was given third priority through the proposal review of the Danish Small Satellite Programme. The instrument design has been continued, but so far no alternative launch platform has been identified by the principal investigator, Torsten Neubert. Utilizing the X-ray inversion technique presented in this thesis such a mission would constitute a powerful tool for monitoring energetic electron precipitation and deriving ionospheric effects such as conductivity changes and energy deposition, as well as obtaining information about magnetospheric source regions and processes.

The case study which is presented in this work demonstrates how energetic electron precipitation events characterized by atmospheric X-rays can provide information about processes taking place in the magnetotail and in the coupling region between the magnetosphere and ionosphere. Such special cases can help constrain substorm models and magneto-hydrodynamic models of the magnetosphere.

X-rays have the advantage that they can be studied day and night, since they are not influenced by sunlight, airglow or overcast conditions. The only drawback is the low X-ray production rates which challenge the detector designs to compromise between spectral, spatial and temporal resolution. Apart from a few K-shell emission lines at low energies, X-rays are generated solely by energetic electrons and hence are not subject to contaminating emissions from precipitating protons, as are other wavelength regimes.

I have striven to make main parts of this thesis accessible to the general public intrigued by space physics. Thus the historical account and the description of the

solar-terrestrial environment given in the first two chapters should be of broad interest, and this goes to some extent also for the introduction to the important instruments and information sources available to the space physicists given in the third chapter. The later chapters describing the main aspects of research that I have carried out during this project are necessarily somewhat more technical.

The opening chapter of this thesis is a historical introduction to the aurora and the field of solar-terrestrial physics. Instead of a chronological review of the numerous imaginative theories about the cause of the aurora I have only included those statements that have stood the test of time. The account is based on encyclopedic entries as well as Kivelson & Russell (1995), Hargreaves (1992) and Golub & Pasachoff (2001) in addition to the in-text references.

In Chapter 2 an introduction is given to the solar-terrestrial environment, starting at the Sun and following the energy flux through the solar wind to the magnetosphere and further into the ionosphere. The spectacular disturbances of the system, geomagnetic storms and substorms are described. In addition to the references in the text the following general references were used: Kivelson & Russell (1995), Hargreaves (1992), Schunk & Nagy (2000), Parks (1991) and Rees (1989).

Chapter 3 presents different important ground-based instruments as well as several satellite missions and space-borne instruments, many of which have contributed data to this work, particularly the imaging riometers in Kangerlussuaq, Iqaluit and South Pole and the global X-ray and UV imagers on the Polar satellite, PIXIE and UVI.

In Chapter 4 is described a deconvolution technique for deducing spectra of the precipitating electrons from observed X-ray spectra. The method developed in this work is an improvement of previous methods and it was validated using X-ray observations from the Polar Ionospheric X-ray Imaging Experiment on the Polar satellite. Comparison with ground-based data from the imaging riometer in Kangerlussuaq was performed for further verification of the reliability of the procedure which could become an important way of monitoring energetic electron precipitation in combination with future X-ray missions, e.g. in connection with space weather initiatives.

A major part of the research I have conducted during this project, reported in Chapter 5, is the study of a transient and localized energetic electron precipitation event which gave rise to intense X-ray emissions at high geomagnetic latitude. This event, which was most likely caused by a plasma flow burst from a transient magnetic reconnection event in the magnetotail enhanced by an electron accelerating mechanism above the ionosphere, can help to shed light on the problematic

magnetosphere-ionosphere coupling in current magnetospheric models.

Summary and conclusion of the thesis is given in Chapter 6.

Appendix A covers the most widely used coordinate systems in ionospheric and magnetospheric physics today.

In Appendix B a selection of the most useful and widespread geomagnetic indices are presented. These are diagnostics of different ionospheric or magnetospheric phenomena such as the intensity of substorms, geomagnetic storms and the global level of disturbance.

Appendix C provides a list of the publications and presentations I have made during this project. This includes two independent papers utilizing data from the Ørsted satellite that I did not find room to cover properly in this thesis.

Finally in Appendix D a summary of the thesis is given in Danish.

This document was prepared with LaTeX 2$_\varepsilon$ (Kopka & Daly 1995) using Times Roman.

Tina Christensen

Chapter 1

A brief history of the Sun-Earth connection

Long before the cause of the aurora could be known, these majestic lights were observed by men who regarded them as related to the spiritual world. Eskimos in Greenland and Canada saw the northern lights as the abode of the deceased, and thought the flickering of the aurora were the dead trying to contact their living relatives. Some native North Americans thought the aurora was a connection with the spiritual world. Others thought it was the feasts of warriors and shamans residing further north. And for some it was the sign that their creator was watching and guarding them.

In superstitious Europe the aurora, as other rare phenomena of the firmament, were often seen as a bad omen, a sign of evil times and hardship to come.

The Norse whom one should think would have had plenty experience with the northern lights do not give many accounts to support this notion. Authors and translators of the nineteenth century have interpreted descriptions of the Valkyries in the Edda as associated with aurora, but interpreted from a modern point of view there are very few indications of northern lights in the Edda (Brekke & Egeland 1980).

The encyclopedia-like Norwegian work The King's Mirror, probably written before 1250 (Brekke & Egeland 1980), is the first to use the term northern lights. It seems that aurora were not well-known to the Norwegians of the time, but were known from voyages to Greenland. Likely the auroral oval was positioned differently then (Brekke & Egeland 1980) due to the changeable nature of the internal geomagnetic field which causes the wandering of the magnetic poles over time.

Reports of aurora occurring in Denmark are known from the meteorological

journal (1582–1597) kept by Tycho Brahe during his sojourn in Uraniborg on the Island of Hven and from Ole Rømer's illustrations of aurora seen over Copenhagen on three occasions in 1707 (Silverman 1980; Brekke & Egeland 1979).

Galileo Galilei was apparently the one to coin the Latin term aurora borealis (northern dawn). This description can seem inappropriate when one knows that the dominant colour of the aurora is yellow-green, but at latitudes far south of the northern auroral zone the aurora will be in the form of diffuse red light on the northern sky.

The history of science is replete with imaginative explanations of the aurora, and only few of the early attempts hit close to the mark. The English astronomer Edmond Halley suggested in the early eighteenth century that the aurora was ordered by the direction of the magnetic field. In 1733 the French philosopher de Mairan published a book about the northern lights in which he proposed an association between sunspots and the aurora. This suggestion of an extra-terrestrial origin was much disputed, but still signified an important change in the way of thinking. The link between geomagnetic and auroral studies grew stronger.

When Galileo Galilei in the early seventeenth century directed the newly invented telescope towards the heavens he studied among other objects the dark areas on the solar disc: the sunspots. After Galilei followed a few decades of very few sunspots, the Maunder minimum, and the periodicity of the sunspot number was not discovered until 1843 by the German amateur astronomer Heinrich Schwabe who conducted sunspot measurements through 25 years, 1825–1850. Since that time the sunspot number has been recorded continuously.

Meanwhile the connection between geomagnetic and auroral activity had become firmly established. George Graham in 1722 observed that the compass is always in motion. The Swedish scientist Anders Celsius wrote an important treatise on his numerous auroral observations and in 1740 confirmed that the magnetic field varies. He encouraged the thorough measurements of the movement of a magnetic needle faithfully conducted by Olof Peter Hiorter who month after month made 24 hourly readings a day of the magnetic variations. From the ensuing extensive dataset he discovered the diurnal variation of the geomagnetic field, and in 1741 discovered the correlation between geomagnetic variations and auroral activity.

In 1773 the southern auroral counterpart, the aurora australis, was reported by captain James Cook.

The Danish professor of science Hans Christian Ørsted in 1820 fortuitously discovered that when currents were turned on in a conductor close to a compass

needle the latter would move. There had to be a relationship between magnetic fields and electric currents. This inspired research efforts across Europe and led the German mathematician Carl Friedrich Gauss to speculate that even though the atmosphere, as it was known, was not a conducting medium, currents flowing in the upper atmosphere were somehow still responsible for the aurora.

Through the first half of the nineteenth century a network of magnetometers was established which became increasingly global in coverage as it spread to British colonies. From the data from four stations around the world Edward Sabine in 1851 discovered that geomagnetic disturbances vary in intensity over the years in correlation with the sunspot cycle.

With the publication in 1873 of James Clerk Maxwell's famous four equations, currents and magnetism were inadvertently tied to each other. Balfour Stewart wrote an article on terrestrial magnetism in Encyclopaedia Britannica in 1882 in which he was led by the established correlation between geomagnetic disturbances and the solar cycle to conclude that the Sun must be responsible for turning the atmosphere into a conducting medium.

The link to the Sun was further established when Richard Carrington and a simultaneous observer on September 1, 1859 saw a solar flare. At the same time in London geomagnetic disturbances were recorded which were caused by the ionospheric effects of the impact of a great excess of solar UV and X-ray photons from the flare. A mere 18 hours later one of the strongest magnetic storms ever recorded broke out.

At the very dawn of the twentieth century, in 1901, G. Marconi successfully transmitted radio signals from Cornwall, England, across the Atlantic ocean to Newfoundland, Canada. The following year A. E. Kennelly and O. Heaviside independently suggested that a presence of free electrical charges in the upper atmosphere had reflected the radio waves and enabled the transatlantic transmission. That same year the first physical theory of the ionosphere was proposed by Oliver Lodge in a concise letter to Nature about Marconi's results:

> The observed effect, which if confirmed is very interesting, seems to me to be due to the conductivity, and consequent partial opacity, of air, under the influence of ultra-violet solar radiation.
>
> No doubt electrons will be given off from matter [...] in the solar beams; and the presence of these will convert the atmosphere into a feeble conductor.
>
> (Lodge 1902).

In the following decades much was learned about the ionosphere from radio wave remote sensing techniques.

1902 was also the year where the Norwegian science professor Kristian Birkeland set out on his third polar expedition during which he gathered data on magnetic perturbations associated with aurora which led him to propose in 1908 that electric currents flowed along magnetic field lines during aurora. These Birkeland currents were a bit too imaginative for most of the scientific world, and due to lack of evidence the idea lay dormant until the era of artificial satellites.

The Swedish physicist and astronomer Anders Jonas Ångström in the nineteenth century had been the first to study the spectrum of the aurora, and he concluded that it was emitted by a hot gas. He measured the clear yellow-green line at 557.7 nm (or in his own units 5577 Å), but was unable to identify the emitter. Decades later Norwegian professor Lars Vegard measured and identified many of the auroral lines, and also discovered the proton aurora, but the source of the dominant yellow-green emission was still elusive because the conditions in the upper atmosphere were so different from those in the laboratories where reference lines were measured. After precise measurements by H. Babcock in 1923, John McLennan was able to ascribe the emission to a forbidden transition in atomic oxygen.

In the first half of the previous century the Sun-Earth connection was not yet well described. German-born British physicist Frederick Alexander Lindemann pointed out that particle beams from the Sun would have to have equal representation of positive and negative charges. This concept of a plasma inspired British mathematician and solar physicist Sydney Chapman and his co-workers J. Bartels and V. C. A. Ferraro to their ground-breaking work in the 1930s on the interaction between the solar wind and the magnetosphere.

Until the early 1950s it was believed that radiation pressure from the solar light was what made comet tails always point away from the Sun, but calculations by the German astrophysicist Ludwig Bierman contravened this. He suggested in 1951 the existence of a steady high-speed outflow of charged particles from the Sun, as opposed to the intermittent plasma streams in the geomagnetic storm models of Chapman and Ferraro. A never ceasing flow could explain both the direction of comet tails and the persistent weak aurora with its associated geomagnetic field variations. The theory gained credibility when Chapman in 1957 made calculations of the great extent of the solar corona and American physicist Eugene Newman Parker was able to reconcile this with Bierman's outflow theory when he showed that the corona will expand outward continually. Parker called the

phenomenon the solar wind, but it was not widely accepted until it was physically detected by satellites in the 1960s.

American physicist John R. Winckler performed pioneering observations with instruments mounted on balloons. He studied cosmic rays and discovered X-rays and γ-rays associated with solar flares. In the early 1950s there had been scientific rocket flights conducted by the American astrophysicist James Van Allen detecting energetic electrons in the Arctic and Antarctic ionosphere. One unexpected discovery of Winckler's was that the aurora can be accompanied by X-ray emissions from such energetic electrons (Winckler & Peterson 1957; Winckler et al. 1958). This observation was done in 1957 at the start of the 18 month world-wide scientific effort to collect data on the terrestrial environment known as the International Geophysical Year.

1957 was also the year where the Soviet Union took the world in general and the United States in particular by surprise by launching the first artificial satellite, Sputnik 1, into orbit around the world. The following year the first successful US satellite, Explorer 1, was launched, and enabled Van Allen, with some help from a graduate student, to detect the belts of trapped radiation. Soon also the interplanetary medium was probed by spacecraft.

The advent of space-based platforms for instruments ensured many discoveries and great advances in ionospheric and magnetospheric research over the following decades, evolving and refining the picture of the solar-terrestrial environment to the view we hold today in which there is still room for modifications and improvements.

Chapter 2

The solar-terrestrial environment

The amazing and awe-inspiring aurora arises from the interaction between the solar wind and the Earth's magnetosphere. In the interaction energy is transferred to the magnetospheric system. This will initiate processes in the magnetosphere which accelerate the plasma particles inhabiting these regions. When the energized particles enter the upper atmosphere their interaction with atmospheric constituents gives rise to the light emissions that are the aurora. The charged particles are led by the magnetic field-lines to high-latitude regions. Thus the aurora occurs in two circumpolar bands: the aurora borealis in the northern hemisphere and the aurora australis in the southern.

This chapter is an account of the regions and properties of the solar-terrestrial environment, outlining the main concepts and providing the background for the study of atmospheric X-rays which follows in Chapters 4 and 5.

2.1 The solar wind

More than light is emitted from the Sun. That much became clear about half a century ago, and was finally proved when solar wind particles were measured by spacecraft in the 1960s. The solar corona is so hot that the plasma cannot be contained by gravity and the corona expands outward continuously. The expansion is radial and supersonic. Magnetic flux is embedded in the outflowing plasma constituting the solar wind. The magnetic field-lines are dragged out radially by the plasma, but because they are rooted at one end on the rotating Sun they will form a spiral pattern (the Parker spiral) in the ecliptic plane, see Fig. 2.1. The spiral is being wound tighter and tighter at longer radial distances. At the Earth's

orbit the angle between the field and a radial line is close to 45°. At this distance the solar wind speed is about 450 km/s.

The temperature of the corona just above the solar surface is about two million K. In comparison the effective (black body) temperature of the Sun is 5700 K. In a plasma heat is conducted very efficiently, and at the distance of the Earth's orbit the temperature of the solar wind is about 120000 K. When contemplating these high temperatures one should keep in mind that the solar wind is very tenuous with some 5-10 protons per cm^3 at the Earth's orbit. Thus the energy density is not as overwhelming as the high temperatures might suggest.

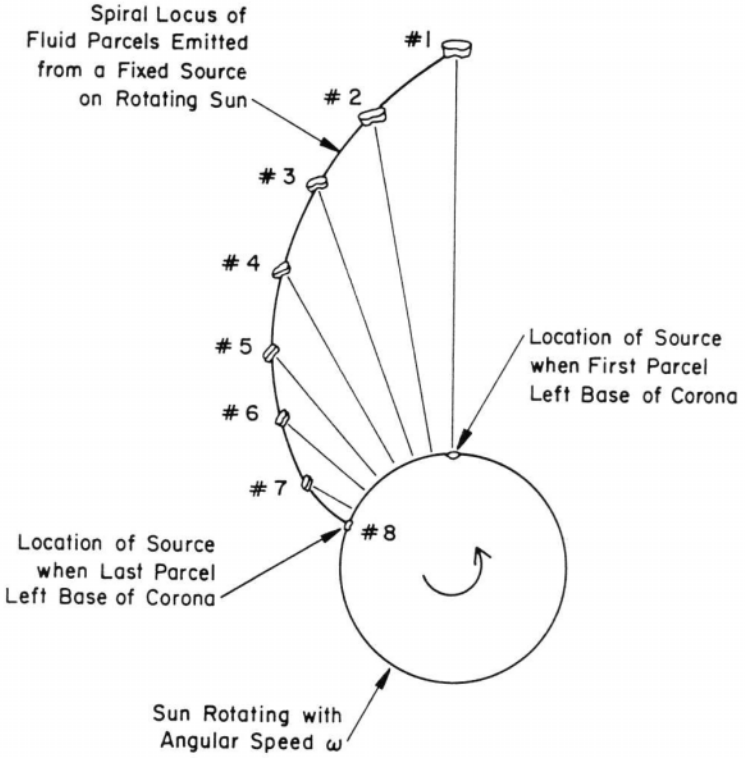

Figure 2.1: **Formation of the Parker spiral.** Plasma moves radially outward from the Sun with constant velocity while the source region at the base of the corona rotates with the Sun. This gives rise to a spiral structure of the associated flux tube. (Figure 4.5 of Kivelson & Russell (1995)).

Explaining coronal heating is still a somewhat elusive affair. Detailed theoretical description of a magnetized plasma is no small undertaking. However, it is widely believed that the magnetic field plays a vital role in coronal heating, although different processes could well be responsible for the heating in different

regions of the highly dynamic and inhomogeneous corona.

Observing the Sun with satellite-borne X-ray imagers reveals protruding loop-like structures and long thin features that seems to stream out from the surface. Thermal X-rays emitted by extremely hot plasma trace out the magnetic field lines. Regions of open field lines are called coronal holes and are the source regions of the fast solar wind. Structures with closed field lines known as helmet streamers are source regions of the slow solar wind. These different surface features and solar wind source regions are schematically drawn in Fig. 2.2. At quiet

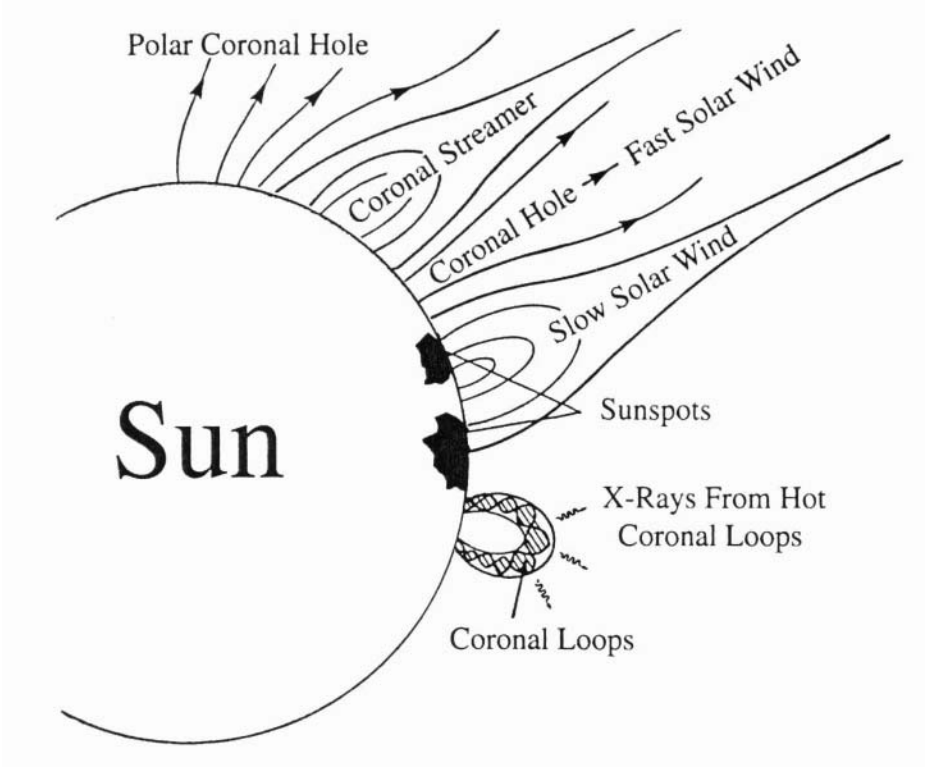

Figure 2.2: **Coronal features.** The magnetic topology of the source regions of fast solar wind, coronal holes, and of slow solar wind, helmet streamers is schematically pictured. Sunspot pairs of opposite polarity are often seen to be connected by loops. (Figure 2.2 of Schunk & Nagy (2000)).

times helmet streamers are mainly found near the equatorial plane and coronal holes cover the polar regions, but during active periods this picture can be greatly disturbed and transient coronal holes can appear at lower latitudes. Imagine a second source region in Fig. 2.1 which is rotationally ahead of the first and for which the radial velocity is greater. At some distance from the Sun the fast solar wind of

the coronal hole will catch up with the slow solar wind creating a shock front.

Cooler and darker than their surroundings sunspots are rather stable regions of increased magnetic field strength. Such a configuration is possible because the high magnetic pressure balance the external thermal pressure. Sunspots almost always come in pairs of opposite polarity which are connected by a flux tube that has risen above the solar surface.

Plasma caught on a magnetic field loop can rise up as the flux tube rises and at the limb of the Sun this is seen as a luminous arc, a prominence. Against the disc of the Sun, however, it will appear as dark a structure, a filament, because the chromospheric material is cooler and denser than the surrounding corona into which is has risen. Filaments are aligned along the neutral line between the two opposite polarity sunspots.

The dynamic nature of the corona can manifest itself in fierce energy eruptions such as solar flares. There are many different theories to explain solar flares, but it seems widely accepted that magnetic field-lines which have risen above the solar surface after convecting up through the outer solar layers are involved and often magnetic reconnection is invoked to explain the violent energy bursts. A likely scenario starts with an active-region prominence: cold dense plasma associated with an arcade of looped magnetic field lines. A prominence can be stable for hours or days but sometimes it takes on a violent evolution: As the magnetic field structure slowly evolves, the loops becomes more and more stretched and the prominence starts rising slowly until the configuration becomes highly unstable and reconnection initiates, causing a large, impulsive energy release which will make the prominence erupt more rapidly. As reconnection continues both the erupting prominence and the plasma on the newly formed loops are heated tremendously causing very bright X-ray emissions. Some flares are accompanied by coronal mass ejections where plasma piled up in the corona above the rising magnetic loops is ejected by the intense energy bursts associated with reconnecting field lines. The lower-lying prominence which consists of chromospheric material might be ejected as well. Coronal mass ejections give rise to large disturbances propagating outward in the solar wind. When emitted in a direction which brings it on a collision course with the Earth, a coronal mass ejection will have a profound impact on the outskirts of the terrestrial atmosphere: the magnetosphere and the ionosphere.

A very important parameter in determining how potently the solar wind can affect the magnetosphere is the angle of the interplanetary magnetic field (IMF) with respect to the Earth's magnetic field. When these are oppositely directed at

the subsolar point, the energy transfer from the solar wind to the magnetosphere proceeds much more efficiently. The varying IMF angle is a consequence of the presence of the heliospheric current sheet which lies between field lines of different polarity and roughly in the equatorial plane. The current flowing around the Sun in the heliospheric current sheet is an effect of the discontinuity which the magnetic field reversal introduces. Figure 2.3 illustrates the shape of the current sheet and shows how the Earth will experience different IMF orientation on its orbital path. The current sheet is highly variable in time and is highly contorted at

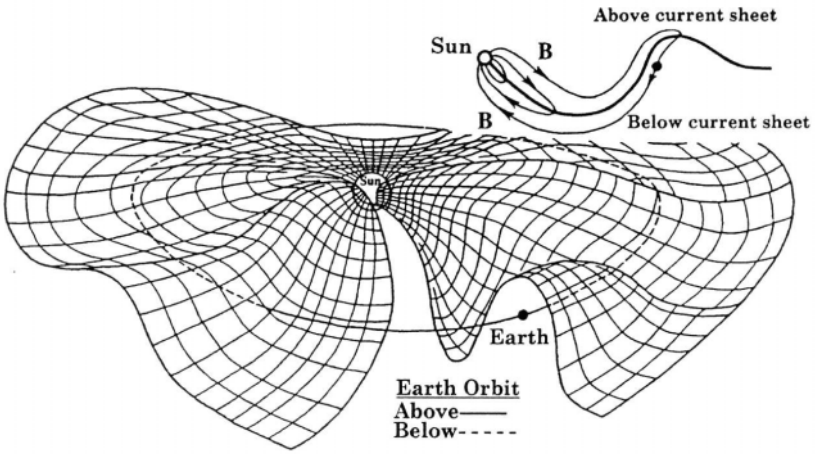

Figure 2.3: **The heliospheric current sheet.** Representation of the three-dimensional structure of the heliospheric current sheet. The IMF has different polarities above and below the current sheet as shown in the inset. The varying IMF orientation along the orbit of the Earth can be seen. (Figure 2.7 of Schunk & Nagy (2000)).

solar maximum.

Solar activity surges and subsides in a cycle that peaks in intensity every 11^{th} year when the solar magnetic field reverses polarity. The traditional indicator for solar activity is the number of sunspots and this has been recorded for 400 years. Solar cycles are not completely regular: some are a bit longer than others, some are more ferocious and some are double-peaked. Periods of high sunspot number are characterized by increased geomagnetic activity.

2.2 The magnetosphere

The Earth's magnetic field acts as an obstacle and causes a standing shock front in the solar wind. When the solar wind encounters this bow shock it is slowed to

subsonic speeds, forming the region known as the magnetosheath where the solar wind is able to flow around the Earth. The bow shock resides a few Earth radii (R_E) in front of the magnetopause which is the boundary separating the geomagnetic field with its plasma populations from the solar-wind plasma. The position of the magnetopause is governed by the balance of the combined pressures of the plasmas and magnetic fields present on each side of the boundary. Looking at the nose of the magnetosphere and reducing this to the dominant terms, roughly speaking the magnetic pressure of the geomagnetic field will balance the solar wind dynamic pressure and determine the magnetopause position in front of the Earth. The variable solar wind can move this boundary further away or considerable closer to Earth than the distance of 12 R_E that is often used as a typical value. In dire cases the magnetosphere can be so compressed that the magnetopause moves within geosynchronous orbit (6.6 R_E), so the geostationary satellites on the dayside for a while find themselves in the magnetosheath.

In a world without the solar wind the Earth's magnetic field would to a very good approximation be a dipole field with a dipole axis tilted 11°with respect to the rotational axis. And close to the Earth it still is. But under the influence of the solar wind it is, as mentioned, compressed on the dayside. On the nightside, however, it is stretched out in a long tail. Often pictures of the magnetotail are not drawn to scale for practical reasons, but in Fig. 2.4 the great extent of the magnetotail can be gauged. The regions of distinctly different magnetic fields are

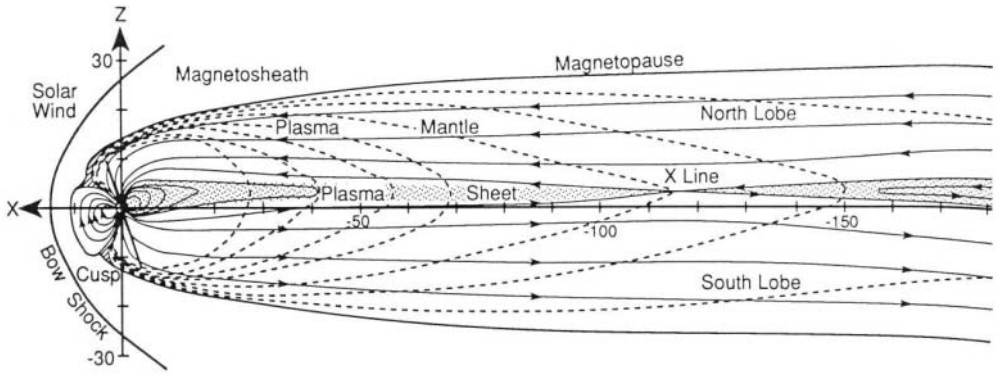

Figure 2.4: **The magnetotail drawn to scale.** Noon-midnight cross section of the magnetosphere. The tilted dipole is shown with a bar. Solid lines are magnetic fi eld lines. Dashed lines indicate the fbw of the mantle plasma. The units on the axes are R_E. The orbit of the Moon is at 60 R_E. The distant X-line is shown at 115 R_E. (Figure 9.3 of Kivelson & Russell (1995)).

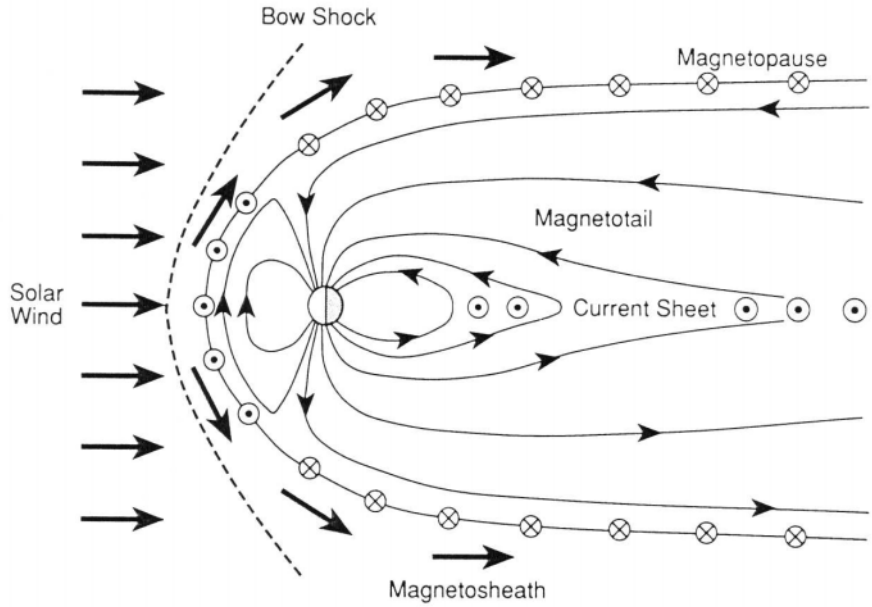

Figure 2.5: **Current sheets of the magnetosphere.** Noon-midnight meridional cross section of a simple Chapman-Ferraro model of the magnetosphere. The geomagnetic field is confined by magnetopause currents. A cross-tail current sheet separates the opposite polarity magnetic flux of the north and south tail lobes. (Figure 9.1 of Kivelson & Russell (1995)).

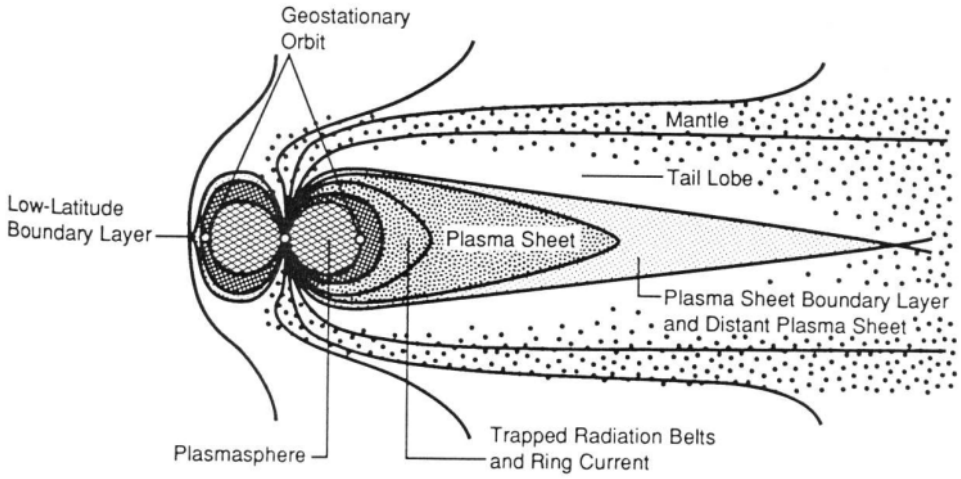

Figure 2.6: **Plasma regions of the magnetosphere.** Schematic drawing of the most important plasma regions of the magnetosphere as seen in the noon-midnight meridian plane. Solid lines are magnetic field lines. (Figure 10.4 of Kivelson & Russell (1995)).

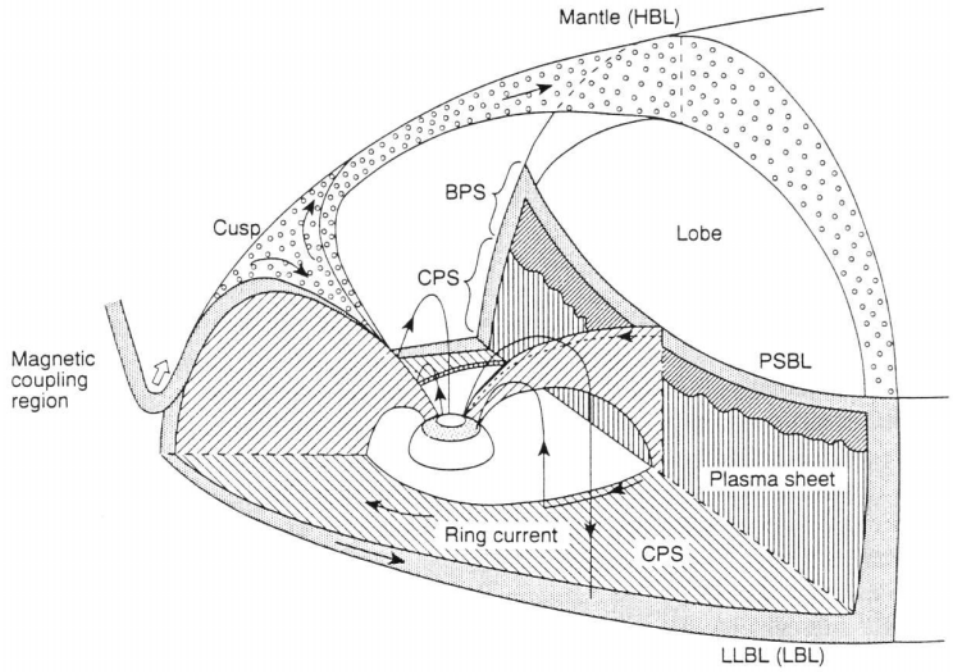

Figure 2.7: **Plasma regions of the magnetosphere.** Schematic drawing of the most important plasma regions including boundary layers. Abbreviations used in the fi gure: BPS: boundary plasma sheet, CPS: central plasma sheet, HBL: high-latitude boundary layer, LLBL,LBL: low-latitude boundary layer, PSBL: plasma sheet boundary layer. Solid lines with arrows depict the region 1 and 2 fi eld-aligned currents. (Figure 5.1 of Potemra (1994) based on work by G. Siscoe).

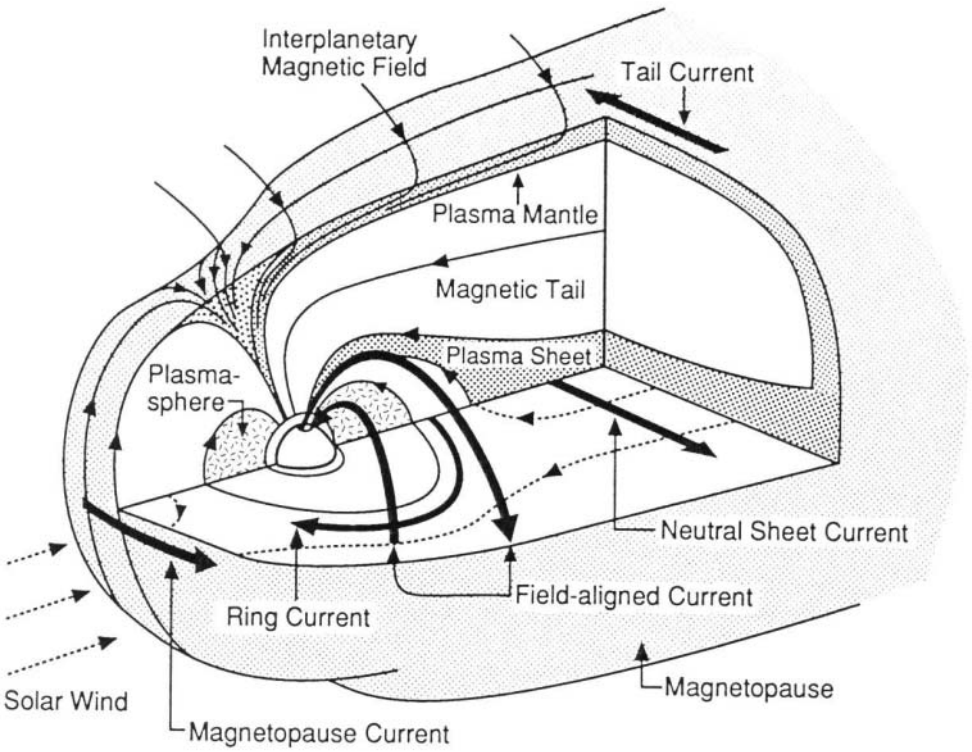

Figure 2.8: **Three-dimensional structure of the magnetosphere.** The noon-midnight and equatorial planes are depicted as well as a dawn-dusk cross section of the tail in this schematic three-dimensional picture of a quadrant of the inner magnetosphere. Shadings indicate different plasma regions as annotated. Solid vector lines are magnetic fi eld lines. Thick solid arrows show currents. Dashed lines in the equatorial plane indicate drift paths of plasma sheet particles entering the inner magnetosphere. (Figure 1.18 of Kivelson & Russell (1995)).

separated by current sheets as depicted in Fig. 2.5. On the magnetopause currents known as the Chapman-Ferraro currents flow. In the mid-plane of the geomagnetic tail a current sheet flows from dawn to dusk, separating the two tail lobes of opposite magnetic polarity. This current sheet connects to the magnetopause currents at the flanks of the geomagnetic tail. The hot plasma that the current sheet is embedded in is called the plasma sheet. Above it is the north tail lobe with its very stretched field lines directed towards and connected to the north polar region of the Earth. Correspondingly the south tail lobe lies below the plasma sheet with the magnetic field lines connecting to and directed out of the south polar region. Between the almost empty tail lobes and the hot ions and electrons of the plasma sheet is a transition region known as the plasma sheet boundary layer whose field lines map to the auroral ovals. The different plasma regions of the magnetosphere are shown in Fig. 2.6, while Fig. 2.7 gives a more detailed picture including boundary layers.

The magnetopause is a more complex transition region than suggested by the thin current sheets of the simple Chapman-Ferraro model. Earthward of the magnetopause current sheet is a boundary layer of several thousand kilometres thickness. Above the north lobe, and correspondingly below the south lobe, is the plasma mantle or high-latitude boundary layer which constitutes a gradual transition to the magnetosheath. Both the lobes and the mantle presumably consist of open field lines. Sunward of the mantle, still on open field lines, is the cusp or entry layer. This region as well as the mantle is populated by magnetosheath plasma, which is able to enter along the open field lines, mixed with an outflow of ionospheric plasma (the polar wind). The magnetosheath is in other regions separated from the magnetosphere by the low-latitude boundary layer: on the dayside and at the flanks of the plasma sheet.

An overview of the structure and most important features of the magnetosphere is shown in Fig. 2.8.

In the inner magnetosphere resides the plasmasphere, the radiation belts and the ring current. The plasmasphere consists of a dense ($\sim 10^3$ cm^{-3}) cold ($\sim$1 eV) plasma, usually with a sharp outer boundary (the plasmapause) at 3-5 R_E. Coexisting with the plasmasphere are the trapped particles of the radiation belts (or Van Allen belts). These particles move along field lines, mirroring at high latitudes with typical bounce periods of about 0.1 s, and at the same time they drift longitudinally, orbiting the Earth in about 10 minutes. Their gyromotion in the non-uniform magnetic field cause curvature and gradient drift of particles around the Earth – positive ions clockwise and electrons counter-clockwise – resulting

in a westward ring current. There is no clear distinction between the trapped and the ring current particles. The latter phrase emphasizes the particles contributing the main part of the current density, whereas the term 'radiation belt particles' is often used to infer penetrating radiation, i.e. radiation that is damaging to spacecraft. Electrons, for instance, contribute relatively little to the ring current and the total energy of trapped particles, but are instrumental in most spacecraft damage.

The trapped particles have orbits around the Earth from about 1000 km altitude to geocentric distances of about 6 R_E. The ring current is located near the inner edge of the plasma sheet and the outer region of the trapping zone, at 4-6 R_E. In

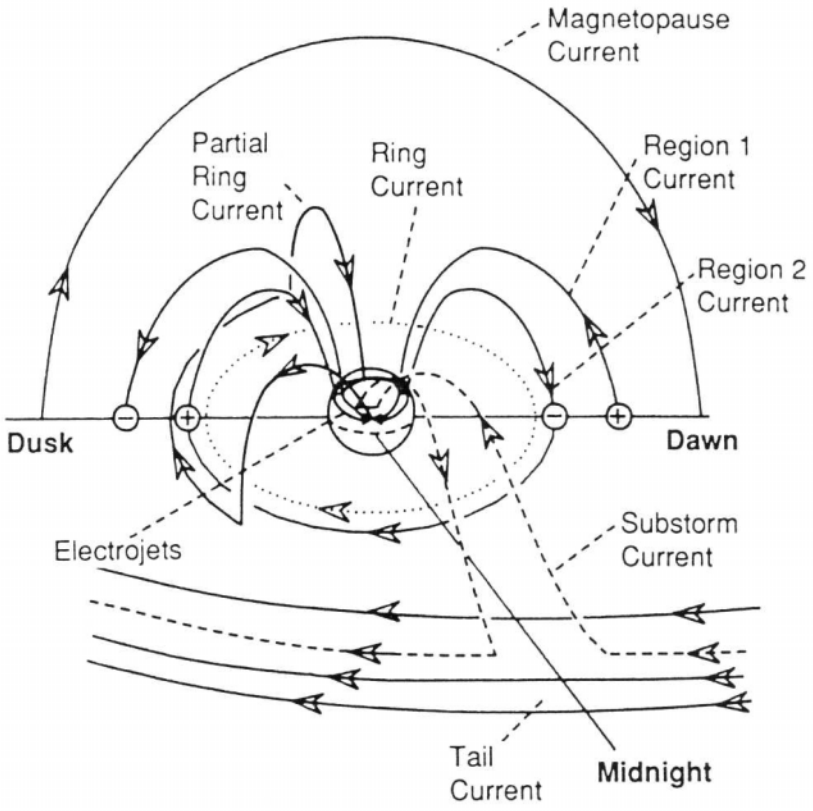

Figure 2.9: **Currents of the magnetosphere.** Schematic three-dimensional representation of the magnetospheric current systems linking to the ionosphere. The view is a dawn-dusk cross section with the Sun in the background and the magnetotail in the foreground. (Figure 13.7 of Kivelson & Russell (1995)).

addition a partial ring current flows mainly on the duskside. It connects at both ends along field lines to the ionosphere, see Fig. 2.9, closing through horizontal

ionospheric currents.

Other field-aligned currents connect the ring current to the ionosphere. These are often called the region 2 currents. They flow into the ionosphere on the dusk-side and out on the dawn-side. At higher latitude are the region 1 field-aligned currents which flow oppositely: into the ionosphere in the dawn sector and out at dusk. The region 1 currents extend far into the magnetotail and close through the magnetosheath boundary layers. At disturbed times additional field-aligned currents flow between the magnetosphere and the ionosphere in the substorm current wedge which is created by diversion of part of the tail current.

2.2.1 Energy transfer from the solar wind

The impact of the solar wind on the dayside magnetosphere is a vast source of energy. The cross section of the magnetosphere is roughly 30 R_E and the kinetic energy flux impinging on the magnetosphere at typical solar wind conditions is about 10 000 GW. Some 5% of this energy finds its way through different interaction processes into the magnetospheric system (Kamide & Baumjohann 1993).

The energy transfer occurs in two distinctly different ways. By now it is widely recognized that the most important process is field-line merging or magnetic reconnection. Other mechanisms are usually called viscous interaction with a general term. They invoke instabilities to explain how momentum can be transferred from the magnetosheath plasma to the magnetosphere. Viscous interaction processes alone are unable to account for the amount of energy seen to enter the magnetosphere. Also it is clear from observations that the rate of energy transfer is strongly dependent on the direction of the interplanetary magnetic field, which is not the case for viscous interactions (Kamide & Baumjohann 1993).

In magnetospheric and ionospheric physics it is customary to use geomagnetic coordinates (see Appendix A). The IMF is usually described by its three components in GSM coordinates: B_x, B_y and B_z. It turns out that when the IMF is directed southwards, i.e. B_z is negative, the energy transfer from the solar wind to the magnetosphere is most efficient. When southward, the IMF is directed oppositely to the Earth's magnetic field, enabling the process of magnetic reconnection to proceed more efficiently at the dayside magnetopause.

The merging and subsequent separation of solar-wind field-lines and geomagnetic field-lines proceed in a cycle suggested by Dungey (1961) and depicted in Fig. 2.10. For simplicity, consider a solar-wind field-line that is oppositely directed to the geomagnetic field at the front of the magnetopause. Extending to

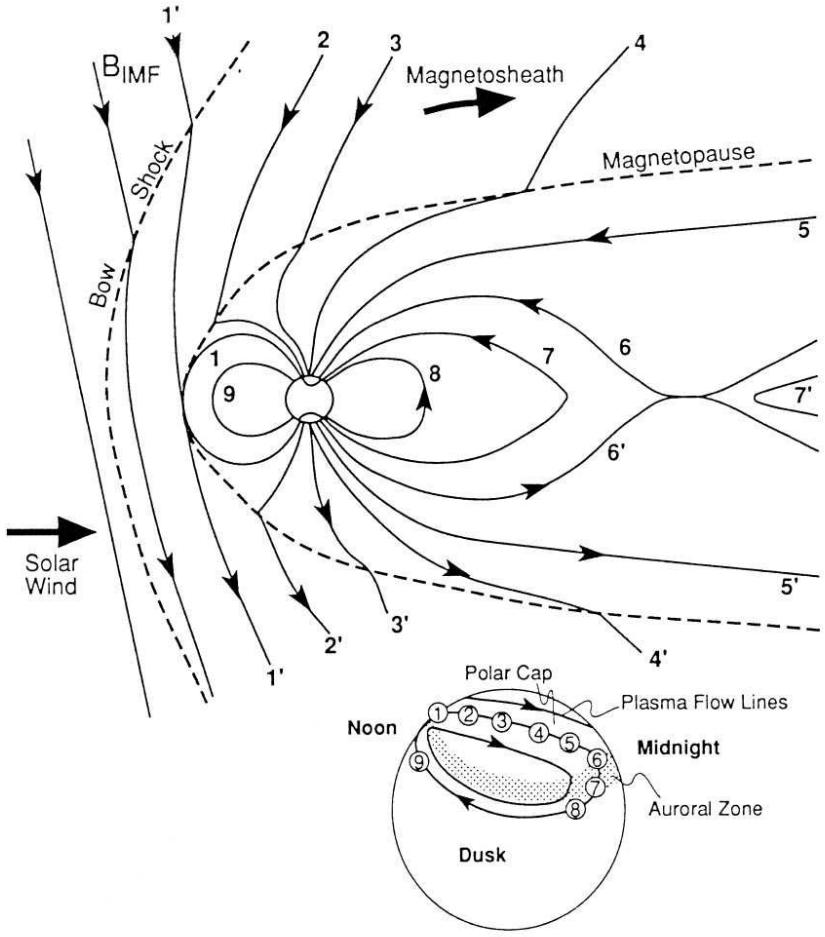

Figure 2.10: **The Dungey cycle.** At the front of the magnetopause the IMF field line marked 1′ merges with the closed geomagnetic field line marked 1. The numbers can be seen as a time sequence. The newly open field lines 2 and 2′ are dragged tailward by the solar wind flow, further and further, until they have obtained a very stretched configuration, 5 and 5′. As magnetic flux builds up in the tail lobes the northern and southern lines will move closer to the neutral sheet and eventually meet and merge, 6 and 6′. The graphic representation is out of scale as the reconnection site is usually located some 100–200 R_E down the tail. The new field line 7′ which is no longer attached to the Earth is free to move further out into interplanetary space. The closed field line 7 will return to the dayside. The projection of foot lines in the inset shows how the newly opened field lines participate in a tailward flow across the polar cap and the closed field lines return to the dayside at lower latitude, thus creating a two-cell circulation pattern. (Figure 9.11 of Kivelson & Russell (1995)).

infinity at both ends it is carried along by the solar-wind plasma approaching the Earth where it will merge with a geomagnetic field line, forming an X-shaped neutral line. The two field lines will reconnect in a new configuration creating two open field-lines, i.e. lines connected to the Earth at only one end, the other end extending to infinity. The solar-wind plasma flow around the Earth will drag the open field lines across the polar regions to the nightside. Here field lines connected to the northern and southern hemisphere, respectively, will again come together and form a second neutral line some 100–200 R_E downtail. The field lines reconnect creating a solar-wind field line with no attachment to the Earth and a closed field line with both feet on the ground. The infinite solar-wind field-line will continue down-stream while the closed field-line will return to the dayside.

Mapping the magnetic foot-lines to the ionosphere gives a double-vortex flow pattern where open field-lines at polar latitudes flow antisunward, while the return flow of closed field lines takes place at lower latitudes. This two-cell pattern resembles thermally driven flow cells and thus got associated with the word convection. The misnomer has stuck, and phrases like ionospheric convection and magnetospheric convection are widely used.

The merging process also proceeds when the IMF is not directly southward, but less efficiently so. When the IMF is northward, reconnection does not happen on the dayside, see Fig. 2.11. Instead the field lines become bend around the magnetosphere, stretched over the polar caps until reconnection becomes possible on the nightside (Biskamp 2000). This will imply an erosion of the field on the nightside, completely opposite to the southward case, but much less effective. For northward IMF the field lines can also be swept around the magnetosphere completely avoiding reconnection.

Reconnection does not proceed as a steady process as could be envisioned from the simple picture described here. Averaging over an appropriately chosen time interval the reconnection rates on the dayside and nightside should of cause be equal, but for short time scales they hardly ever are. During periods of southward IMF magnetic flux is transferred from the dayside to the nightside magnetosphere. In this way substantial amounts of energy can be stored in the magnetotail.

2.3 The ionosphere

The upper layers of the Earth's atmosphere are subject to the most energetic part of the solar radiation: UV and X-ray photons which ionize the constituent atoms

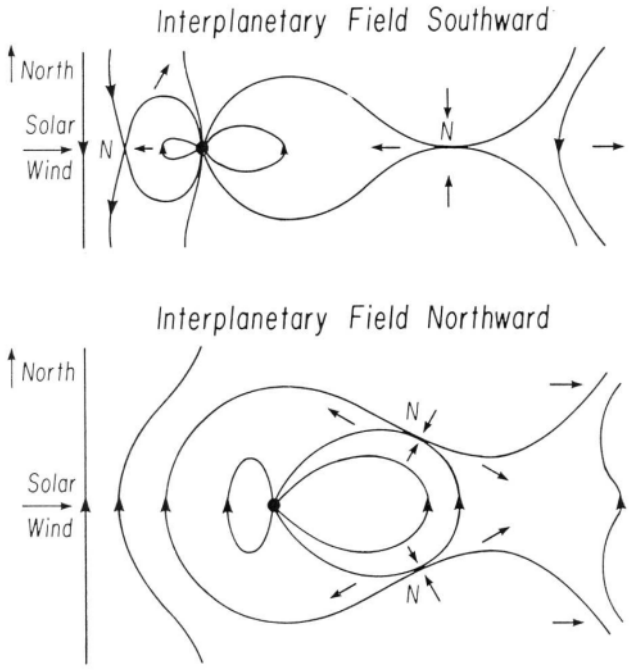

Figure 2.11: **The Dungey cycle for southward and northward IMF. Top:** The classic Dungey cycle for southward IMF. **Bottom:** How reconnection can occur during northward IMF. (Figure 1.16 of Kivelson & Russell (1995), based on work by Dungey).

and molecules. Because the atmospheric density decreases rapidly with altitude, recombination proceeds rather slowly, and above about 80 km there is a permanent population of ionized species. This region is appropriately called the ionosphere, and it reaches up to an altitude of about 1000 km above which the magnetic field begins to dominate and the realm of the magnetosphere exists. The concentration of free electrons only amounts to something like 1% (Hargreaves 1992), but properties profoundly different from those of the underlying neutral atmosphere ensue: Being a plasma, different interactions and waves exist, and the conducting medium allows for strong currents to flow and affects the propagation of radio waves.

The atmospheric layers (Schunk & Nagy 2000) are often defined by their temperature gradient: The troposphere where we live is the layer closest to the ground and the one associated with atmospheric weather. Here the temperature decreases with increasing height until the tropopause at 10-12 km altitude. Above this is the stratosphere where the temperature starts to increase again, reaching a maximum at the stratopause at about 45 km altitude due to absorption of UV radiation by

the ozone layer. The lowest temperature of about 180 K is reached at the top of the mesosphere at some 95 km altitude. We now reach the thermosphere where the highest temperature is found. Heating, mainly via ionization, increases the temperature to something like 1000 K, variable with time, and this temperature remains constant further out.

In the thermosphere diffusion processes become important and the atmosphere is no longer well mixed. This will give rise to a separation where the heavier molecules dominate at lower altitudes and the less heavy atoms become predominant higher up. Atmospheric chemistry is also important in determining the height profiles of the abundances of the different species. Above about 500 km, in the exosphere, collisions become unimportant.

The main ionizing source is solar UV radiation, but ionization by precipitating particles also contribute substantially, especially at high latitudes. The local electron density is a result of the competition between the local ion production and recombination rates. Diffusion and transport processes can also influence the chemical composition and electron density. The density of a species can as a first approximation be described as exponentially decreasing with altitude. The intensity of ionizing radiation will decrease as it penetrates down through the atmosphere subject to absorption. This means that the electron production from solar radiation will maximize at a specific height. This peak altitude will be raised as the solar zenith angle increases because the sunlight is attenuated by the longer travel distance. At night time the electron density falls off as recombination processes dominate. Light emission from the recombination processes, airglow, is unstructured and present at all latitudes, and is thus different from the aurora whose source is precipitating particles.

The ionization by energetic particles is much more variable with time. The particles come in from the magnetotail so they are most abundant around midnight and the flux and energy are very dependent on the geomagnetic activity level. The maximum ionization height in the ionosphere by precipitating particles is determined by the energy of the particles: the more energetic the further down into the atmosphere do they penetrate before depositing their energy.

Geomagnetically disturbed times give rise to an increased heating of the ionosphere via Joule heating and increased ionization. The heating makes the atmosphere expand which affects the local chemical composition. The upwelling will also increase the recombination rate. The atmospheric expansion means that the density at a specific height is increased. This gives rise to an increased atmospheric drag on spacecraft, causing them to lose altitude.

2.3.1 Ionospheric and field-aligned currents

The presence of free electrons means that the ionosphere is a conducting medium. The presence of a magnetic field means that the medium is anisotropic with respect to the currents that flow. Consequently, the conductivity is a tensor, not just a proportionality constant as for a simple conductor.

When the applied electric field is perpendicular to the magnetic field the conductivity is described by two components: the conductivity in the direction of the applied field is known as the Pedersen conductivity, whereas the component perpendicular to the applied electric field is called the Hall conductivity. When the applied electric field is parallel to the magnetic field the situation is simpler and the conductivity is called longitudinal.

The ionospheric Hall and Pedersen conductivities are influenced by the electron density, the collision frequencies (ion-neutral and electron-neutral) and the atmospheric density. Thus the conductivities are altitude dependent. The height-integrated Pedersen conductivity receives its main contribution from altitudes between 125 and 140 km (Kamide 1988), while the Hall conductivity is strongly influenced by energetic particle precipitation and obtains the highest values below 125 km. On geomagnetically quiet days the height-integrated Hall conductivity is about twice the height-integrated Pedersen conductivity, whereas on disturbed days the ratio of height-integrated Hall to Pedersen conductivities is greatly varying and generally exceeds two.

The previously mentioned ionospheric two-cell circulation pattern will drive ionospheric currents since the movement of ions is subject to more collisions than that of electrons and thus the ions lag behind. This will give rise to a sunward current over the polar cap, and in the auroral oval where conductivities are high the currents are concentrated into an eastward electrojet on the duskside and a westward electrojet on the dawnside. The Hall currents of the electrojets give rise to characteristic ground magnetic perturbations. Well-distributed arrays and networks of magnetometer stations is an essential way of monitoring the global ionospheric circulation pattern.

The plasma movement is equivalent to the presence of a dawn-to-dusk electric field with a highly variable potential difference with a typical value of around 60 kV. Instead of the plasma flow pattern it is often equipotentials of the electric field that are shown in plots.

When the IMF has a large B_y component the flow cells are skewed (see Fig. 2.12) and the open-closed field-line boundary is moved dawnward in the

northern hemisphere in the case of positive B_y and duskward for negative B_y (Cowley et al. 1991). In the northern hemisphere for IMF B_y positive the newly opened field lines will preferentially be transported to the dawnside of the tail lobe due to stresses exerted on the field lines by the IMF B_y component. This gives rise to a westward ionospheric flow in the cusp region immediately poleward of the open-closed field-line boundary known as the Svalgaard-Mansurov effect. Further poleward the flow turns and moves across the central polar region. In the southern

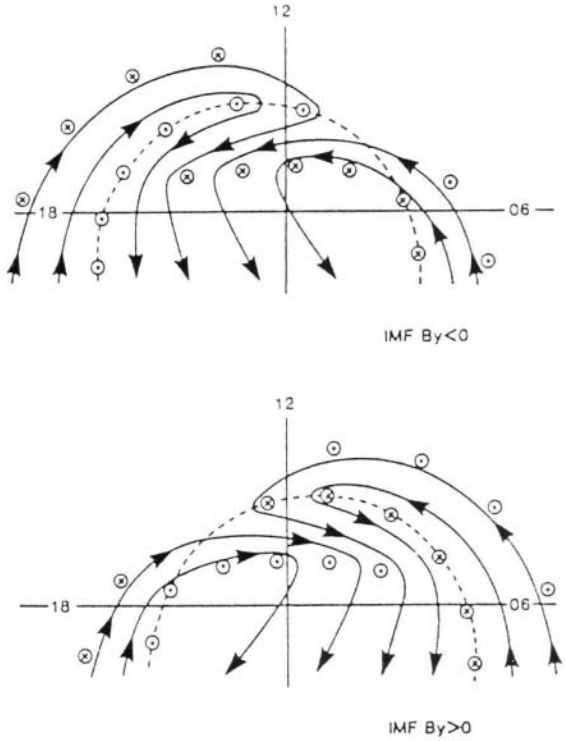

Figure 2.12: **Ionospheric circulation patterns for large IMF B_y.** Solid lines: plasma flow. Dashed line: open-closed field-line boundary. Perpendicular vector symbols: field-aligned currents. (Upside down version of Fig. 3 of Cowley et al. (1991) from Potemra (1994)).

hemisphere the stresses will work oppositely and give a preferential transport of newly opened flux lines to the dusk tail lobe for positive IMF B_y. For negative B_y conditions the flow patterns will be skewed oppositely. Flow changes due to IMF B_y sign reversal occur rapidly.

During periods of strongly northward IMF the circulation can reverse so that the flow over the central polar cap is sunward. The circulation change is initi-

ated quickly near local noon, and the final configuration is obtained after roughly 20 minutes (Clauer 1994). However, Stauning et al. (2002) have observed a case where the change occurred very gradually and the complete reversal took about one hour.

The large-scale ionospheric flow patterns depict the plasma motions of the magnetosphere. Another feature connecting the two regions is field-aligned currents. A statistical pattern of field-aligned currents derived from nigh on 500 satellite passes was presented by Iijima & Potemra (1976), see Fig. 2.13. The poleward

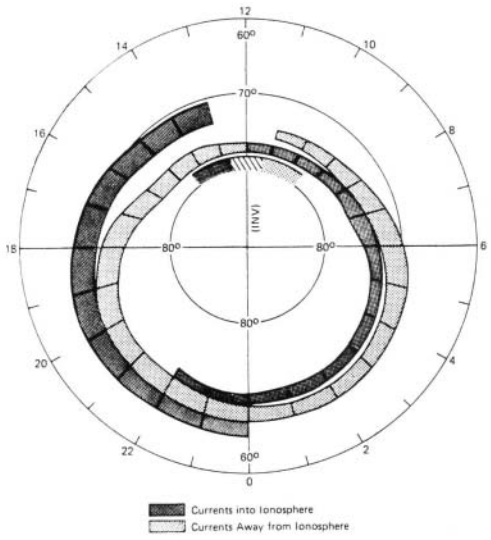

Figure 2.13: **Field-aligned current distribution.** Statistical distribution and fbw direction of large-scale fi eld-aligned currents for weakly disturbed conditions (AL$<$100 nT). Plots are for the northern hemisphere. Noon is upwards. Dark shade: downward currents. Lighter shade: upward currents. The hatched area in the noon sector indicates varying current fbw directions. (Figure 6 of Iijima & Potemra (1976)).

currents which are downward at dawn and upward at dusk are the region 1 currents. The equatorward region 2 currents are oppositely directed, i.e. upwards on the morning side and downward on the afternoon and evening side. The pattern of continuous bands is an average over currents driven by at least half a dozen different ionospheric sources (Potemra 1994). At noon and midnight there are often more than two distinctive current sheets and the region 1-region 2 notation breaks down.

Field-aligned currents are associated with shears in the flow and thus the position of the field-aligned currents shift, especially in the noon sector, with the

orientation of IMF B_y as seen in Fig. 2.12. Near midnight the field-aligned currents are mainly driven by magnetospheric substorm processes which create the substorm current wedge.

During times of strongly northward IMF a current system known as NBZ currents can exist. At very high geomagnetic latitude (85°), two cells of polarity opposite to the region 1 current equatorward of them are seen (Stauning 2002). They are probably driven in a way similar to the dayside region 1 currents whose intensity is strongly dependent on IMF B_z. The dayside region 1 currents are more intense during southward IMF conditions when dayside reconnection is most efficient. In the high-latitude boundary layer there is a southward component of the magnetospheric field so that merging can proceed at northward IMF conditions. Such a mechanism can explain the observed features of the NBZ field-aligned currents.

The first empirical model of field-aligned currents were not followed up by other comprehensive studies based on in situ measurements until recently when Weimer (2001) presented maps based on magnetic measurements from the Dynamics Explorer 2 satellite for different IMF and solar wind conditions and dipole tilt angles.

Papitashvili et al. (2002) have presented a field-aligned current model based on high-precision magnetic field measurements from the Ørsted and Magsat satellites. The extensive statistical material allows for separation not only in bins of IMF conditions but at the same time by seasonal and hemispheric parameters, allowing the seasonal dependence of asymmetries between the hemispheres to be resolved.

2.3.2 The aurora

The aurora is a dynamic display of light emission from atoms, ions and molecules that have been excited or ionized by precipitating particles. The emissions mainly occur at altitudes from 100 to 300 km. Depending on the source of energizing particles the aurora can appear as narrow arcs stretching across the sky with a quite stable appearance, it can be seen as rays, draperies or arcs moving and changing rapidly or it can be an unstructured backdrop of vague emissions.

The visible aurora can be classified in many ways. It is customary to distinguish between diffuse aurora which occurs in ionospheric regions that map along geomagnetic field lines to the central plasma sheet, and discrete aurora which appear poleward of the diffuse aurora and for which the source region is the plasma

sheet boundary layer (Hargreaves 1992).

The auroral oval, which is fixed with respect to the Sun, is broadest in the midnight sector. The auroral zone is a geographic region with a constant width corresponding to the extent of the midnight auroral oval. Within the auroral zone aurora is observable with the naked eye on more than half of all clear nights. The frequency and intensity of aurora increase with solar activity.

The dominant lines of the auroral spectrum are from transitions in atomic oxygen and from neutral and ionized molecular nitrogen. The brightest visible auroral line is the green oxygen line at 557.7 nm. This is a transition from the $^1S_0$ to the $^1D_2$ level[1]. From the $^1D_2$ level there is a doublet at 630.0 and 636.4 nm to the levels $^3P_2$ (ground level) and $^3P_1$ respectively. The 630.0 nm line is the strongest of the two (three times as probable). (Actually it is a triplet not a doublet, as there is of course also a transition to the $^3P_0$ level, but the transition probability is 8000 times lower (Osterbrock 1989), so the line is not seen).

These oxygen lines are all due to quantum-mechanically forbidden transitions[2] that can occur only because the atmospheric density at high altitudes is so low that collisional de-excitation is not important. The $^1S_0$ level has a lifetime of 1 s but that of $^1D_2$ is even longer: 110 s. The oxygen doublet is completely quenched below 200 km altitude. Typically the red colour of the 630.0 nm line dominates at the highest altitudes whereas the yellow-green colour often prevails closer to the ground. Below 100 km the colour magenta is often seen. These reddish-blue emissions are from vibrational bands in N_2^+, N_2 and O_2^+. Hydrogen contributes with two weaker lines: the first lines of the Balmer series, Hα and Hβ.

There is of course a multitude of other lines of varying intensity depending on the precipitating source. Generally soft precipitation gives a predominance of atomic lines, whereas energetic precipitation penetrates deeper and excites more of the molecular bands. This means that simultaneous monitoring of two appropriately chosen emission lines can be used as a diagnostic of the hardness of the energy spectrum of precipitating electrons. The line ratio of the [O I] 630.0 nm line[3] and the N_2^+ 427.7 nm band has been empirically calibrated to the auroral

[1] Here the Russell-Saunders notation (Bransden & Joachain 1983) for the electron configuration of an atomic state is used. It is beyond the scope of this thesis to review the quantum mechanics of the energy levels of atoms and transitions between them.

[2] Forbidden means that they are not allowed in the electric dipole approximation, but the transitions can still occur as magnetic dipole, electric quadrupole and/or higher-order transitions. The transition probabilities are several orders of magnitude lower than for electric dipole transitions.

[3] In this spectroscopic notation the square brackets indicate a forbidden transition, and O I means the neutral (atomic) form of O. O II would denote the singly ionized form, O III the doubly

electron energy (Rees & Luckey 1974).

Space-borne imagers have access to other parts of the auroral spectrum and can monitor larger areas than ground-based instruments. Especially UV imaging is used to obtain valuable information about the global development of auroral activity.

2.4 Energetic electron precipitation

The distinction between soft and energetic electrons is by no means well-defined. For the purpose of ionospheric precipitation studies 1 keV is an appropriate limit.

Statistical studies e.g. by McDiarmid et al. (1975) and Hardy et al. (1985) have charted the distribution in flux and energy of precipitating electrons as a function of geomagnetic activity level from in situ particle measurements on low Earth orbit satellites. The former restricted the data samples to 1100 passes of low geomagnetic activity ($K_p \leq 3_0$)[4] while the latter binned their 1.4 million spectra by different K_p values.

At the equatorward edge of the auroral zone, immediately poleward of the trapping boundary, are the hot electrons of the diffuse aurora. The mirror point for a trapped particle is determined by the equatorial pitch angle, α_0, i.e. the value at the equator of the pitch angle, α, which is the angle between the velocity and the magnetic field direction. As the gyrating particle moves along the field line away from the equator it will experience an increased magnetic field. The magnetic moment can be expressed as $\mu = E \sin^2 \alpha / B$, where E is the kinetic energy of the particle, α is the pitch angle and B is the magnetic field strength. Conservation of the magnetic moment implies that the pitch angle increases as the particle moves poleward and experiences the increased strength of the converging field. Eventually all parallel kinetic energy is converted to transverse energy, $\alpha = 90°$, and the particle will bounce back. The location of the mirror point is determined by $B_0/B_M = \sin^2 \alpha_0$, where B_0 and B_M are the magnetic field strength at the equator and at the mirror point, respectively.

If the particle travels into the atmosphere before encountering the mirror point it will be lost due to interactions. The particles which have pitch angles which make them subject to atmospheric interactions are said to be in the loss cone. The diffuse aurora is caused by hot plasma sheet electrons that are scattered into the

ionized form and so forth.

[4]For a definition of the geomagnetic index K_p see Appendix B.

loss cone.

Further poleward the electrons are of lower energy. When the geomagnetic activity increases, the auroral oval expands greatly equatorward and both fluxes and energies of the electrons increase. The intensity of energetic electrons reaches maxima in the pre-midnight and in the morning sector, the latter being of highest average energy. The pre-midnight maximum is related to substorm break-up events, while the morning maximum is caused by energetic electrons which drift eastward after having been injected near midnight at a substorm onset.

The higher the energy, the faster the electrons drift around the planet, and the further will they drift before precipitating into the atmosphere. In the morning sector there exists a mechanism of wave-particle interaction that effectively scatters the energetic electrons into the loss cone (Østgaard et al. 2000; Matthews et al. 1988).

Besides excitation and ionization of the atmospheric constituents the precipitating electrons have a significant impact on the chemical composition due to dissociation of molecules, whether directly by impact or in recombination processes following ionization.

The content of free electrons affects the refractive index of the medium and makes the ionosphere opaque to radio waves below a certain frequency. Radio waves are reflected at the level where the wave frequency equals the plasma frequency, and this fact is used to probe the ionosphere. Incidentally, radar for air craft detection were developed from the technique of ionospheric sounding.

Radio waves of higher frequency than the maximum plasma frequency of the ionospheric layers will penetrate, but will be subject to absorption. The absorption is proportional to the electron density and the electron-neutral collision frequency. The background of galactic radio noise provides a stable source for measurements of ionospheric radio wave absorption which enables continuous monitoring of increases in the electron density. The method is called riometry, where rio is an acronym for relative ionospheric opacity.

2.4.1 Atmospheric X-rays

Another effect of precipitating energetic electrons is emission of atmospheric X-rays in the bremsstrahlung process where an electron is decelerated in the Coulomb field of an atomic nucleus.

Only a fraction of the electrons will give rise to X-ray emission. E.g. only one in 200 electrons of energy 200 keV will produce a photon of at least 10 keV,

whereas only one in 17500 20 keV electrons will succeed (Berger & Seltzer 1972). X-ray imaging and spectroscopy are none the less very useful remote sensing techniques for obtaining information on the precipitating high-energy electrons. Such measurements capture the high-energy tail of the electron energy distribution which contribute non-negligibly to the global energy deposition (Østgaard et al. 2001) and the Hall conductance (Aksnes et al. 2002), especially in the pre-midnight and morning sectors.

X-rays penetrate deeper into the atmosphere than electrons and can be detected by balloon-borne detectors at heights of 30-40 km. A primary electron of 20 keV will penetrate to a depth of 93 km (mean range) while a photon possessing the same energy on average will reach an altitude of 46 km before absorption (Berger & Seltzer 1972). Atmospheric X-rays are not terribly important for the energy deposition in the ionosphere, except at low altitudes. Below about 80 km they contribute significantly to the ionization (Luhmann 1977).

An advantage of X-ray measurements is that the X-ray aurora can be observed on the dayside as well as on the nightside. Furthermore it is important to note that atmospheric bremsstrahlung X-rays originate exclusively from interaction between energetic electrons and atmospheric constituents. Thus X-ray measurements do not suffer from the inability to distinguish between emissions from precipitating electrons and protons. Determining electron fluxes from auroral emissions can lead to overestimation because significant amounts of auroral emissions are due to proton precipitation and not, as is often assumed, almost exclusively from precipitating electrons (Frey et al. 2001).

2.5 Ion precipitation and outflow

As for electrons, ion precipitation occurs in the auroral zone. The number flux is, however, smaller by 1-2 orders of magnitude (Schunk & Nagy 2000) and the contribution to the downward field-aligned current is negligible. Nevertheless, since the average energy of the precipitating ions is much higher than for the precipitating electrons, the ions contribute significantly to the energy flux.

On the dawn-dusk meridian the highest average ion energies are encountered on the duskside, whereas the electron average energy peaks at dawn. This is due to the different drift paths of negative and positive energetic particles entering the inner magnetosphere from the plasma sheet, see Fig. 2.14. Generally the precipitating electrons carry most of the energy flux, but for all levels of geomagnetic

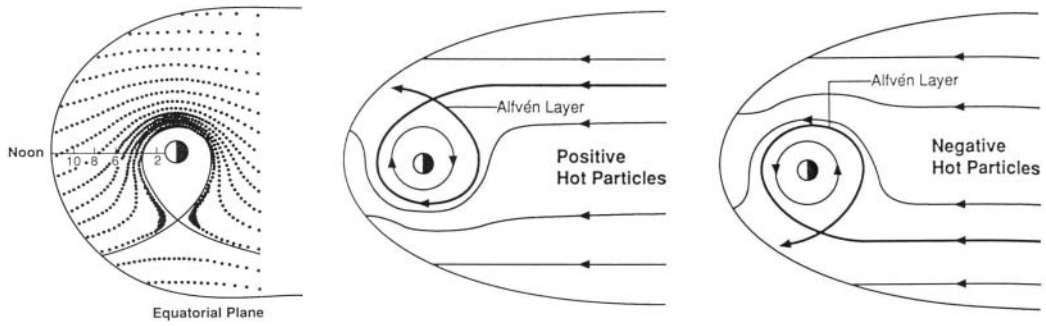

Figure 2.14: **Particle drift paths. Left:** Drift of cold particles. Co-rotation dominates over gradient drift. Spacing of the dots indicates the distance travelled by a particle in 10 minutes. No particles can drift across the loop-shaped separatrix. **Middle and Right:** Drift paths of hot particles. Gradient drift dominates over co-rotation and particles of opposite charge take different directions around the Earth. The separatrix or Alfvén layer cannot be crossed by drifting particles. Note that a particle in the Alfvén layer does not cross its own track as it may seem, but rather follows a path like the one indicated by the innermost path shown in the left panel. Note also that plasma-sheet electrons will come closer to the Earth on the dawnside than ions, and on the duskside ions will penetrate closer than electrons. (Figure 10.25 and 10.26 of Kivelson & Russell (1995)).

activity in the dusk sector near the electron trapping boundary the ion contribution to the energy flux equals or even exceeds that of the electrons (Hardy et al. 1989).

Recently it has become possible to observe the precipitating protons directly, not just the resulting auroral emissions. The precipitating protons are subject to charge-exchange reactions via collisions with the neutral atmospheric constituents. The result is fast neutral hydrogen atoms which will emit Doppler-shifted Lyα radiation via resonant scattering of solar Lyα. On their way down the protons can charge-exchange back and forth many times. With an imager of very high spectral resolution the Doppler-shifted Lyα of the precipitating hydrogen can be discerned against the backdrop of the 100 times more luminous Lyα emissions constituting the geocorona. The geocorona is created by the tenuous neutral hydrogen cloud surrounding the Earth in the exosphere.

The first direct images of the proton aurora were provided by the far-ultraviolet (FUV) imager on the IMAGE satellite (Burch et al. 2001). They show that the protons are not effected to the same extent as the electrons by the poleward expansion of the aurora in substorms. Both the proton and the electron aurora has a diffuse component at lower latitudes, but the structured and discrete emissions at higher

latitudes are mainly caused by electron precipitation. An example of substorm brightening occurring embedded in proton precipitation was reported by Mende et al. (2001), and such observations put a serious constrain on substorm theories.

From the high-latitude ionosphere and the polar cap regions ions flow out into the magnetosphere. Thermal ions escape the gravitational field of the Earth in a supersonic flow, much as the solar wind, which is why the phenomenon is called the polar wind. The nature of the flow changes as it moves along the diverging geomagnetic field lines. It undergoes a transition from dominance of chemical reactions to diffusion, and along the way transitions to collisionless and to subsonic conditions also occur.

In addition to the thermal ion outflow of the polar wind there are many processes that can energize ions and create energetic ion outflows (Schunk & Nagy 2000). From the cusp ions accelerated in wave-particle interactions flow into the mantle, the low-latitude boundary layer and the plasma sheet. Ion outflow from lower latitudes can enter the plasmasphere. The plasma sheet and the tail lobes are populated by ions flowing out from the polar cap, while energetic ions from the nightside auroral oval can feed the plasma sheet and ring current.

2.6 Magnetosphere-ionosphere coupling

The collisionless regime of the magnetosphere and the ionospheric domain where collisions and the presence of neutral particles are important are thoroughly interconnected by the geomagnetic field lines threading both regions. The strong coupling takes many forms, such as field-aligned currents, the circulation of plasma and magnetic flux in the Dungey cycle and in substorm processes, particle acceleration and precipitation and ion outflow.

It is very convenient to be able to map magnetospheric regions down into the ionosphere along magnetic field lines to obtain information e.g. on the source region of energetic particles. This is usually accomplished with geomagnetic field models, such as those of Tsyganenko (1987; 1989; 1995) which are based on actual field measurements. The latter, known as the 1996 Tsyganenko model and referred to simply as T96, included solar wind and geomagnetic activity input parameters to take into account the drastic changes in geomagnetic configuration with different solar wind conditions, whereas the 1989 model, T89, was only parameterized by K_p.

An alternative mapping based on particle precipitation characteristics as ob-

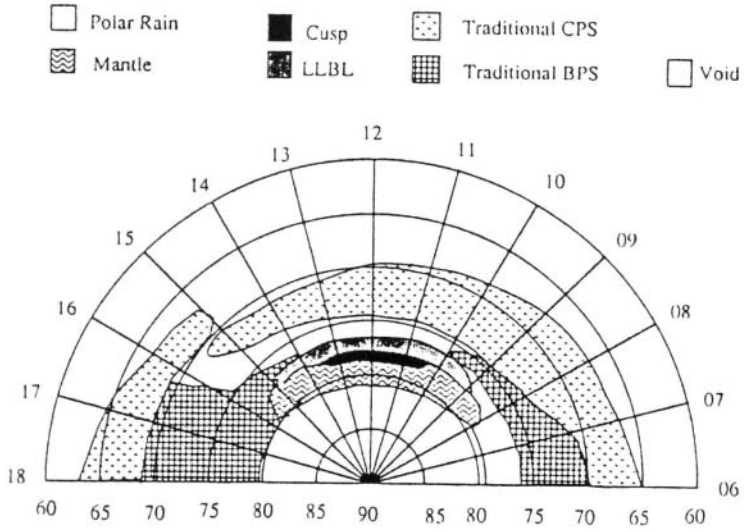

Figure 2.15: **Particle precipitation regions.** Statistical map of plasma characteristics mapping the ionosphere to the magnetosphere. Coordinate grid is magnetic latitude and magnetic local time. (Figure 2 of Newell & Meng (1992)).

served in situ by low-altitude satellites was performed by Newell & Meng (1992). By spectral characteristic the precipitating regions are classified as originating in one of seven categories: Polar rain, mantle, cusp, low-latitude boundary layer, boundary plasma sheet, central plasma sheet or void of significant particle flux.

Polar rain is low-energy electrons from the solar wind able to enter the ionosphere along the open field lines of the polar cap. The mantle source region is characterized by de-energized magnetosheath plasma. In the cusp the magnetosheath plasma can enter directly. The cusp is a latitudinally narrow region, typically extending 1° in magnetic latitude and often $0.^\circ 5$ or less. The ionospheric projection of the low-latitude boundary layer is sometimes called the cleft and the electrons here have lower velocities and higher temperatures than the cusp electrons. The term boundary plasma sheet here covers the source region of discrete aurora and central plasma sheet is used to describe the source region of the diffuse aurora.

In addition to mapping the probability of encountering the seven different types of precipitation, Newell & Meng (1992) produced a compact map of the dayside ionosphere showing the location of the regions of different plasma characteristics. The mapping is consistent with mapping done with different geomagnetic field models (Potemra 1994). The work was followed up by Newell & Meng

(1994) who concluded that the solar wind dynamic pressure is crucial in determining the magnetospheric projections.

2.7 Geomagnetic storms

Shock waves emanating from solar activity and propagating through interplanetary space can give rise to large sudden increases in the dynamic pressure of the solar wind near the Earth. These sudden impulses, usually caused by coronal mass ejections, are able to compress the magnetosphere substantially and often give rise to storm sudden commencements. The severity of a geomagnetic storm is largely controlled by the direction of the IMF. A substantial increase in available energy from increased solar wind velocity and/or density is the other main ingredient. The phases of a geomagnetic storm are characterized by the effect on the ring current as measured by the D_{st} index[5]. The initial phase is when the pressure pulse encounters and envelops the magnetosphere. This pushes the dayside magnetopause inward by as much as several R_E in fierce storms. The compression increases the magnetopause tail currents and will give rise to a positive D_{st} excursion which can last from minutes to hours.

In the main phase of a geomagnetic storm the ring current is built up. Usually the plasma sheet plasma will drift around from the tail on open drift paths and exit at the dayside magnetosphere, see Fig. 2.14. The plasmasphere is a forbidden region of closed drift paths into which no external drift paths can lead. During storms the plasma sheet is pushed in much closer to Earth where the particles suddenly find themselves on closed field paths due to changed topology of the magnetic field. Hence, the particles are trapped in the ring current. The increased ring current will give a substantial deflection in the D_{st} index which in intense storms will get below -100 nT, and in moderate storms will reach below -50 nT. The main phase lasts from half an hour to several hours.

In the recovery phase the ring current particles are lost mainly by ion-neutral charge-exchange collisions on a time scale of days. The resulting escape of energized neutrals makes it possible to image the development of the ring current with neutral atom imagers, such as the ENA (energetic neutral atom) imagers on the IMAGE satellite (Burch et al. 2001).

A geomagnetic storm can give rise to very high levels of particle precipitation in a much expanded auroral oval, and the increased ionization results in el-

[5]The D_{st} index is defined in Appendix B.

evated Pedersen conductivities. In conjunction with the storm-enhanced electric fields this can lead to order-of-magnitude increases in the Joule heating caused by very intense ionospheric currents. Such powerful currents can induce secondary currents at ground-level, which can be hazardous or destructive if they occur in extended high-voltage power lines or pipelines.

Since geomagnetic storms are often caused by coronal mass ejection, forewarnings of the possible impact of a shock wave are sometimes given. Most coronal mass ejections are associated with long-duration X-ray flares which tend to have lower peak temperature than impulsive flares. The arrival of solar X-rays occur within eight minutes of the solar eruption. Based on measurements in two different wavelength bands the X-ray flares peak temperature can be obtained, and the flares are classified according to intensity. From these two parameters the probability of a solar particle event can be evaluated from an empirical calibration: High intensity and low temperature give the highest likelihood of large fluxes of energetic solar particles arriving at Earth (Garcia 1994).

When solar protons arrive, the steepness of the flux increase indicates where on the solar surface the event originated. A very rapid rise suggests that the protons have travelled on a magnetic field line connecting the Earth to an active region on the western solar limb.

From an active region located at western longitudes to which the Earth is well-connected, the solar particles will have easy access, but there is a good chance that the shock front will not impact the Earth. In solar energetic proton events originating at meridional or eastern heliographic longitudes the solar particle flux rises more gradually and the energized particles are associated with shock acceleration rather than direct emergence from a flare region. These events are very often associated with interplanetary shocks impacting the magnetosphere (Garcia 1994).

The position of the active region can also be identified from imaging of the solar disc. Sunspots can be seen in Hα images which are readily available from ground-based solar telescopes. To identify the flare region with greater certainty if many possible source regions are present, space-based X-ray imagers are very helpful.

The shock strength and time of arrival can be estimated from the initial shock speed at the Sun from bursts of radio waves (type II radio bursts) when combined with X-ray and optical data, and the background solar wind speed from monitors at the Earth's orbit (Smith et al. 2000). The transit time is from one to four days.

2.8 Substorms

Reconnection and plasma circulation in the tail appear inherently unsteady. Magnetic flux built up in the tail lobes is aperiodically released in explosive events known as substorms, since originally they were thought to be subdivisions of geomagnetic storms, i.e. that storms consisted of a collection of substorms. Gonzalez et al. (1994) lists three points to note in formulating the relationship between storms and substorms: Firstly, there is no apparent difference between stormtime substorms and substorms at times of quiet D_{st}. The most intense substorms, however, occur during the main phase of a storm. Secondly, no magnetic storms have been observed in the absence of substorms. Thirdly, very high geomagnetic activity ($K_p = 9$) is only recorded during magnetic storms.

In his classic 1964 paper Syun-Ichi Akasofu proposed a model which combined the sequence of auroral events over the entire polar region into a consistent large-scale picture of the auroral substorm, a term which was coined by Sydney Chapman (Akasofu 1964). The development of the auroral substorm was described by two phases: the expansive phase and the recovery phase.

The expansive phase initiates with a sudden brightening of a new or existing arc on the equatorward edge of the quiet arcs in the midnight region. This brightening is followed by rapid poleward motion, resulting in a bulge which expands poleward, westward and eastward. The continued expansion of the bulge creates a westward travelling surge characterized by folded arcs and rapid westward speed. Preexisting bands are displaced poleward by the passage of the surge. In the morning sector auroral patches and omega-shaped bands drift eastward.

Eventually the poleward and westward expansion reaches a maximum, indicating the start of the recovery phase. The aurora starts to withdraw equatorward and abate. Especially in the midnight and evening sector the intensity of the aurora diminishes. In the morning sector continued eastward drift is seen for a while. The duration of the expansion phase is about 30 minutes whereas the recovery phase lasts about an hour or two.

The concept of the auroral substorm was soon extended as it became clear that it was the polar ionospheric manifestation of a magnetospheric phenomenon, the magnetospheric substorm (Coroniti et al. 1968). According to Akasofu (1968) this term was introduced by Neil M. Brice and Kinsey A. Anderson.

McPherron (1970) realized that magnetic signatures detected on the ground and processes that take place in the magnetosphere prior to the substorm expansion phase should be interpreted as part of the magnetospheric substorm model.

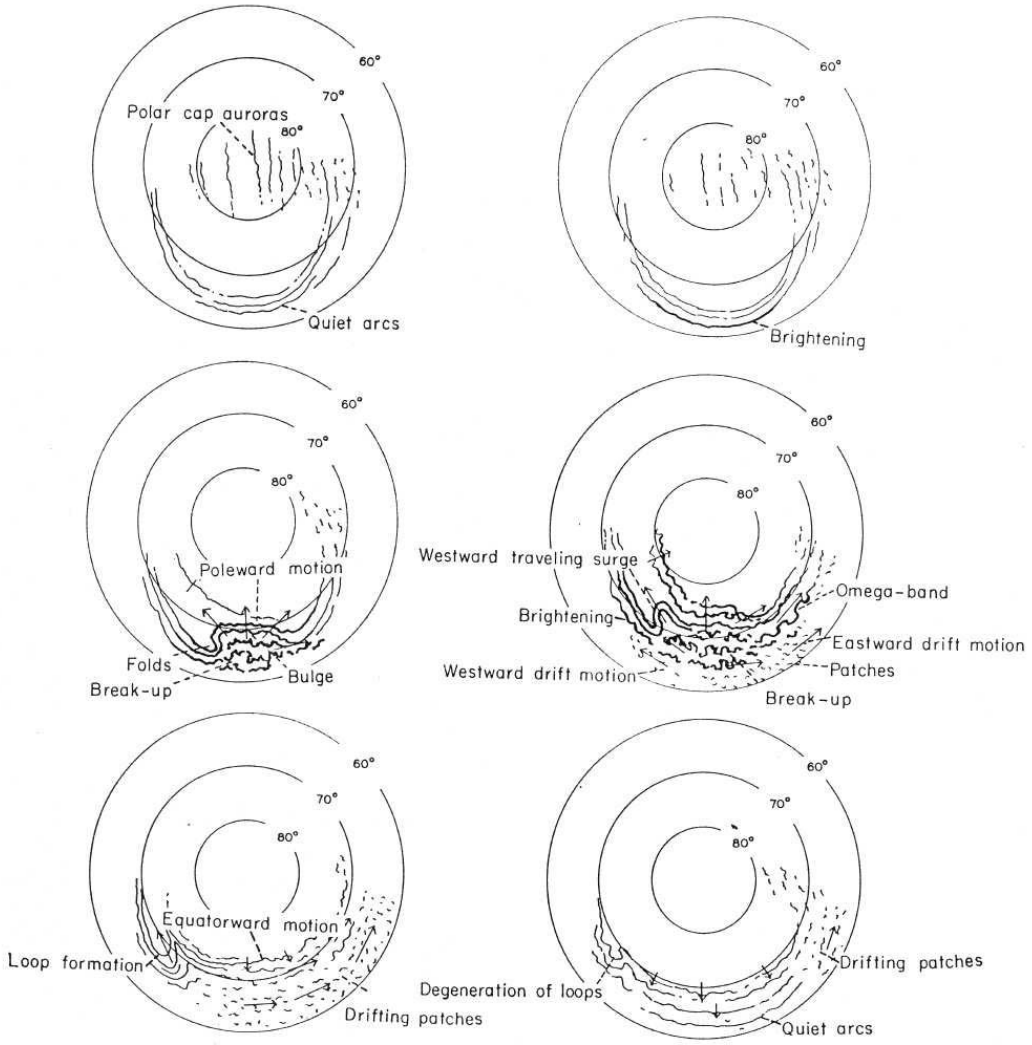

Figure 2.16: **Development of the auroral substorm. Top left:** Quiet phase, before onset. **Top right:** Substorm expansion phase onset, brightening of one of the quiet arcs. **Centre left:** Rapid poleward motion creates the bulge. **Centre right:** As the bulge expand, folds in the evening sky move rapidly westward forming the westward travelling surge. **Bottom left:** When the maximum poleward expansion has been reached, the recovery phase starts. The bulge is reduced and the aurora retreat equatorward. **Bottom right:** Equatorward motion and decrease in luminosity continues. The situation approaches the one before expansion onset. (Figures 2-7 of Akasofu (1964)).

This initial phase he called the growth phase, and it has become part of the standard substorm description.

Sometimes a growth phase does not result in a proper expansion phase onset, but rather in a weaker brightening. This is called pseudo-breakup in contrast to the auroral breakup that initiates the expansion phase. It seems that the same physical process is responsible for the two kinds of auroral activation which differ in spatial size and intensity (Nakamura et al. 1994; Rostoker 1998). Several pseudo-breakups can occur in the growth phase. The reasons why they do not evolve to proper expansion onsets are probably that the available energy loaded into the magnetotail is not yet sufficient and the ionospheric conductivities are too low to allow global-scale expansion.

At a conference in 1978 in Victoria, British Columbia, Canada, nine magnetospheric physicists involved in substorm research took it upon themselves to provide a definition of the magnetospheric substorm in order to achieve a consensus as to what the term covered, since the magnetospheric substorm had turned out to be more complex than first imagined. The ensuing definition (Rostoker et al. 1980) adjusted the original picture of the auroral substorm (Akasofu 1964) by removing the time scales assigned to the different phases and stages. Also the revised picture comprised multiple intensifications (onsets and surges) within a single magnetospheric substorm. Since the phenomenon is global, care needed to be taken in defining the regions of onset and maximum poleward expansion. The necessity of global observations to distinguish these from local intensifications was stressed.

Other modifications to the classic picture occurred over the years (McPherron 1995). It has been realized from space-borne imagers that the expansion phase does not proceed as one continuous motion, but occurs in steps and comprise multiple auroral intensifications caused by successive surges forming increasingly farther westward and poleward. Also, intensifications of the poleward edge of the auroral bulge can occur even after recovery has been initiated at lower latitudes.

Many phenomenological substorms models have been put forward (e.g. McPherron 1995). Some have not achieved wide recognition, some have useful elements, but need to be seen as part as a more complex picture. Most successful in incorporating new observations into the model via continued refinements have been the near-Earth neutral line (NENL) model, a nice review of which is given by Baker et al. (1996).

The early phenomenological model sought to reconcile different observations and previous theoretical work into a sequence of events which consisted of a

growth phase, an expansion phase and a recovery phase (McPherron et al. 1973).

The growth phase initiates when the IMF becomes southward and the merging process starts eroding the dayside magnetopause. The eroded flux is transported to the tail where the increased lobe fields will give rise to an increase in the cross-tail current and an inward extension of the current system while the current sheet grows thinner.

In the expansion phase an intense localized westward electrojet appears and a simultaneous dipolarization of the tail-field. Energization and injection of particles occurs close to the Earth and the plasma sheet expands rapidly.

In the recovery phase the auroral manifestations of the substorm decay and the previous quiet time aurora is reestablished.

Two important features of the expansion phase emerge. One is the substorm

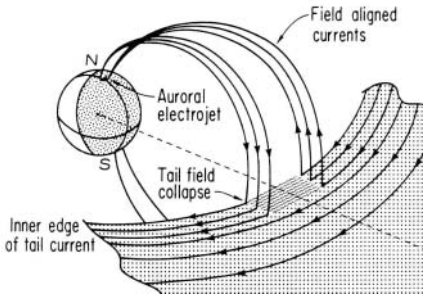

Figure 2.17: **The substorm current wedge.** Part of the cross-tail current is diverted into the ionosphere through field-aligned currents, thus driving the auroral electrojet. (Figure 8 of McPherron et al. (1973)).

current wedge: the diversion of the cross-tail current, see Fig. 2.17, to drive the localized substorm electrojet via field-aligned currents into the ionosphere. The other is the demonstration that the formation of a neutral point in the near tail and its subsequent tailward movement can explain the plasma sheet expansion and the injection of energized particles.

Russell & McPherron (1973) give an in depth description of the model with numerous observational examples of the role of the magnetotail in substorms, and the idea of the near-Earth neutral line is elaborated. It is argued from observations that the reconnection site can be as close as 10 R_E to the Earth at its formation at expansion onset, whereas it must be beyond the Moon's orbit (60 R_E) at quiet times.

Observations by the Imp 8 satellite probing the magnetotail led Hones, Jr. (1977; 1979) to suggest that reconnection starts on closed field lines, resulting in

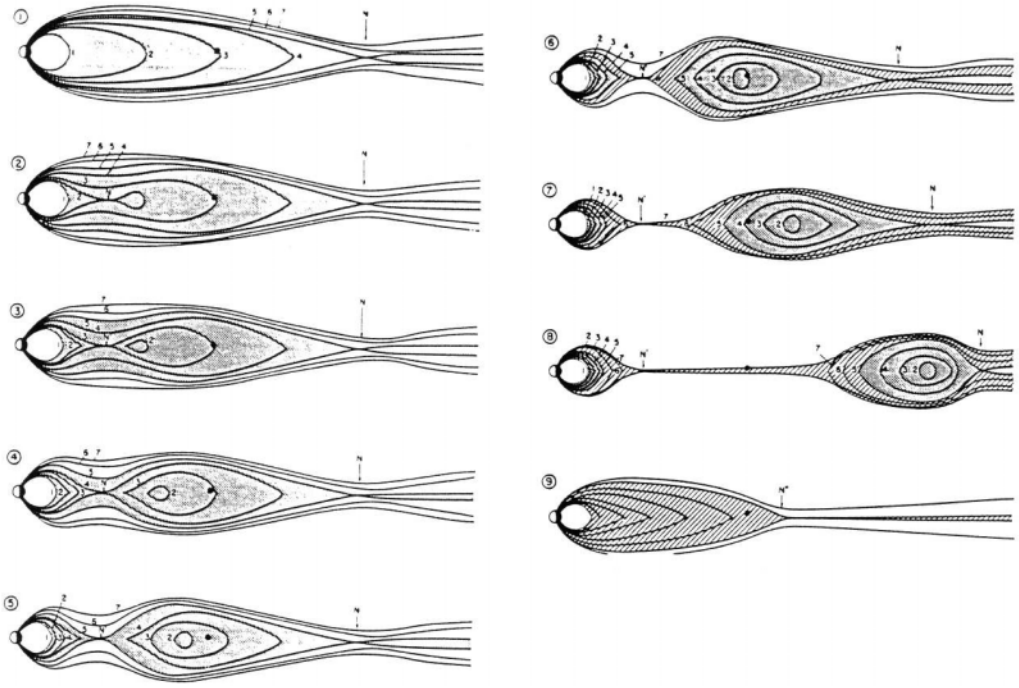

Figure 2.18: **Development of the magnetospheric substorm.** Seven field lines are numbered so their development can be followed. N marks the distant neutral line. N′ marks the near-Earth neutral line which forms on closed field lines at expansion onset, panel 2. The solid circle indicates a spacecraft. Fine hatching delineates plasma of the pre-substorm plasma sheet. Coarse hatching delineates plasma on newly merged lobe field lines that were previously open. Panels 3 and 4: reconnection on closed field lines results in plasmoid formation. Panel 5: reconnection of the last closed field line: the plasmoid is no longer tied to the Earth. Panels 6-8: The severed plasmoid retreats down the tail and is eventually ejected. Panel 9: the near-Earth neutral line rapidly retreats tailward and the plasma sheet starts recovering. (Fig. 3 of Hones, Jr. (1977)).

a dipolarization of the Earthward field while pinching off of a section of tailward material thus forming the substorm plasmoid. Reconnection continues, and when open field lines after a while starts reconnecting, the newly created tailward lines, which are unrooted at both ends, will start dragging the plasmoid tailward as the field line drifts with the solar wind plasma through which it threads. The sequence of events is depicted in Fig. 2.18. Plasmoid formation and ejection is a core feature of the NENL model, and the subsequent observations with ISEE 3 (Hones, Jr. et al. 1984; Baker et al. 1987) of the predicted plasmoid structure was a great success for the model.

Difficulties of the NENL model lies in the mapping of events to the ionospheric phenomena, e.g. the break-up arc seems to lie on closed field lines. The presence of multiple arcs during the growth phase and multiple discrete intensifications after expansion onset are also hard to explain.

One of the disputed features in the model is the sequence of events around expansion onset.

It is not generally agreed whether reconnection is cause or effect in the substorm sequence of events. Lui (1996) argues that a cross-field current instability causes the current disruption in the near-Earth tail and that two possible scenarios follow: It can provide the resistivity for magnetic reconnection, or it can lead to a conversion of magnetic energy to particle energy without the presence of a singularity such as the X-line of the NENL model.

Baker et al. (1999) view the whole magnetosphere as a global system that through the growth phase loading reaches a critical state where catastrophic collapse of the magnetotail occurs in analogy with critical systems such as sandpiles or avalanches. The energy dissipation and plasma flow associated with magnetic reconnection drive all the other features of the expansion phase.

Lui (2001) argues that many satellite studies of the magnetotail, which have been interpreted as evidence of the NENL model, actually fit better in the paradigm of the current disruption model. In this model the substorm is not seen as one global instability, but rather as localized activities which can be caused by a number of different physical processes. External forcing of the magnetosphere causes a critical or metastable state with near-continuous energy dissipation in localized regions. The accumulated effect of these individual transient and localized events constitute a global disturbance, the substorm, which is again seen in analogy with critical systems such as sandpiles or avalanches.

Substorm expansion onset is invariably connected with brightening of an existing auroral arc, and must originate in a region so close to the Earth that X-line

formation is unlikely. In the current disruption model the substorm sequence is initiated with onset of an instability that leads to current disruption close to the Earth. In the turbulent region of current disruption the most equatorward arc associated with the largest cross-tail current is the most likely to initiate auroral breakup. The current disruption leads to injection of energetic particles and causes further thinning of the plasma sheet which will make the current disruption spread tailward. Several current disruption sites are formed further down the tail, and one of these will evolve into an X-line which causes plasma sheet recovery.

Shiokawa et al. (1998) suggests a model in which dipolarization and substorm current wedge formation are initiated by a pile-up of magnetic flux from the braking of a fast flow ejected in a NENL formed previously in the mid-tail. Earthward

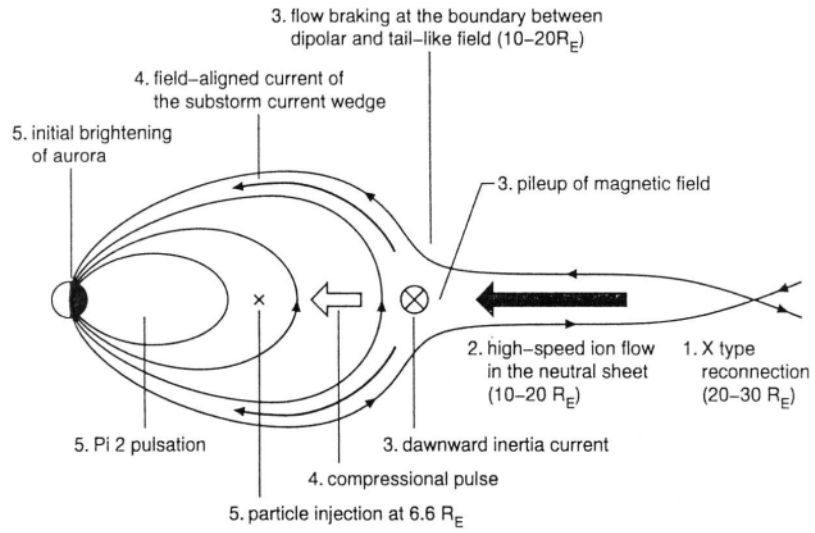

Figure 2.19: **Pile-up model.** Noon-midnight cross section showing how a pile-up of magnetic flux due to braking of the high-speed earthward ion flow from the near-Earth reconnection site causes the substorm current wedge formation. The sequence of events at expansion onset is indicated. (Figure 15 of Shiokawa et al. (1998)).

fast flows in the magnetotail are often interpreted as supporting the pile-up model.

Ohtani (2001) argues that caution is needed and lists a number of problems for this model. He advocates a view where tail-current disruption is an independent process which is triggered by an instability in the near tail, a process that may become more favourable after NENL formation in the mid-tail. This view of the relation between the two distinctive processes of current disruption and NENL formation may resolve some of the difficulties of the pile-up model.

The energy dissipated in the substorm process have in most cases been previously loaded into the magnetotail in the growth phase. Often expansion onset coincides with some discontinuity in the interplanetary medium which triggers an explosive energy release of the magnetospheric system that has become unstable after a period with southward IMF and energy storage.

At other times, however, the energy deposition is directly driven by the solar wind. Probably a compromise between the two processes is closer to the truth. Baker et al. (1997) examined the relative roles of the directly driven and storage-release aspects of substorms and concluded that both play essential roles in the solar wind-magnetosphere interaction.

2.9 Conclusion

This chapter has introduced the important concepts of the solar wind, the magnetosphere and the ionosphere, and the energy transfer between these regions which occurs in the interaction between the solar wind and the magnetosphere and in geomagnetic storm and substorm processes. These are crucial in the generation of precipitating electrons which cause the aurora and are able to produce the atmospheric X-rays which are studied further in Chapters 4 and 5.

Chapter 3

Instrumentation

To gain knowledge of the vast and complex regions of the magnetosphere and ionosphere it is useful to exploit as many data sources as possible. Some instruments provide high spatial resolution, but only limited spatial coverage. Others provide global images showing large-scale structures, but not the details. In situ measurements are often very accurate, but suffer from very limited spatial coverage. Remote sensing techniques can often probe larger regions, but sometimes invoke certain assumptions to derive the desired quantities. Much can be learned from combining simultaneous observations from different types of instruments positioned at several locations. A multitude of data from current and past missions and installations are available to the scientific community, but it is important to be familiarized with the instruments, their capabilities and limitations.

This chapter provides a short description of the most important data sources and observational techniques available to the scientific community. Many of these (notably imaging riometers and the global imagers PIXIE and UVI) have contributed data to the work presented in Chapters 4 and 5.

3.1 Ground-based magnetometers

Magnetometers measuring both strength and direction of the local magnetic field are spread all over the world giving good global coverage, even if the African, Asian, Australian and South American continents and especially the oceans are thinly covered. The data is made available to the scientific community through international database collaborations. Magnetometer data are usually represented as disturbances (measured relative to a quiet day level) in three components which

can be in local geographic or local geomagnetic coordinates[1]. Typical time resolutions are 5 s or 1 minute. Specific stations deliver data for calculation of geomagnetic indices[2] which are used as diagnostics e.g. of the global disturbance level and storm and substorm intensity. Meridional chains, i.e. a number of stations spread in latitude, but lying almost along the same magnetic longitude, such as the Greenland west-coast magnetometer chain, are very useful for comparing temporal and spatial variations in activity. The latitudinal position of electrojets can be followed, and poleward and equatorward movement of activity can be tracked. Even better of course is a grid of stations covering the auroral zone over an entire hemisphere. In the Russian sector stations are sparse, but apart from that it is possible to get a relatively good coverage of the northern auroral zone. A picture of the instantaneous ionospheric circulation pattern can be achieved by plotting the horizontal perturbation vectors rotated 90° counter-clockwise, since the ground magnetic disturbances to a good approximation arise solely from the Hall currents of the ionospheric plasma drift.

3.2 Riometers

The riometer is a radio antenna that measures the absorption of radio waves of a specific wavelength through the ionosphere, or in other words it measures the relative ionospheric opacity at radio wavelengths. To that end a radio source situated above the ionosphere is required. Nature provides one in the form of the galactic radio wave background which is close to uniform except for a few bright radio sources whose positions are known, so that they can be taken into account when analyzing the ground signal. Riometry is sometimes referred to as measurements of cosmic noise absorption.

The absorption is proportional to the electron-neutral collision frequency and the electron density integrated along the line-of-sight. The electron-ion collision frequency gives a smaller contribution due to the low ion density compared to the neutral density. The collision frequency, being proportional to the density, drops off rapidly at increasing altitude, making the riometer most sensitive to increased electron densities at low ionospheric altitudes. Hence the riometer is sensitive to electrons penetrating deep into the ionosphere, i.e. to energetic electron precipitation which in this case means electrons of energies above about 10 keV. Also,

[1] See Appendix A.
[2] See Appendix B.

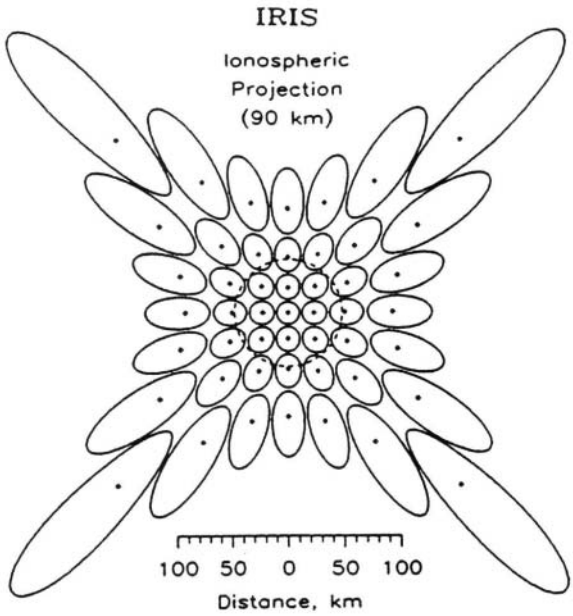

Figure 3.1: **Imaging riometer field-of-view.** Projection of the 49 beams onto the ionosphere at 90 km altitude. The maximum sensitivity of each beam is marked by a dot. The contours indicate where the sensitivity has dropped by 3 dB. The substantial zenith angles of the outer beams gives larger ionospheric cross sections, i.e. larger beam widths. The field-of-view is about 250 by 250 km, and the spatial resolution in the central part is about 20 km. The dashed circle represents the field-of-view of a traditional broad-beam riometer for comparison. (Figure 6 of Detrick & Rosenberg (1990)).

significant absorption levels are observed during solar proton events.

Usually 90 km is used as reference altitude for riometers, but caution must be imposed depending on the type of event studied. The absorption is inversely proportional to the square of the radio frequency, so too high a frequency means the absorption will be hard to detect. The frequency needs to be above the maximum plasma frequency of the ionosphere (about 10 MHz) to avoid reflection. Below 30 MHz man made radio noise becomes problematic, and riometers are usually operated at 30-50 MHz.

The traditional broad-beam antenna underestimates the absorption if the spatial extent of the absorbing region is less than the instrumental field-of-view. Simultaneous operation of antennae of different frequencies and beam-widths can give information on spatial extent of absorption regions (Hargreaves et al. 1979; Rosenberg et al. 1991).

Since the late 1980s a new riometer set-up under the name IRIS (imaging riometer for ionospheric studies) has been installed at several sites, e.g. South Pole, Iqaluit and Kangerlussuaq[3]. Consisting of an array of several narrow-beam antennae, an imaging riometer has a much better capacity for determining the morphology and spatial extent of absorbing regions. In addition it has the ability to resolve the question of whether intensity variations are temporal or spatial in nature. The time resolution is 1 s. The imaging riometers at the three above-mentioned sites all consist of an array of 8 by 8 antennae. The signals from the 64 antennae are input to a phasing matrix (Detrick & Rosenberg 1990) which provides the resulting 49 beams. The field-of-view of the instrument at 90 km altitude is depicted in Fig. 3.1. To be able to determine the amount of absorption of the galactic radio signal, the quiet day level for each beam must be carefully established.

A great advantage of riometers, which is also true for magnetometers, is their capability to operate automatically 24 hours a day, their data quality being unaffected by daylight or overcast conditions.

3.3 Digisondes and ionosondes

The digisonde emits a vertical pulsed radio signal and studies the return signal with an antenna system which can determine the arrival angle, polarization, amplitude, phase and Doppler shift of the received signal. The time delay of the signal is also an important parameter. From such observations the electron density profile, the echo location and the horizontal velocity of ionospheric irregularities can be derived, in addition to the parameters derivable from ionosondes.

Ionosondes are the previous generation of ionospheric sounders, but still widely in use. These measure only delay and amplitude of the return signal which yields information about maximum usable frequencies for radio communication, the virtual height of ionospheric irregularities, structures and layers and estimates of horizontal velocities of such structures. The concept of virtual height refers to the fact that the time-of-flight of the wave is increased by refraction when increased ionization is encountered, and thus only with the data from a digisonde can the true height be calculated.

A serious limitation of digisonde and ionosondes is the fact that information can only be gained about ionospheric layers below the height of maximum ionization. During events of high-energy precipitation this means most of the high-

[3]Previously known as Søndre Strømfjord.

latitude ionosphere is precluded from this type of ionospheric sounding.

3.4 Coherent scatter radars

A radar designed to detect signals reflected from slowly varying turbulent ionospheric structures and irregularities (as opposed to fast thermal fluctuations) is called a coherent scatter radar. The signals are emitted at oblique angles into the ionosphere. Coherent scatter radars using UHF and VHF signals are often called auroral radars and they are used to probe ionization associated with auroral activity, notably plasma instabilities related to the flow of electrojets. The coherent scatter technique is most powerful in a configuration where two geographically separated radars are configured to simultaneously view the same area. The radars independently measure line-of-sight Doppler shifts, and when the data are combined the distribution of echo strength and two-dimensional velocities in the common viewing area can be obtained.

Radars operating in the HF range probe a higher ionospheric region, and are very useful for studying the ionospheric circulation. There exists a network of such radars, SuperDARN (super dual auroral radar network), configured so that at least two radars cover the same area (3–4 million km^2) from different directions. The newest radar, King Salmon, is not yet part of such a pair, however. Currently SuperDARN encompasses nine radars in the northern hemisphere (see Fig. 3.2) and six in the southern.

Combining the line-of-sight Doppler shift obtained with each radar allows derivation of regional or even hemispherical maps of two-dimensional ionospheric plasma drift, electric fields and field-aligned currents. The drawback of the coherent scatter technique is that it requires the presence of physical irregularities or spatial variations able to create radar echoes. Consequently, obtaining a return signal is not always possible. In addition the data interpretation is not straightforward.

3.5 Incoherent scatter radars

A radar probing fluctuations that are faster than successive echoes can resolve, as is the case for thermal fluctuations, is called an incoherent scatter radar. This is the most accurate ground-based radio technique and provides a lot of detailed information about the ionosphere. Different operational modes are designed and

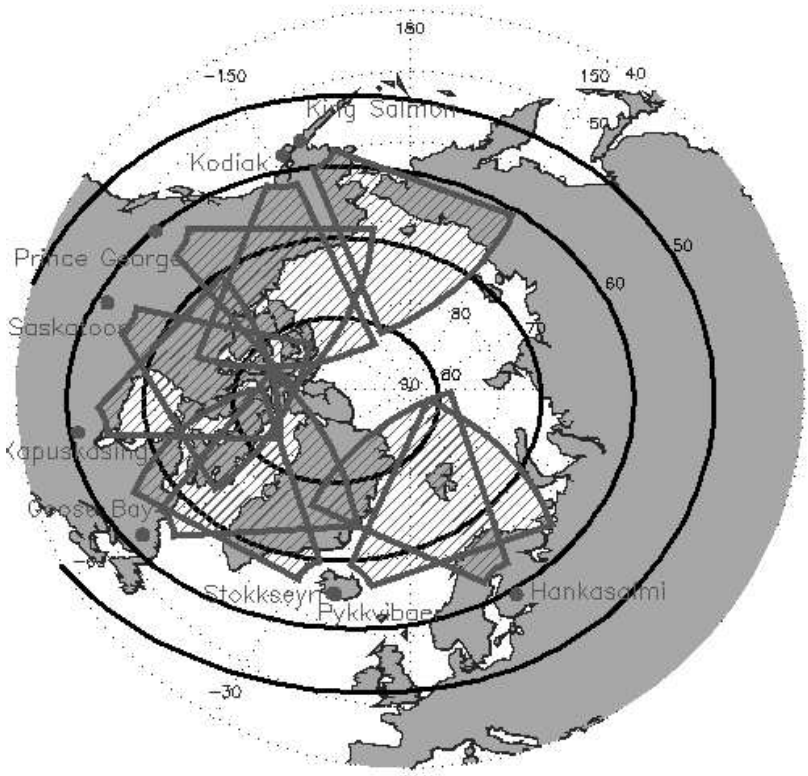

Figure 3.2: **SuperDARN coverage.** The effective areas of the radars comprising SuperDARN in the northern hemisphere. Dotted grid is geographical while solid black lines indicate geomagnetic latitudes. (Map obtained from the University of Saskatchewan web site).

optimized to provide the best determination of different quantities to the detriment of other parameters.

Quantities derivable from the radar echoes are high-resolution electron density profiles, ion and electron temperatures as a function of height, ion velocity and ion composition as a function of height and for high altitudes the electric field. With a few more assumptions the following quantities can be obtained as well: conductivities, velocity and temperature of neutrals, field-aligned currents, ionospheric currents, Joule heating, energy deposition by auroral electrons, energy spectrum of auroral electrons and gravity waves.

Incoherent scatter radars are, however, quite expensive installations. They are costly in maintenance and power expenditure and are mostly run in campaign modes, i.e. they do not provide continuous data.

3.6 All-sky cameras

An all-sky camera is a TV camera mounted with a fish-eye lens so that the field-of-view covers most of the overhead sky. It provides detailed pictures of the auroral morphology and dynamics.

3.7 Photometers

Photometers are optically designed to detect light emissions at a specific wavelength. Typical auroral wavelengths monitored are the [O I] 630.0 nm line and the N_2^+ 427.7 nm band because their relative intensities correlate with the hardness of the energy spectrum of precipitating electrons (Rees & Luckey 1974).

3.8 Polar ionospheric X-ray imaging experiment

The Polar ionospheric X-ray imaging experiment (PIXIE) was the first, and still is the only, detector to provide images of the entire terrestrial X-ray aurora in a hemisphere. Global X-ray imaging adds to our understanding of the large-scale behaviour of energetic electron precipitation. PIXIE is a gas detector mounted on a non-spinning platform on the Polar satellite. Polar is a NASA (National Aeronautics and Space Administration) satellite which was part of the International Solar-Terrestrial Physics (ISTP) programme, a collaboration between NASA, ESA (European Space Agency) and the space research institutes of Japan and Russia. NASA discontinued ISTP in late 2001, and the operation of the Polar satellite continues on a drastically reduced mission operations budget.

PIXIE consists of a double pinhole camera integrated into one unit. Each camera has four different pinhole-plate settings to optimize the configuration for different parts of the highly elliptic Polar orbit which has perigee at 1.8 R_E and apogee at 9 R_E radial distance. At perigee the auroral oval subtends a large solid angle and the perigee setting of the aperture plates are designed to let X-rays pass through only two pinholes so as to ensure non-overlapping images on the detector. At higher altitude the auroral oval has a small solid angle and more pinholes are desirable, as long as the images on the detector do not start to overlap. In the data processing the simultaneous images are added to increase the signal-to-noise ratio. In addition to the number of pinholes, the pinhole size can be varied. Larger pinholes give higher sensitivity, but lower spatial resolution.

The gas detector has two chambers each with two proportional counters. The front chamber contains Ar and has a 0.1 mm Be window, making it sensitive to 2–12 keV X-rays. The rear chamber is filled with Xe, has a 2 mm Be window and is sensitive to 10–60 keV X-rays. Both chambers has 10% CO_2 mixed in with the noble gas to avoid uncontrolled ionization. Each counter has 64 energy channels, but in reality these have to be binned further to improve the signal-to-noise ratio. Since the auroral intensity decreases rapidly with energy, there are very few atmospheric X-rays in the highest energy channels making these very susceptible to background noise and fluorescence. Therefore it is practical to bin the obtained spectra into six energy bands: four from the front chamber and two from the rear, covering approximately 3–22 keV (Østgaard et al. 2000; Østgaard et al. 2001).

Time resolution can easily be set individually for events depending on the X-ray intensity. PIXIE provides a high time resolution, but to obtain an acceptable signal-to-noise ratio, integration times of a least one minute, usually more, are needed, except for perigee passes where time resolutions down to 10 s are attainable. Spatial resolution varies greatly along the orbital path from roughly 1000 km at apogee to 150 km at perigee. The spatial resolution depends on distance to the source and pinhole size. In addition a certain wobbling of the spacecraft smears the image in one direction, effectively lowering the resolution.

Problems with the high-voltage power supply in the front chamber was resolved by introducing duty cycles where the power supply would be turned off at regular intervals, e.g. a few minutes on, a few minutes off, etc. Continuous coverage of events is thus provided only by the rear chamber.

Unfortunately, as of late September 1998 the rear chamber no longer provides data.

The detector design is described by Imhof et al. (1995) and data processing is described by Østgaard et al. (1999a) and Thorsen (1998).

3.9 The UV imager on Polar

Also mounted on the de-spun platform of the Polar satellite is the Ultraviolet Imager (UVI) (Torr et al. 1995). It is equipped with advanced filter technology designed to separate the observations into wavelength regions that can later be combined to obtain auroral characteristics.

Special filters for UVI are designed so that the N_2 Lyman-Birge-Hopfield band

measurements are split into two parts: one at shorter wavelengths (LBHs) which is strongly affected by the O_2 Schumann-Runge absorption continuum, and another at longer wavelengths (LBHl) where O_2 absorption is less significant.

The dominant excitation mechanism of the forbidden N_2 LBH emissions is by electron impact. Electrons of higher energies will penetrate deeper into the atmosphere so that the emissions will occur at lower altitudes and thus be more susceptible to absorption as the O_2 abundance increases with depth. Combining measurements from the two UVI bands allows characterization of the electron differential energy spectrum for an assumed spectral form (e.g. Maxwellian) as demonstrated by Germany et al. (1997). The technique is described in further detail by Germany et al. (1994a; 1994b).

UVI also has special narrowband filters for the two characteristic O I lines at 130.4 and 135.6 nm. The latter can be combined with LBHl instead of LBHs to derive the electron energy spectrum, but the O I line is more sensitive to changes in N_2 density and compositional changes (Germany et al. 1997), so using the two LBH bands is a more robust method. UVI is also equipped with a filter at 190.0 nm which monitors the contamination from scattered sunlight.

The detector is a cooled CCD (charge-coupled device). The instrument can be run in different modes, cycling through a number of selected filters and including background measurements. The integration time is 36 s in each filter, so this is the maximum time resolution, requiring a single-filter mode. More usual is a 3–4 minute cycle.

When Polar is at an altitude above 6 R_E (half the time) the 8° UVI field-of-view covers the entire auroral oval. The spatial resolution of the instrument is about 30–40 km, depending an altitude. The spacecraft jitter, however, smears the images about 200-300 km in one direction, at these altitudes.

3.10 Solar wind probes

Being the energy source and the driver (directly or otherwise) in many magnetospheric processes and ionospheric phenomena, the solar wind is an essential target for monitoring. Solar wind satellites monitor electromagnetic fields, plasma parameters, waves and energetic particles. Solar wind probes are either in high-altitude orbits, which will bring the spacecraft into the magnetotail at intervals, or located in the first Lagrange point, L1, a stable gravitational minimum some 200 R_E upstream. L1 has the advantage of continuous solar wind monitoring, but

the distance is substantial. There is no guarantee that all perturbations detected by a probe at L1 will impact the magnetosphere.

Three current satellites provide crucial solar wind data. IMP-8 (Interplanetary Monitoring Platform)was launched in 1973 into a near-circular 35 R_E orbit and is still operational. Wind was launched in 1994. It does not have a fixed orbit. In the beginning the orbits were highly elliptical with 50–250 R_E radial distance. Later it resided at L1 for a while, and in 1998 the orbit was changed to an out-of-the-ecliptic configuration. ACE (Advanced Composition Explorer) was launched in 1997 and monitors the solar wind from the vantage point of L1.

Advance warnings of solar activity are obtainable by monitoring the Sun itself. SOHO (Solar and Heliospheric Observatory) launched in 1995 and situated at L1 is equipped with a host of instruments monitoring the solar corona and probing the solar interior.

3.11 Geosynchronous monitors

The geosynchronous orbit is excellent for monitoring the state of the magnetosphere. Satellites residing here are able to monitor the outer radiation belts and observe substorm signatures such as particle injections and magnetic field dipolarization. They are also used to detect solar X-ray events and classify solar flares. The most important satellites are the GOES (Geostationary Operational Environmental Satellites) and the LANL (Los Alamos National Laboratories) satellites. Currently five of each are in operation, distributed at different local times.

3.12 Low-Earth orbiting satellites

Monitoring of particles, waves and electromagnetic fields from low-Earth orbit, especially from polar orbits, is important for our knowledge of the high-latitude ionosphere and the magnetospheric regions connected to it. Such observations are provided by the DMSP (Defence Meteorological Satellite Program) polar orbiters of which there are currently four, and by the first two satellites of NASA's Small Explorers (SMEX): SAMPEX (Solar Anomalous and Magnetospheric Particle Explorer) launched 1992 and FAST (Fast Auroral Snapshot Explorer) launched 1996.

The Ørsted satellite launched in 1999 is a geomagnetic mission which is dedicated to measuring the Earth's magnetic field with unprecedented high precision.

TRACE (Transition Region and Coronal Explorer) is another SMEX low-Earth orbiting satellite launched in 1998. It is a solar imager using narrowband filters to observe the high-temperature domains of the Sun where luminous plasma traces out the solar magnetic field lines.

Radio occultation, limb sounding or atmospheric profiling is a rather new technique whereby the atmosphere and ionosphere can be probed by remote sensing. It exploits the fact that global navigation satellites like the GPS (Global Positioning Satellites) emit radio signals at two frequencies from an intermediate height (24000 km in the GPS case). A receiver on a low-Earth orbiter can detect the signals, and when one satellite as seen from the other is setting behind the Earth, the signals have travelled through the ionosphere and lower atmosphere. This modifies the signals, and parameters like the total electron content of the ionosphere and profiles of temperature, water vapour content and electron density can be obtained.

3.13 Other satellite missions

In addition to the missions mentioned above, a few high-profiled missions deserve special attention.

3.13.1 Geotail

Geotail launched in 1992 is a collaboration between the Japanese Institute of Space and Astronautical Science and NASA and was part of the ISTP programme. Initially it had an orbit with an apogee of up to 200 R_E which was kept on the nightside of the Earth allowing the spacecraft to study the distant magnetotail. In 1995 the apogee was reduced to 30 R_E to probe the near-Earth magnetotail, until then a poorly sampled region. The instruments on Geotail provide in situ data on electromagnetic fields, waves and particles which have added greatly to our knowledge of magnetospheric processes, and continue to do so.

3.13.2 IMAGE

The NASA IMAGE (Imager for Magnetopause-to-Aurora Global Exploration) satellite was launched in 2000 into an elliptical polar orbit with a perigee altitude of 1000 km and an apogee altitude of 7.2 R_E. It carries extreme and far UV imagers, a radio imager and a new type of instrument: neutral atom imagers sensitive

to particles in three different energy ranges. The specially designed Lyα filter on the FUV instrument for observing the proton aurora was described in Section 2.5. IMAGE science objectives include investigation of the dominant mechanisms of particle injections into the magnetosphere and the energization, transportation and loss of magnetospheric plasmas during storms and substorms.

3.13.3 Cluster II

Cluster together with SOHO was an ESA cornerstone mission. Cluster comprised four satellites that were to fly in variable configurations exploring the three-dimensional structure of magnetospheric regions. The 1996 launch was a disaster turning the four eagerly awaited scientific satellites into extremely expensive fireworks when the Ariane 5 rocket exploded.

A new spacecraft was assembled from spare parts, and in 1997 ESA decided to rebuild another three identical satellites and go ahead with the mission now renamed Cluster II. In 2000 the four satellites were successfully launched on two different rockets. They are in nearly identical orbits with perigee at 4 R_E and apogee at 19.6 R_E. The separation of the spacecraft can be adjusted to fit the spatial scales of interest in different regions and vary from a few hundred km to a few R_E. Each of the four satellites are equipped with 11 instruments for in situ measurements of electromagnetic fields, waves and particles. Observing the magnetosphere with identical instruments on four satellites gives a unique opportunity to study three-dimensional and time-varying structures since the classic problem of distinguishing between spatial and temporal variations can be overcome.

3.14 Conclusion

Vast data resources are available to the space physics community through easily accessible databases, but in order to be able to properly analyze and interpret these data intimate knowledge of instruments and detection techniques are crucial. For the work presented in the following chapters the most important properties are those of the imaging riometer and the global X-ray and UV imagers on the Polar satellite: PIXIE and UVI. Data from a solar wind probe, geosynchronous monitors and the Geotail spacecraft are also included in the research.

Chapter 4

Electron spectra from X-ray spectra

In the pursuit of further knowledge about magnetospheric processes an important source of information is the distribution of electrons in energy and space. In situ measurements of electron energy spectra in the auroral zone can not feasibly be done on large spatial scales, and for the magnetosphere such an objective is even farther beyond reach. Particle measurements done by polar orbiting satellites will provide a few minutes of data from the auroral zone during each orbit of the order of 100 minutes. For global monitoring and long time coverage of the auroral oval remote sensing techniques from satellites are utilized to characterize the auroral electrons.

Apart from a few K-shell emission lines at low energies, atmospheric X-rays are solely produced by energetic electrons. No contamination exists from either sunlight, airglow or precipitating protons. Hence, X-ray remote sensing provides a useful diagnostic of the energetic part of the precipitating electrons. The X-ray spectrum and the electron spectrum are not simply related, though. The electrons are subject to energy loss and angular scattering through Coulomb collisions. The energy spectrum and angular distributions of photons emitted in the bremsstrahlung process depend on the distribution function of the electrons. After emission the X-ray photons are subject to absorption and scattering, especially if they propagate in a downward direction.

Most authors when deriving electron spectra from observed X-ray spectra have utilized previously tabulated meticulous theoretical calculations of X-ray spectra based on a variety of input electron spectra, but such a method is dependent on assumptions about the shape of the incident electron spectrum. In order to avoid such a presupposition this work employs a direct inversion technique which is presented and validated in this chapter with the purpose of enabling a better char-

acterization in the future of the precipitating electrons by possible X-ray imagers such as the solid state detector (Budtz-Jorgensen et al. 2001) which was part of the Atmospheric X-ray Observatory (proposed by Torsten Neubert for the Danish Small Satellite Programme) and a worthy successor to PIXIE.

4.1 Bremsstrahlung from precipitating electrons

Rees (1964a) calculated X-ray fluxes as a function of height and X-ray energy for a number of monoenergetic and Maxwellian input electron spectra. The energy dissipation as a function of height is dependent on the angular distribution of incident electrons (Rees 1963) which was considered isotropic over the downward hemisphere. The calculations of the penetration depth of electrons are carried out for a geomagnetic latitude of 67°, but the effect of the magnetic field is small (Rees 1964b). The non-relativistic theory of Sommerfeld is used for evaluation of the total X-ray production cross section, but even with a screening correction applied this theory is problematic for electron energies above a few keV (Koch & Motz 1959). The angular distribution of X-ray emissions was treated separately by multiplication by a simple angular distribution function (see Eq.(4.12)). At each height interval the bremsstrahlung emission was calculated for the upward and for the downward hemisphere, but these were added before tabulation, reporting only the omnidirectional bremsstrahlung emission, because the final goal was a calculation of the effect on ionization profiles.

A more rigorous approach was taken by Berger & Seltzer (1972) who performed Monte Carlo simulations of bremsstrahlung in the atmosphere. Their calculations were based on previous stringent Monte Carlo simulations of energy deposition by auroral electrons (Berger et al. 1970) and included multiple scattering (elastic and inelastic) of electrons, production of secondary electrons, X-ray bremsstrahlung production and multiple Compton scattering and photoelectric absorption of X-ray photons. In a treatment like this drastic approximations are avoided and the accuracy is mainly limited by the cross section values available for the different processes. Berger & Seltzer (1972) used the Sauter cross section with the Elwert correction factor for calculating the bremsstrahlung production. This cross section is described in Section 4.3 below. Resulting bremsstrahlung flux spectra from incident monoenergetic electron beams are tabulated for three optical depths typical of balloon heights (30–40 km). Based on the monoenergetic results examples of bremsstrahlung flux spectra from incident exponential elec-

tron spectra are calculated and shown graphically. Seltzer & Berger (1974) treated the case of zero atmospheric depth, i.e. the bremsstrahlung spectra seen at satellite altitudes. Values for monoenergetic electrons beams are tabulated and graphs are shown for exponential electron spectra. The angular distribution of the resultant X-ray energy spectra is unfortunately not presented.

Luhmann (1977) showed that certain approximations in the treatment of the electron transport still yields results comparable with those of Berger & Seltzer (1972) with greatly reduced computational efforts. The approximations (neglecting pitch angle scattering and magnetic focusing) to the time-dependent Fokker-Planck equation, which describes transport of a uniform primary electron beam of infinite extent in a plane-parallel atmosphere with a converging magnetic dipole field, are described by Luhmann (1976).

Luhmann (1977) used the Bethe-Heitler X-ray production cross section, differential in photon energy (Koch & Motz 1959, Formula 3BN), and included the angular distribution in a manner similar to Rees (1964a). Photoelectric absorption was taken into account, and Compton scattering was treated as an absorption process, even though it only redistributes the photon energy. In their calculations of soft auroral X-ray emissions at satellite altitude Luhmann & Blake (1977) included contributions from K shell line emissions from nitrogen and oxygen at 0.396 and 0.525 keV, respectively, showing that these can be comparable in intensity to the bremsstrahlung continuum at these energies.

Walt et al. (1979) employed a rigorous method for computing the directional bremsstrahlung flux at satellite altitudes. The calculations were divided into three steps: electron diffusion, bremsstrahlung production and photon diffusion and escape. The electron energy spectrum and angular distribution as a function of height was obtained from an incident electron flux of arbitrary energy and angular distribution by numerical integration of the Fokker-Planck equation. It was assumed that bremsstrahlung production takes place in a thin layer. The authors conclude that the altitude is not very important as long as it is above the region of photon absorption. The Sauter cross section with the Elwert correction factor was used to evaluate the bremsstrahlung production. Upward emitted X-rays were assumed to escape unhindered. The diffusion of downward emitted photons were treated with a Monte Carlo approach taking into account photoelectric absorption and coherent and incoherent scattering. The contribution of originally downward emitted photons to the resulting upward X-ray flux was included.

The X-ray energy spectra presented by Walt et al. (1979) are obtained for isotropic exponential incident electron spectra and give the directional photon flux

for several escape angles and different characteristic energies of the incident electron spectra. The contribution of reflected photons gives rise to a slight increase in the spectra near 50 keV, since downward emitted photons below about 20 keV are very likely to be absorbed and those of energy above 50 keV are less susceptible to being scattered at such large angles as are needed for escape. The fraction of reflected photons increases with electron energy, since the photoelectric absorption cross section decreases while the Compton scattering cross section increases with energy. For high electron energies the assumption that all X-rays are emitted at the same altitude becomes less valid. For electron spectra of characteristic energies of 100 and 200 keV the penetrating power is so great that low energy photons are subject to attenuation, the exact extent of which cannot be determined by a method where a single height is attributed to all X-rays emissions.

The authors stress the importance of considering the photon escape angle since the flux increases rapidly with zenith angle. The photons have a strong tendency for near-horizontal escape angles, and this effect is more pronounced the higher the energies of the precipitating electrons.

Some general conclusions from all these different calculations can be summarised. When the energy of the incident electrons is increased, the X-ray intensity at a given energy is increased, and the X-ray energy spectrum shifts to higher energies. Exponential incident electron spectra tend to give exponential X-ray spectra. Attenuation of the X-ray intensity is significant only for low photon energies. It is important for calculating X-rays at balloon altitudes, but mostly negligible for satellite altitudes.

4.1.1 Electron spectra from X-ray spectra

Tables such as those of Seltzer & Berger (1974) and Walt et al. (1979) can be interpolated and used to determine the precipitating electron spectra responsible for observed X-ray spectra as have been done by many authors.

A discrete ordinates code is much faster than Monte Carlo techniques, and a package has been developed to perform one-dimensional transport calculations of the fully-coupled electron-photon cascade at energies above 1 keV (Lorence 1992). This code uses the Sauter cross section for bremsstrahlung production with the Elwert-Haug correction factor (see Section 4.3). It has been run for a series of exponential incident electron spectra of characteristic energy up to 100 keV, providing look-up tables (unpublished) that have been used by Østgaard et al. (2000; 2001; 2002) and Aksnes et al. (2002) for deriving electron spectra from

PIXIE data. To emulate the high energy tail these authors used a sum of two exponential electron spectra whenever that gave a better fit to the observed X-rays than a single exponential spectrum. But even with such extensive tables the method is limited by its dependency on an assumed spectral shape and the energy range covered by the theoretical calculations.

When Smith et al. (1995) derived electron spectra from X-rays observed from a balloon over Antarctica he looked to the bremsstrahlung deconvolution technique developed for solar X-rays by Johns & Lin (1992) based on work by Brown (1971). This method does not invoke any assumed spectral shape, but requires good spectral resolution of the observed X-ray spectrum.

The method developed in this work and described in detail below was inspired by this astrophysical approach which was modified to include the angular distribution of the emitted photons. The Sauter-Elwert cross section for bremsstrahlung production was incorporated instead of the Bethe-Heitler-Elwert cross section used by Smith et al. (1995).

4.2 Deconvolution method for X-ray spectra

When considering atmospheric X-rays the source region can be viewed as relatively limited in altitude while it can be extensive in latitude and longitude. Due to the limited extent in height the source can be described as optically thin.

For satellite data absorption and scattering of X-rays is negligible, at least for photon energies greater than a few keV (Robinson & Vondrak 1994). Seltzer & Berger (1974) have calculated bremsstrahlung spectra at satellite altitudes from a Monte Carlo approach taken into account multiple Compton scattering of electrons (by atoms and orbital electrons) and photoelectric absorption and multiple Compton scattering of the X-ray photons. They find an attenuation of 10 keV photons produced by electrons with energies exceeding 400 keV. This is an effect of the fact that such energetic electrons statistically penetrate to greater depth before interacting with the atmospheric constituents. In the case of a hard electron energy spectrum, atmospheric absorption of X-ray photons below a few keV is not negligible.

Walt et al. (1979) concludes that the X-rays detected at satellite altitudes mostly comes directly from the source rather than from downward emitted and subsequently scattered photons. This is not necessarily obvious as the angular distribution of emitted photons is strongly downward directed. All in all this justifies

an approximate treatment of photon transport, and in this work photon absorption will be ignored.

X-rays from secondary electrons are considered negligible because few are produced, and those created are likely to be of low energy and emitted at low altitudes and thus very unlikely to escape the atmosphere (Robinson & Vondrak 1994).

The work of Walt et al. (1979) shows that an isotropic electron flux at the top of the atmosphere will not experience a significant change in angular distribution by scattering processes before the electron energy is greatly reduced. In the treatment of electron transport only the energy loss is taken into account while the angular distribution is assumed to remain isotropic.

Table 4.1 summarizes the notation to be used in the following. Using the assumption that X-ray production occurs in a layer that is limited in altitude extent, the density and energy distributions can be considered as non-varying with height within the layer. The X-ray emission, ε_x, from an optically thin source in the direction ξ with respect to vertically down is then

$$\varepsilon_x(\xi, k) = \int_k^\infty \int_{d\Omega_\xi} N\, j_e(E, \zeta)\, \frac{d^2\sigma}{dk\, d\Omega}\,(E, k, \theta)\, d\Omega_\xi\, dE \quad \text{\#/s/sr/keV/cm}^3, \quad (4.1)$$

where N is the number density of atmospheric constituents, j_e is the differential flux of electrons (see below), k is photon energy, E is electron kinetic energy, σ is the bremsstrahlung cross section (differential in photon energy and emission angle θ) in units of cm^2 per keV per atom per incident electron.

The $d\Omega_\xi$ refers to the integration being over angles ζ and τ after the bremsstrahlung cross section's θ dependence have been expressed in terms of ξ, ζ and τ via Eq. (4.2). The relations between the different angles are illustrated in Fig. 4.1. The internal angle, θ, between the directions of the incident electron and the emitted photon is given by

$$\cos\theta = \cos\xi \cos\zeta + \sin\xi \sin\zeta \cos\tau. \quad (4.2)$$

The differential particle flux, j, is the number of particles (here photons or electrons) that pass through a unit area perpendicular to the propagation into a unit solid angle per second per unit energy. For an optically thin source the directional photon flux is simply $j_x = \varepsilon_x s$, where s is the path length through the source. We observe the source at angle ξ with respect to vertical down. If l denotes the thickness of the source layer, the differential photon flux in this direction will be

Table 4.1: Notation and definitions

Symbol	Description
ϵ, ϵ_f	Initial and final total energy of electron
$\mathbf{p}$, $\mathbf{p}_f$	$\mathbf{p}/c$, $\mathbf{p}_f/c$ = initial and final momentum of electron
E, E_f	Initial and final kinetic energy of electron
k, $\mathbf{k}$	k, $\mathbf{k}/c$ = energy and momentum of emitted photon
θ, θ_f	Angle of $\mathbf{p}$ and $\mathbf{p}_f$ with respect to $\mathbf{k}$
ϕ	Azimuth angle between the planes ($\mathbf{p}$,$\mathbf{k}$) and ($\mathbf{p}_f$,$\mathbf{k}$)
$d\Omega_k$	Element of solid angle in the direction of $\mathbf{k}$, $d\Omega_k = \sin\theta d\theta d\phi$
ζ	Pitch angle of incident electron with respect to downward direction
ξ	Direction of emitted photon with respect to downward direction
τ	Azimuth angle between the planes defined by $\mathbf{p}$ and $\mathbf{k}$ with vertical
β, β_f	Ratio of initial and final electron velocity to velocity of light
σ	Bremsstrahlung cross section [cm^2 per atom per incident electron]
j_x, j_e	Differential particle flux of photons and electrons [#/s/sr/keV/cm^2]
Z	Atomic number of target
N	Number density of atmospheric constituents
l	Thickness of the X-ray production layer
m	Electron mass
e	Elementary charge
c	Speed of light in vacuum
mc^2	Electron rest mass = 511 keV
$\hbar$	$\hbar = h/2\pi$, h = Planck's constant
α	Fine structure constant, $\alpha = e^2/\hbar c \approx 1/137$
r_0	Classical electron radius, $r_0 = e^2/mc^2$
ε_0	Permittivity of free space

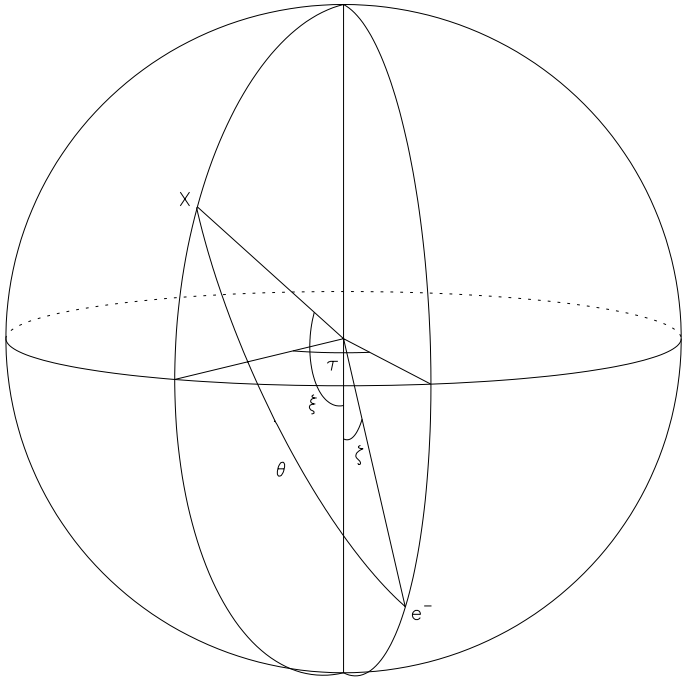

Figure 4.1: **Definition of angles in the bremsstrahlung process.** X denotes the X-ray photon and e^- denotes the incident electron. θ is the internal angle between incident electron and emitted photon directions. ζ and ξ give the directions of incident electron and emitted photon with respect to the downward direction, and τ is the azimuth angle. See also Table 4.1.

$j_x = \varepsilon_x l / \cos(\pi - \xi) = \varepsilon_x l / (-\cos\xi)$, i.e.

$$j_x(k,\xi) = \frac{Nl}{-\cos\xi} \int_k^\infty \int_0^{2\pi} \int_0^\pi j_e(E,\zeta) \frac{d^2\sigma}{dk\, d\Omega}(E,k,\xi,\zeta,\tau) \sin\zeta \, d\zeta \, d\tau \, dE. \tag{4.3}$$

If the differential electron flux is isotropic over the downward hemisphere it can be written as

$$j_e(E,\zeta) = j_e(E) f(\zeta), \quad \text{where} \quad f(\zeta) = \begin{cases} 1 & 0 \le \zeta < \frac{\pi}{2} \\ 0 & \frac{\pi}{2} \le \zeta \le \pi \end{cases} \tag{4.4}$$

and we then have

$$j_x(k,\xi) = \frac{Nl}{-\cos\xi}\int_k^\infty j_e(E)\int_0^{2\pi}\int_0^{\frac{\pi}{2}}\frac{d^2\sigma}{dk\,d\Omega}(E,k,\xi,\zeta,\tau)\,\sin\zeta\,d\zeta\,d\tau\,dE. \tag{4.5}$$

Bremsstrahlung spectra from optically thin sources will always be monotonically decreasing with increasing photon energy. Electrons of a given kinetic energy can obviously only produce photons of lower or equal energy. So if above a certain energy, k_n, there is no X-ray emission, and the maximum electron energy can be assumed to be $E_m > k_n$ then we have from Eq. (4.5)

$$j_x(k_n,\xi) = \frac{Nl}{-\cos\xi}\int_{k_n}^{E_m} j_e(E)\int_0^{2\pi}\int_0^{\frac{\pi}{2}}\frac{d^2\sigma}{dk\,d\Omega}(E,k_n,\xi,\zeta,\tau)\,\sin\zeta\,d\zeta\,d\tau\,dE. \tag{4.6}$$

If we proceed to divide the full energy range into intervals k_1,k_2,k_3,...,k_n (which could be the energy bins of observational data) and setting $E_m = k_{n+1}$ the photon flux in any interval can be written as

$$j_x(k_i,\xi) = \frac{Nl}{-\cos\xi}\sum_{j=i}^{n}\left(\int_{k_j}^{k_{j+1}} j_e(E)\int_0^{2\pi}\int_0^{\frac{\pi}{2}}\frac{d^2\sigma}{dk\,d\Omega}(E,k_i,\xi,\zeta,\tau)\,\sin\zeta\,d\zeta\,d\tau\,dE\right). \tag{4.7}$$

Since the bremsstrahlung cross section varies slowly with electron energy it is not too bad an approximation to assume that the electron flux averaged over the cross section does not differ significantly from the actual electron flux for each particular energy interval and hence

$$j_x(k_i,\xi) = \frac{Nl}{-\cos\xi}\sum_{j=i}^{n}\left(j_e(k_j\rightarrow k_{j+1})\int_{k_j}^{k_{j+1}}\int_0^{2\pi}\int_0^{\frac{\pi}{2}}\frac{d^2\sigma}{dk\,d\Omega}(E,k_i,\xi,\zeta,\tau)\,\sin\zeta\,d\zeta\,d\tau\,dE\right). \tag{4.8}$$

Note that the energy bins of the electrons are shifted relative to the energy bins of the photons. k_i denotes the centre of photon energy bins while electron energy bins start at k_i.

In the following the shorthand notation $\sigma_d(k_i)$ is used for $\frac{d^2\sigma}{dk\,d\Omega}(E,k_i,\xi,\zeta,\tau)$. Equation (4.8) can be written on matrix form:

$$\mathbf{G}\mathbf{J}_\mathbf{e} = \mathbf{J}_\mathbf{x}, \tag{4.9}$$

$$\text{where} \qquad \mathbf{J_e} = \begin{Bmatrix} j_e(k_1 \rightarrow k_2) \\ j_e(k_2 \rightarrow k_3) \\ \vdots \\ j_e(k_n \rightarrow k_{n+1}) \end{Bmatrix}, \qquad \mathbf{J_x} = \begin{Bmatrix} j_x(k_1, \xi) \\ j_x(k_2, \xi) \\ \vdots \\ j_x(k_n, \xi) \end{Bmatrix} \qquad \text{and}$$

$$\mathbf{G} = \begin{Bmatrix} \int_{k_1}^{k_2}\int_{\Omega} \sigma_d(k_1) d\Omega dE & \int_{k_2}^{k_3}\int_{\Omega} \sigma_d(k_1) d\Omega dE & \cdots & \int_{k_n}^{E_m}\int_{\Omega} \sigma_d(k_1) d\Omega dE \\ 0 & \int_{k_2}^{k_3}\int_{\Omega} \sigma_d(k_2) d\Omega dE & \cdots & \int_{k_n}^{E_m}\int_{\Omega} \sigma_d(k_2) d\Omega dE \\ \vdots & \vdots & \ddots & \vdots \\ 0 & 0 & 0 & \int_{k_n}^{E_m}\int_{\Omega} \sigma_d(k_n) d\Omega dE \end{Bmatrix}.$$

This is as a well-determined discrete linear inverse problem and is easily solved. By using singular value decomposition of $\mathbf{G}$ (instead of backsolving or direct matrix inversion) the error propagation is minimized. First, however, $\mathbf{G}$ must be calculated.

4.3 Bremsstrahlung cross sections

Calculating the cross section for the bremsstrahlung process, in which an electron is decelerated in the field of an atomic nucleus, is no straightforward matter. It involves the evaluation of the matrix element for the transition of the system from an initial state before photon emission to a final state after emission. For this the wave functions describing an electron in a screened Coulomb field are needed. The difficulty of solving the Dirac wave equation arises primarily because the wave function must be represented as an infinite series.

In cross-section calculations approximations are therefore used, such as the Born approximation or the Sommerfeld-Maue wave functions. The Born approximation gives relatively simple analytical formulae, but becomes less accurate for heavy target nuclei, for low initial electron energies and for the high-frequency limit where the photon energy approaches the kinetic energy of the incoming electron.

A nice review of cross section formulae is found in Koch & Motz (1959). The emphasis, however, is mainly on intermediate to high electron energies (the MeV region).

Elwert & Haug (1969) derives a rather complicated formula for the bremsstrahlung cross section differential in photon energy and in photon and electron

emission angles using Sommerfeld-Maue wave functions. In the limit of low energies it reduces to Sommerfeld's nonrelativistic result, at high energies it reduces to a result of Bethe and Maximon and for low $Z\alpha/\beta$[1] it reduces to the formula of Bethe, Heitler, Sauter and Racah differential in photon energy and photon and electron emission angles.

Accurate calculations based on partial-wave calculations are given by Lee et al. (1976) and Tseng et al. (1979) for electron energies of 1–500 keV, but the tabulations are unfortunately not adequately extensive for the purpose of this work.

Here will be used a cross section differential in photon energy and angle, deduced under the Born approximation without screening, denoted the Sauter cross section, given in Eq. (4.10) below. When modified with the Elwert factor (Eq. (4.11)) this gives results for the bremsstrahlung energy spectrum at keV energies no worse than the Elwert & Haug (1969) results. The latter, however, gives a more accurate angular distribution.

4.3.1 Born approximation cross sections

Johns & Lin (1992) use the Bethe-Heitler cross section differential in photon energy and assume that X-ray emission occurs isotropically. But the emission of X-ray photons is highly asymmetric and must be taken into account, so here the Sauter cross section (presented below in Eq. (4.10)) differential in photon energy and angle is used. Both are subject to the same shortcomings, however, due to the Born approximation and use of a non-screened potential. Some of these shortcomings have given rise to correction formulae.

Coulomb correction

For the nonrelativistic Bethe-Heitler cross section a Coulomb correction formula was developed by Elwert (1939). This so-called Elwert factor, f_E is given in Eq. (4.11).

$$f_E = \frac{\beta\left(1-\exp\left(\frac{-2\pi\alpha Z}{\beta}\right)\right)}{\beta_f\left(1-\exp\left(\frac{-2\pi\alpha Z}{\beta_f}\right)\right)} \tag{4.11}$$

[1] See Table 4.1 for definitions of symbols.

$$\frac{d^2\sigma}{dk\,d\Omega_k}(E,k,\theta) = \frac{\alpha Z^2 r_0^2}{8\pi}\frac{1}{k}\frac{p_f}{p}\times$$
$$\left\{\frac{8\sin^2\theta\,(mc^2)^4\,(2\epsilon^2+m^2c^4)}{p^2\Delta^4} - \frac{2m^2c^4\,(5\epsilon^2+2\epsilon\epsilon_f+3m^2c^4)}{p^2\Delta^2}\right.$$
$$-\frac{2m^2c^4\,(p^2-k^2)}{Q^2\Delta^2} + \frac{4\epsilon_f m^2C^4}{p^2\Delta} + \frac{m^2c^4L_1}{pp_f}\times$$
$$\left[\frac{4\epsilon\sin^2\theta\,(3km^2c^4-p^2E_f)\,m^2c^4}{p^2\Delta^4} + \frac{4\epsilon^2\left(\epsilon^2+\epsilon_f^2\right)}{p^2\Delta^2}\right.$$
$$\left.+\frac{2\,(mc^2)^4 - 2m^2c^4\left(7\epsilon^2-3\epsilon\epsilon_f+\epsilon_f^2\right)}{p^2\Delta^2} + \frac{2k\,(\epsilon^2+\epsilon\epsilon_f-m^2c^4)}{p^2\Delta}\right]$$
$$\left.-\left(\frac{4m^2c^4L_2}{p_f\Delta}\right) + \left(\frac{m^2c^4L_3}{p_fQ}\right)\left[\frac{4m^2c^4}{\Delta^2} - \frac{6k}{\Delta} - \frac{2k\,(p^2-k^2)}{Q^2\Delta}\right]\right\}, \quad (4.10)$$

where $\epsilon = E + mc^2$, $\epsilon_f = E_f + mc^2$, $\Delta = \epsilon - p\cos\theta$,

$$Q^2 = p^2 + k^2 - 2pk\cos\theta, \quad L_1 = \ln\left(\frac{\epsilon\epsilon_f - m^2c^4 + pp_f}{\epsilon\epsilon_f - m^2c^4 - pp_f}\right),$$

$$L_2 = \ln\left(\frac{\epsilon_f + p_f}{\epsilon_f - p_f}\right), \quad \text{and} \quad L_3 = \ln\left(\frac{Q+p_f}{Q-p_f}\right)$$

It is valid in the nonrelativistic regime ($E \ll 511$ keV), but it is not valid at the high-frequency limit ($k \to E$). Koch & Motz (1959) states that as a rough guide it can be expected to give results accurate to within 10% for electron energies below 100 keV.

No satisfactory Coulomb correction factor has been developed for intermediate energies. Several authors tend to use the Elwert factor also for this regime, as it can be seen to improve the accuracy of the cross section.

High-frequency-limit corrections

The Sauter cross section becomes infinitely small as the photon energy approaches the electron energy. Experiments indicate, however, that the cross section has a finite value at this limit (Koch & Motz 1959). Calculations in good agreement with experimental values of the high-frequency limit have been carried out by Fano et al. (1958) and Elwert & Haug (1969) but results for only a very limited number of energies are listed by the authors.

An analytical formula is cited by Koch & Motz (1959) which is accurate to within 20%. Here the simpler approach of Johns & Lin (1992) will be used instead: an extrapolation technique where the cross section evaluated at the three points k = 0.85E, 0.89E, and 0.93E are fit to an exponential function[2] which then provides values for the cross section at photon energies between 0.93E and E. For θ = 0° the Sauter cross section at the high-frequency limit is still zero, (because it is proportional to $\sin^3\theta$) in disagreement with experimental data.

Screening corrections

Screening becomes important in the extreme-relativistic limit, $E \gtrsim 5$ MeV, and in the nonrelativistic limit, $E \lesssim 10$ keV (Koch & Motz 1959). In the nonrelativistic regime no satisfactory correction has been obtained. Screening effects are also important in the low-frequency limit where $K \leq 0.1E$.

4.3.2 Comparison of Sauter and Bethe-Heitler cross sections

An example of the Sauter cross section as a function of photon energy for electron energies of 50 keV and 500 keV at four different internal angles is shown in Fig. 4.2. For lower electron energies the Elwert correction factor becomes ever more important. The Sauter cross section in the low-energy regime explored here suffers from significant deviation from experimental results.

As the Elwert correction factor was not developed for a cross section differential in photon angle one might speculate if one were better off using the Bethe-Heitler cross section multiplied by a simplified angular distribution, $f(\theta)$, like the one used by Rees (1964a):

$$f(\theta) = \frac{\sin^2\theta}{(1-\beta\cos\theta)^4}. \tag{4.12}$$

The angular distribution of the Sauter cross section is in Fig. 4.3 compared to the Bethe-Heitler cross section times $f(\theta)$ in a polar plot showing the dependence on photon emission angle ξ assuming an isotropic angular distribution of incident electrons over the downward hemisphere. The angular distribution of Eq. (4.12) predicts even less emission at upwards angles than the Sauter cross section, specially for the higher electron energies. It seems prudent to choose the more ac-

[2] Johns & Lin (1992) uses a linear fit which is more appropriate for the Bethe-Heitler cross section.

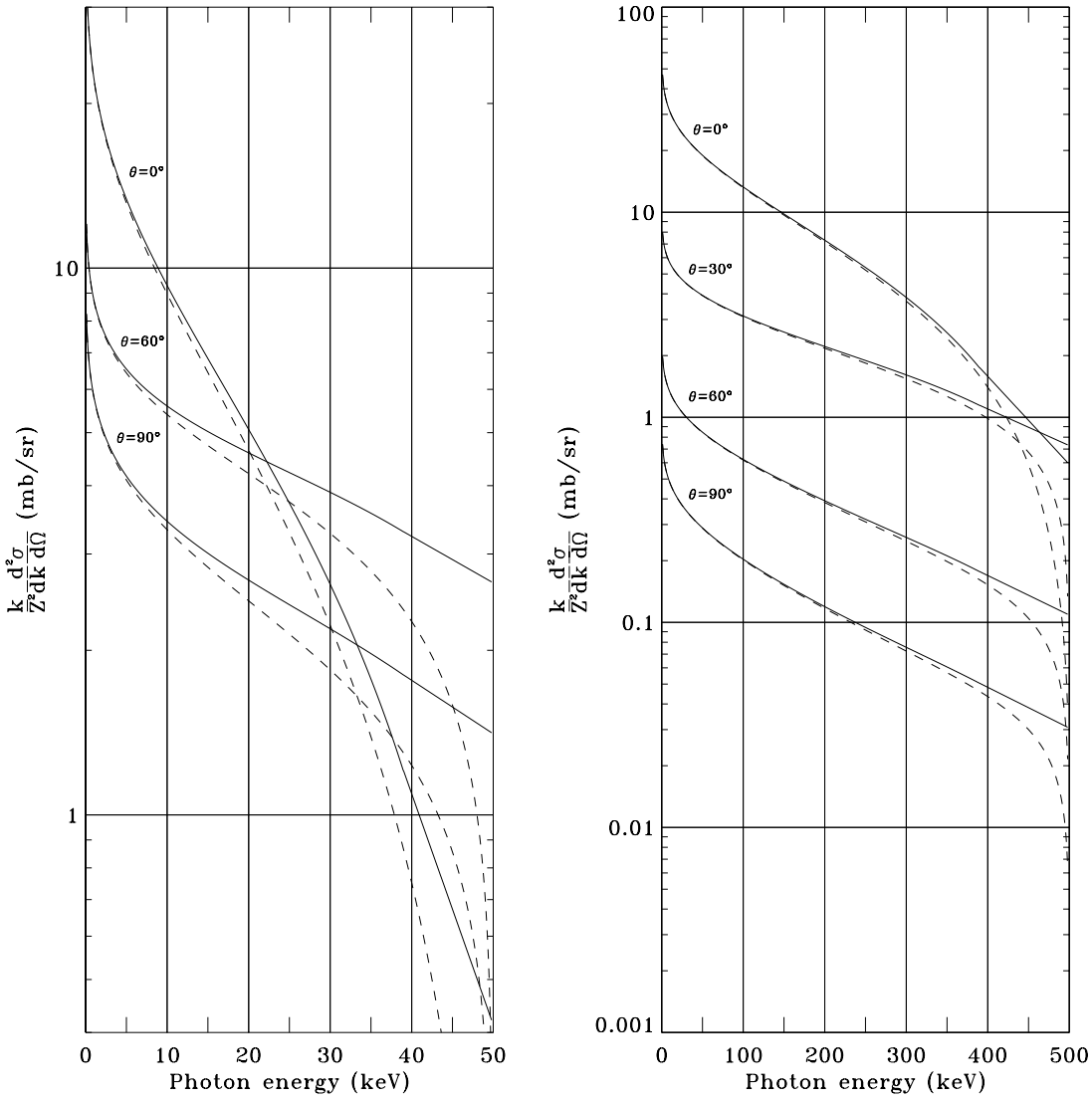

Figure 4.2: **The Sauter cross section as a function of photon energy.** The **dashed lines** show the Sauter cross section as given in Eq. (4.10), while the **solid lines** include the Elwert correction factor (Eq. (4.11)) and a high-frequency limit extrapolation. The differential cross section is multiplied by the factor k/Z^2 and is in units of mb/sr (where mb is millibarn; barn = 10^{-28} m^2). **Left panel:** for an electron energy of 50 keV and θ = 0°, 60° and 90°. **Right panel:** for an electron energy of 500 keV and θ = 0°, 30°, 60° and 90°.

curate Sauter cross section for the present work where emission angles close to zenith are important.

In Fig. 4.4 the Sauter cross section integrated over all angles is compared to the Bethe-Heitler cross section. Both are corrected by the Elwert factor. The Bethe-Heitler-Elwert cross section is known to fit experimental data most accurately at electron energies below 100 keV and to underestimate the actual values at energies of the order of the electron rest mass ($\sim$500 keV). The cross sections are evaluated for Z = 7.2, appropriate for the present calculations. The comparison shows the integrated Sauter cross section to lie slightly above the Bethe-Heitler cross section without large discrepancies. This gives confidence that the former is no less accurate than the latter, perhaps even slightly better. The main difference between the two seems to be in the angular distribution.

4.4 Electron spectra from X-ray spectra

A test photon spectrum ($\propto\ k^{-2}$ up to energy k_m and zero above) and the result after employing the method outlined above is shown in Fig. 4.5 (top panel). The deconvoluted electrons display an unrealistic behaviour at the high energy end: The highest energy bin has very high flux while the next several lower energy bins have negative energy. This happens because of the unphysical assumption that the photon spectrum suddenly drops to zero flux. k_m represents a detection threshold, not an actual drop of the flux to zero, which means that while there are still photons above this limit, they are not registered due to detector sensitivity.

This can be amended by extending the photon spectrum by extrapolating from a power law fit to the two highest energy data points, as done by Johns & Lin (1992). When the contribution to the observed X-ray spectrum from higher energy electrons is taken into account in this way, the result is much improved, see Fig. 4.5 (bottom panel).

4.4.1 Relating X-ray producing and precipitating electrons

The electron spectrum obtained by solving Eq. (4.9) is the photon-producing electron spectrum. This is related to the precipitating electron spectrum at the top of the atmosphere by a continuity equation (Johns & Lin 1992):

$$\frac{dN_e(E,t)}{dt} = F(E,t) - \frac{N_e(E,t)}{\tau_e(E)} - \frac{d}{dE}\left(N_e(E,t)\frac{dE}{dt}\right), \qquad (4.13)$$

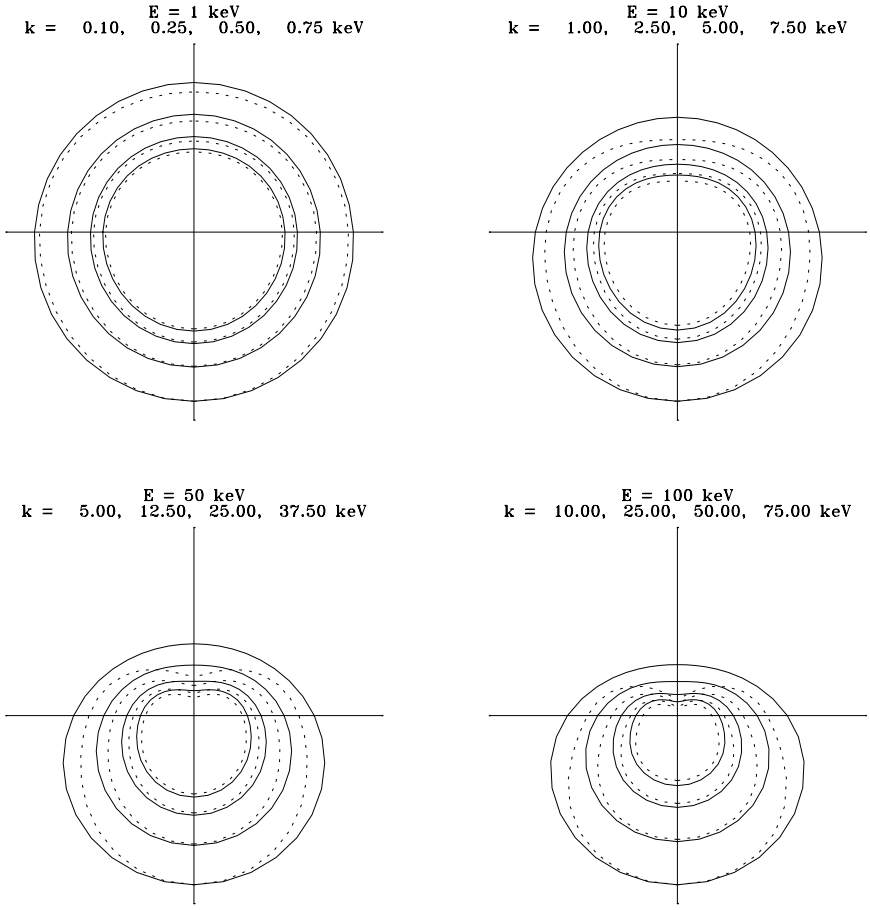

Figure 4.3: **Angular distribution of X-ray production cross section.** Dependence of the X-ray production cross section on the photon emission angle, ξ, for electron energies of 1, 10, 50 and 100 keV for panels 1–4, respectively. In each panel the angular distribution for photon energies corresponding to 10, 25, 50 and 75% of the electron energy are shown. The lowest photon energy gives the highest cross section and is outermost. An electron angular distribution isotropic over the downward hemisphere was assumed. **Solid line:** Sauter cross section normalized to the cross section in the nadir direction ($\xi = 0°$) for the lowest k in each panel. **Dotted line:** Bethe-Heitler cross section multiplied by the angular distribution of Eq. (4.12) normalized to the value in the nadir direction ($\xi = 0°$) for the lowest k in each panel.

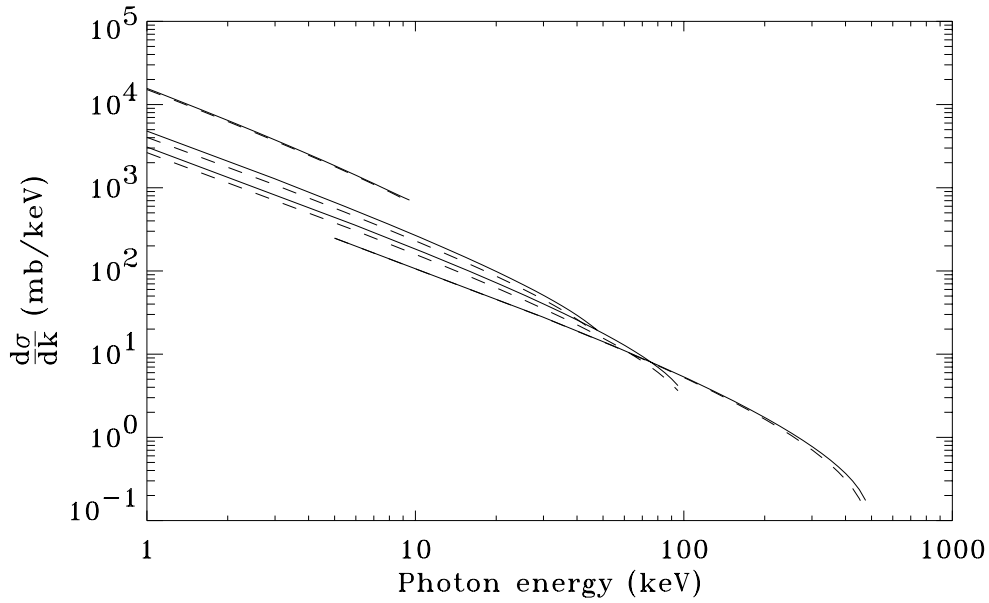

Figure 4.4: **X-ray production cross section. Solid line:** Sauter cross section with Elwert correction factor integrated over all angles. **Dashed line:** Bethe-Heitler cross section with Elwert correction factor. The line pairs are (from the top) for electron energies of 10, 50, 100, and 500 keV respectively. The cross sections were evaluated for Z = 7.2.

where $N_e(E,t)$ is the total bremsstrahlung-producing electron population in electrons/keV, $F(E,t)$ is the precipitating electron spectrum in electrons/keV/s and τ_e is the electron optical depth.

The second term on the right-hand side refers to electron escape from the X-ray production layer which can be neglected ($\tau_e \rightarrow \infty$). If in addition the assumption that the precipitating electron spectrum varies slowly compared to the stopping time of electrons in the atmosphere is imposed, we have a steady state continuity equation:

$$F(E) = \frac{d}{dE}\left(N_e(E)\frac{dE}{dt}\right). \tag{4.14}$$

We can get an expression for dE/dt by rewriting it as dE/dx multiplied by the velocity v. dE/dx is the total energy loss per unit length and if we assume this to be dominated by collisions it is described by formulae (13.14) and (13.19) of Jackson (1998). Converted to SI units they read:

$$\frac{dE}{dx} = NZ\frac{e^4}{4\pi\varepsilon_0^2 mc^2\beta^2}\left(\ln(B_q) - \beta^2\right), \tag{4.15}$$

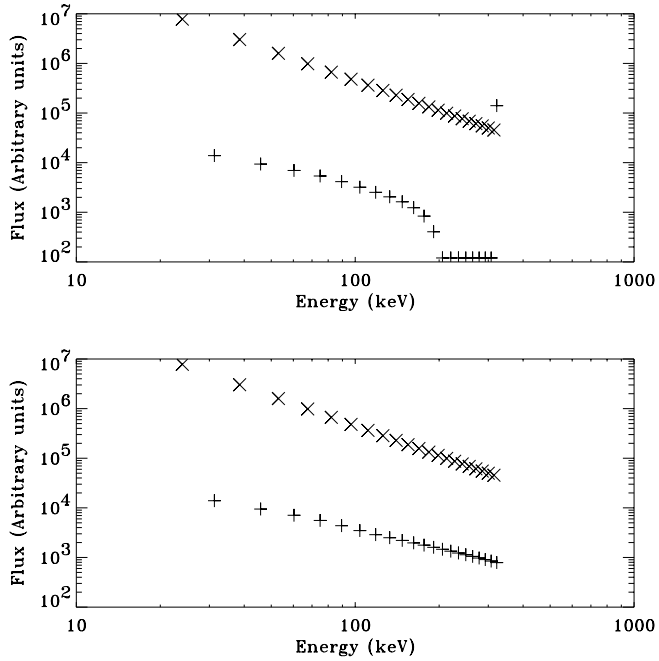

Figure 4.5: **Deconvolution examples of test spectra. Crosses:** input spectrum of X-ray photons $\propto \ k^{-2}$. **Plus signs:** deconvoluted electron spectrum. **Top panel:** 20 input photons and the resulting electron spectrum. **Bottom panel:** The photon spectrum was extended by an additional 50 points by extrapolation of the power law. Only data points and deconvoluted electrons in the region of interest (the first 20 bins) are shown.

$$\text{where} \qquad B_q = \frac{\sqrt{2}\,\gamma\beta\sqrt{\gamma-1}\,mc^2}{\hbar\,\langle\omega\rangle}, \tag{4.16}$$

where γ is the relativistic factor, $\gamma = 1/\sqrt{1-\beta}$ and $\langle\omega\rangle$ is the average harmonic binding frequency. These formulae contain the essentials of Niels Bohr's classical energy loss formula (Bohr 1915; Bohr 1948). In the calculations the value $\hbar\,\langle\omega\rangle$ = 86 eV is used.

In this work we are interested in the electron spectrum per unit area and per unit solid angle, so we assume that the electrons maintain an angular distribution that is isotropic over the downward hemisphere and that horizontal transport is negligible. Let $f(E)$ be the precipitating electron spectrum in electrons/keV/cm^2/s/sr and $n_e(E)$ the column population of X-ray producing electrons, then

$$f(E) = \frac{d}{dE}\left(n_e(E)\frac{dE}{dt}\right) = \frac{d}{dE}\left(j_e(E)\frac{l}{v}v\frac{dE}{dx}\right) = \frac{d}{dE}\left(j_e(E)l\frac{dE}{dx}\right). \tag{4.17}$$

Since $J_e \propto 1/(Nl)$ and $dE/dx \propto N$ both N and l cancel out of the calculations. The atoms responsible for the electron energy loss are the same that are available to the bremsstrahlung process.

4.5 Validation

The investigation and improvements of the Smith et al. (1995) method were initiated to be able to obtain electron energy spectra without imposing an assumed spectral shape. This was done in preparation for the next Danish small satellite to follow in the foot steps of Ørsted which, it was hoped, were to fly a payload including an atmospheric X-ray imager (Budtz-Jorgensen et al. 2001). In the meantime the method had to be validated by using available X-ray data, and the current PIXIE mission was an obvious source.

Observational data from PIXIE has been projected down to 100 km altitude. Spectra has been made for a circular region with radius 370 km centred on the location of the riometer in Kangerlussuaq (STF). In Figs. 4.6–4.9 are presented data from 12 March 1998 and in Figs. 4.10–4.13 from 15 March 1998. To get a reasonable noise level integration times of about four minutes are used and the data are divided into six energy bins. The noise level, indicated by one sigma error bars, is still considerable, though. When the electron spectrum is calculated, these errors induce considerable uncertainty giving rise to a spectrum that fluctuates from one energy bin to the next. Within the uncertainties a monotonic spectrum can still be fit, though. But the electron deconvolution technique is not really feasible for the low spectral resolution and low signal-to-noise ratios.

To get a more useful result the observational X-ray data has been fit to a power law, which gives a much more well-behaved deconvoluted electron spectrum, but the uncertainty is equally large of course.

Figure 4.6 presents data from 12 March 1998, 03:30:30–03:35:00 UT at Kangerlussuaq. The X-ray flux data versus energy is plotted with X symbols in a double logarithmic plot. Error bars are one standard deviation. The best power law fit to the data is shown by a dashed line. In the upper part of the plot the deconvoluted electron fluxes are shown with diamonds. The best fitting power law spectrum is indicated with a dashed line to provide an extrapolation for better comparison with the electron spectrum derived from the same observational data by the method of Østgaard et al. (2000) and shown by a solid line. In Fig. 4.7, which is a semi-logarithmic plot provided by Nikolai Østgaard, are shown the ob-

served X-ray data and the X-ray spectrum predicted from the electron spectrum shown by the solid line in Fig. 4.6. The electron spectrum was found by a least-squares fitting method, going through a database of model calculations. In this case a single exponential spectrum gave a better fit than a sum of two exponentials. Comparing the observed X-ray energy spectra displayed in double and semi logarithmic plots it is inconclusive whether an exponential or a power law fit to the X-ray data is most appropriate.

The following three pairs of figures use the same layout. Figure 4.8 presents data from 12 March 1998, 03:40:40–03:45:00 UT. From the approximately five minutes between this and the previous spectrum, no data was available from the PIXIE front chamber due to the duty cycling of the high-voltage power supply. In Fig. 4.9 are the X-rays predicted by the electron spectrum obtained by the method of Østgaard et al. (2000). Figures 4.10 and 4.11 similarly present data from a few days later, 15 March 1998, 02:00:40–02:04:40 UT at the same site, while Figs. 4.12 and 4.13 show data from 15 March 1998, 02:10:40–02:14:40 UT. Again the gap between the two time intervals are due to power cycling of the front chamber.

The general impression from these figures is that the derived electron energy fluxes from the two methods agree well. The best agreement is seen when the Østgaard method gives the electron energy flux as a sum of two exponentials. In the case of a single exponential spectrum the two methods diverge quickly outside the energy interval of measured X-rays.

The Østgaard method was validated by Østgaard et al. (2000) who compared derived double exponential spectra to in situ electron measurements from DMSP and NOAA satellites, validating the usefulness of the estimates. The demonstrated likeness of electron energy fluxes derived with the method of Østgaard and the method of this work leads to the conclusion that the electron spectra derived here are indeed valid and useful estimates of the actual precipitating electron fluxes.

4.5.1 Comparison with riometer data

Spectra were derived in a spatially limited region over the station of Kangerlussuaq to enable further validation of the data by comparison with imaging riometer data. The circular ionospheric area for which X-ray energy fluxes were obtained was defined as the cross section at 100 km altitude of the opening of a cone of zenith angle 75° originating at the station coordinates. In the plane parallel approximation this gives a circle of radius 370 km, but for such large zenith angles

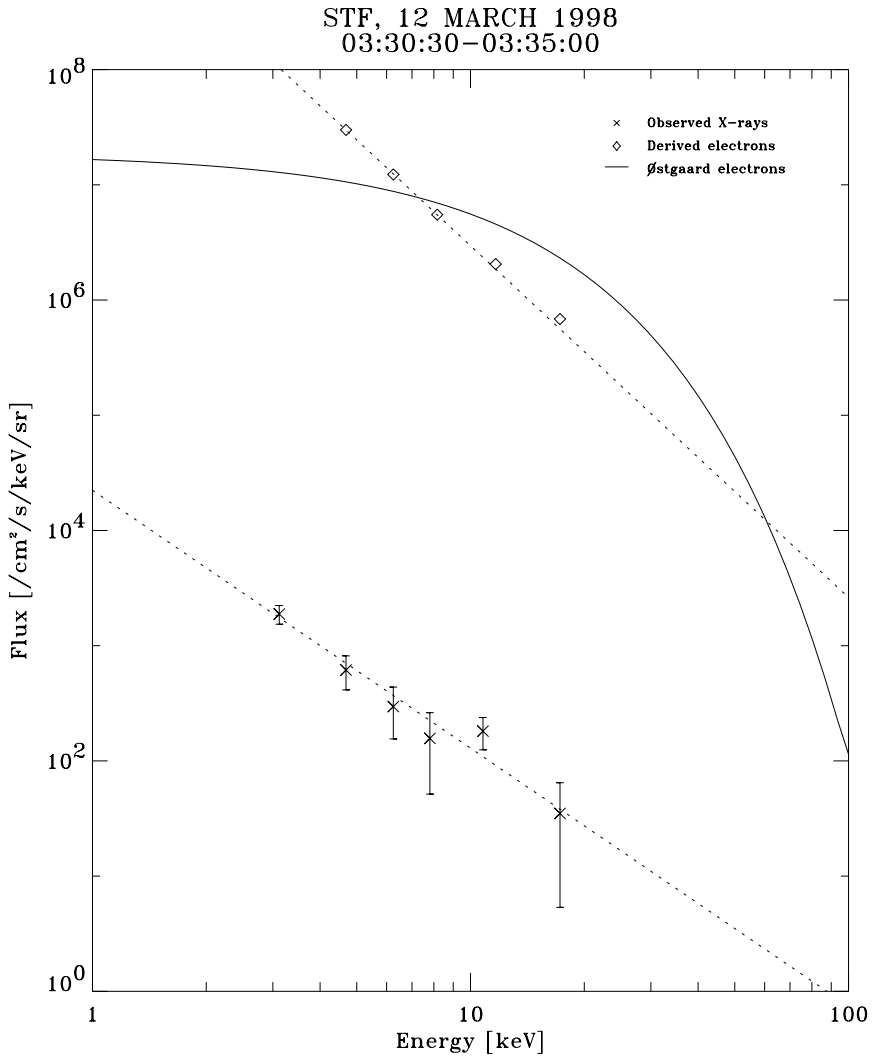

Figure 4.6: **Observed X-rays and deconvoluted electrons, 12 March 1998, 03:30:30–03:35:00 UT at Kangerlussuaq. X**: Observed X-ray fluxes with 1 σ error bars. $\diamond$**:** Deconvoluted electron fluxes. **Dashed lines** are power law fits to the spectra. **Solid line:** electron spectrum derived by the method of Østgaard et al. (2000). All fluxes are in units of [#/cm^2/keV/s/sr]. Both axes are logarithmic.

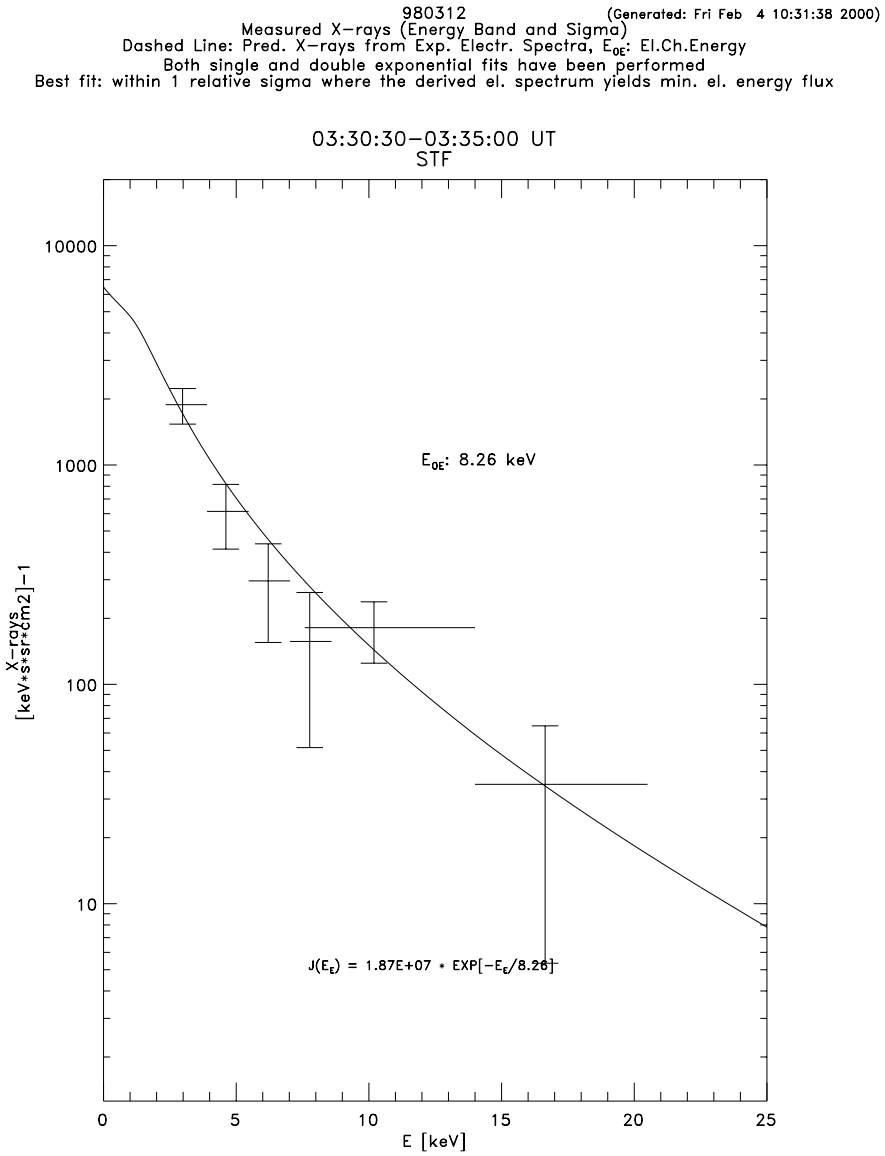

Figure 4.7: **Observed and predicted X-rays, 12 March 1998, 03:30:30–03:35:00 UT at Kangerlussuaq.** Widths of the energy bins are indicated by the horizontal lines of the symbols, whereas the vertical lines are 1 σ error bars. The solid line shows the predicted X-ray spectrum from the best fi tting electron spectrum found from a pre-calculated database by a least squares fi tting method. The characteristic energy of the exponential electron spectrum and the energy spectrum in units of [electrons/cm^2/keV/s/sr] is indicated. Semi-logarithmic plot. (Courtesy of Nikolai Østgaard).

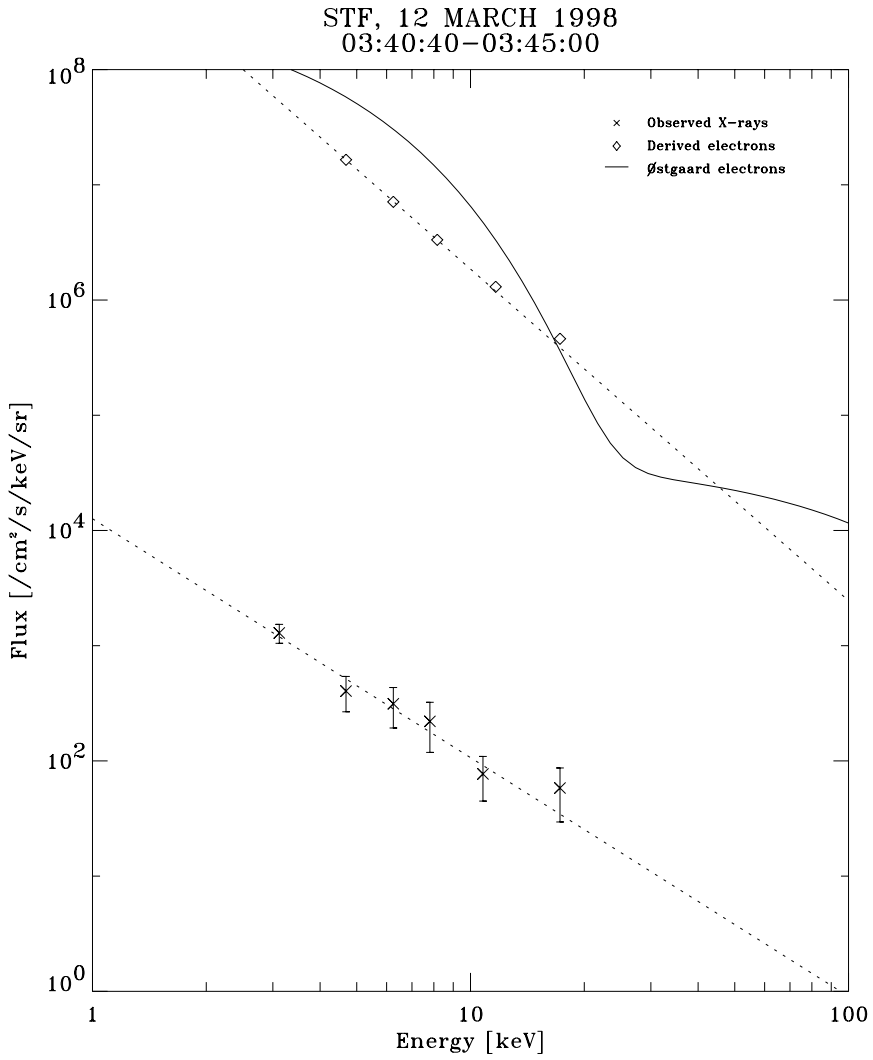

Figure 4.8: **Observed X-rays and deconvoluted electrons, 12 March 1998, 03:40:40–03:45:00 UT at Kangerlussuaq. X**: Observed X-ray fluxes with 1 σ error bars. $\diamond$**:** Deconvoluted electron fluxes. **Dashed lines** are power law fits to the spectra. **Solid line:** electron spectrum derived by the method of Østgaard et al. (2000). All fluxes are in units of [#/cm^2/keV/s/sr]. Both axes are logarithmic.

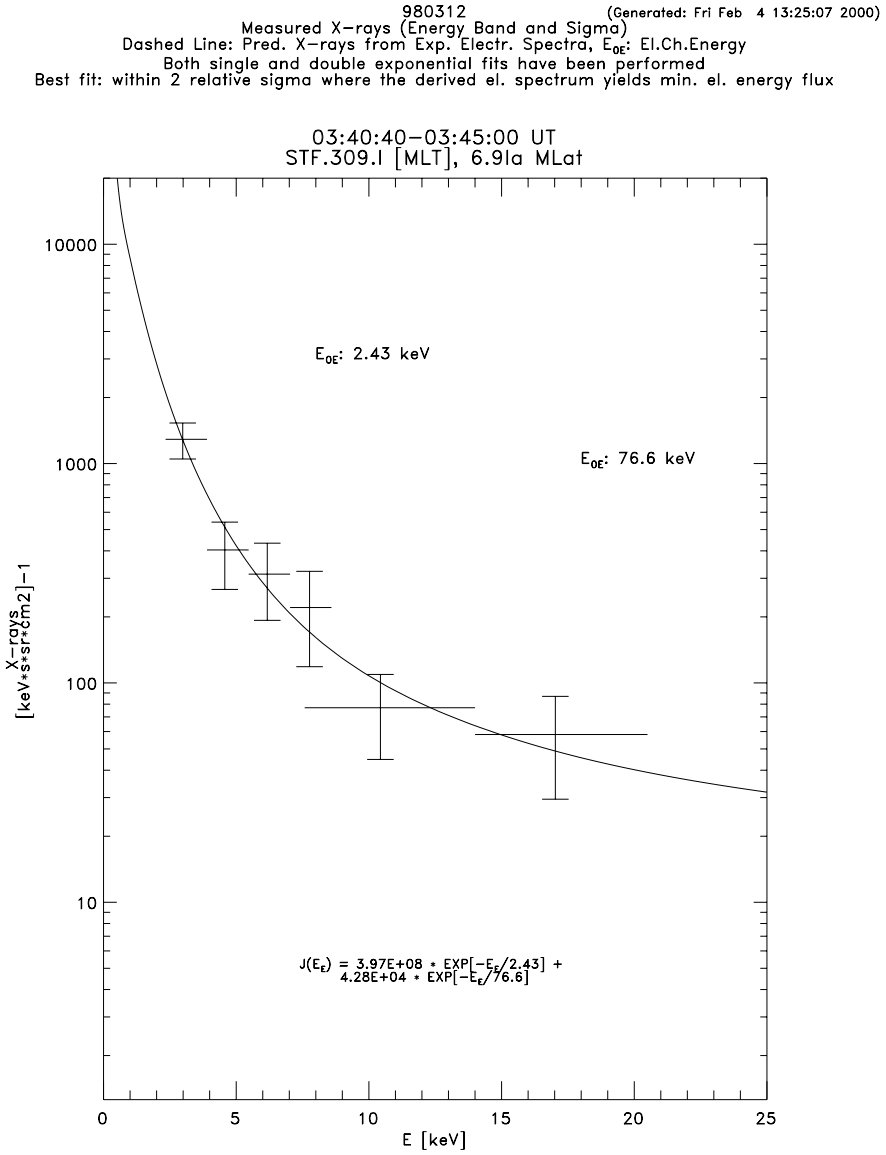

Figure 4.9: **Observed and predicted X-rays, 12 March 1998, 03:40:40–03:45:00 UT at Kangerlussuaq.** Widths of the energy bins are indicated by the horizontal lines of the symbols, whereas the vertical lines are 1 σ error bars. The solid line shows the predicted X-ray spectrum from the best fi tting electron spectrum found from a pre-calculated database by a least squares fi tting method. The characteristic energies of the two components of the double exponential electron spectrum and the expression for the electron energy spectrum in units of [electrons/cm^2/keV/s/sr] is given. Semi-logarithmic plot. (Courtesy of Nikolai Østgaard).

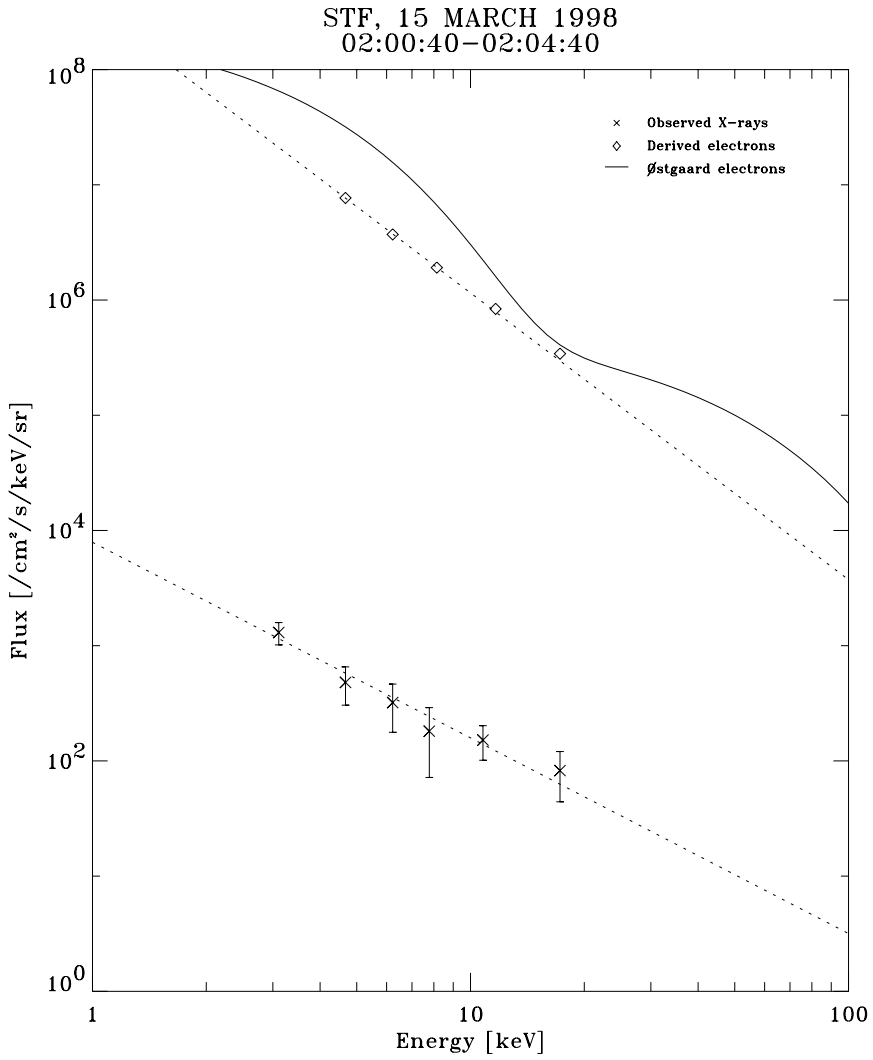

Figure 4.10: **Observed X-rays and deconvoluted electrons, 15 March 1998, 02:00:40–02:04:40 UT at Kangerlussuaq. X**: Observed X-ray fluxes with 1 σ error bars. $\diamond$**:** Deconvoluted electron fluxes. **Dashed lines** are power law fits to the spectra. **Solid line:** electron spectrum derived by the method of Østgaard et al. (2000). All fluxes are in units of [#/cm^2/keV/s/sr]. Both axes are logarithmic.

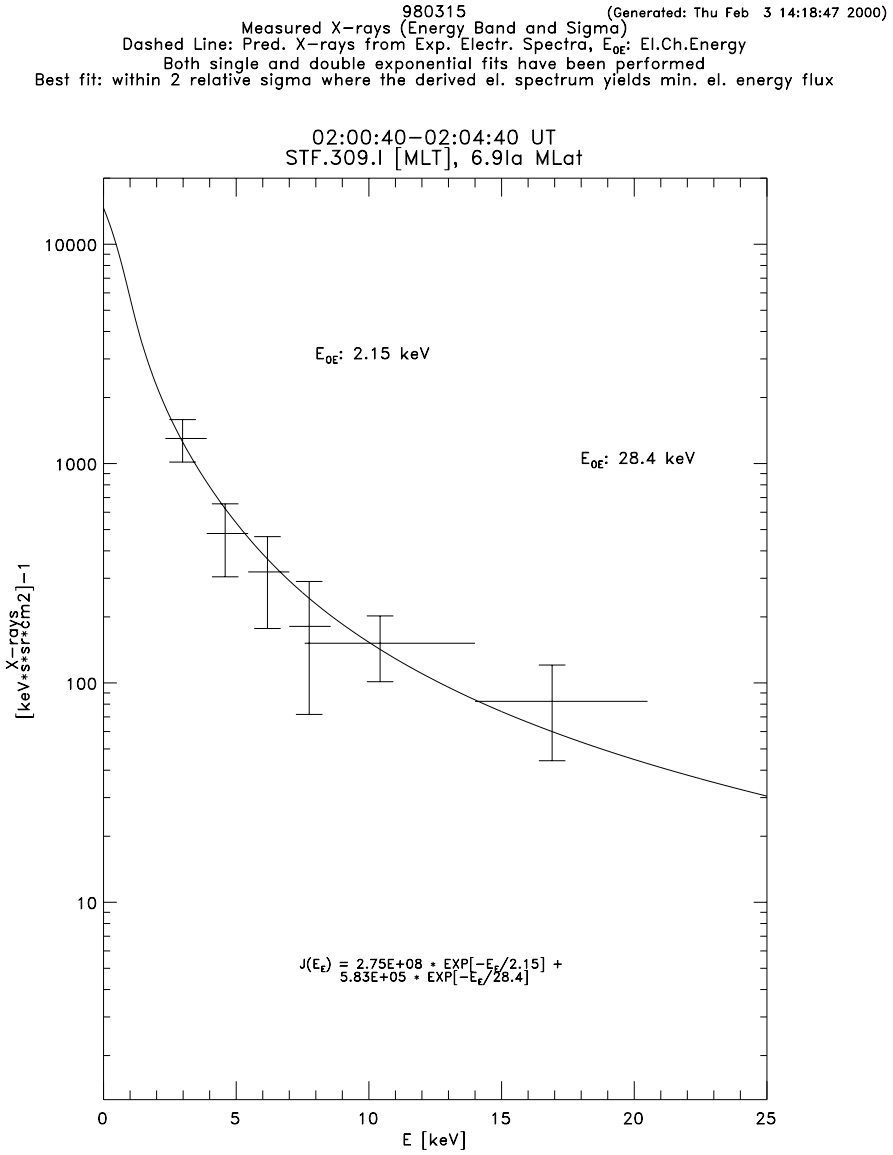

Figure 4.11: **Observed and predicted X-rays, 15 March 1998, 02:00:40–02:04:40 UT at Kangerlussuaq.** Widths of the energy bins are indicated by the horizontal lines of the symbols, whereas the vertical lines are 1 σ error bars. The solid line shows the predicted X-ray spectrum from the best fitting electron spectrum found from a pre-calculated database by a least squares fitting method. The characteristic energies of the two components of the double exponential electron spectrum and the expression for the electron energy spectrum in units of [electrons/cm^2/keV/s/sr] is given. Semi-logarithmic plot. (Courtesy of Nikolai Østgaard).

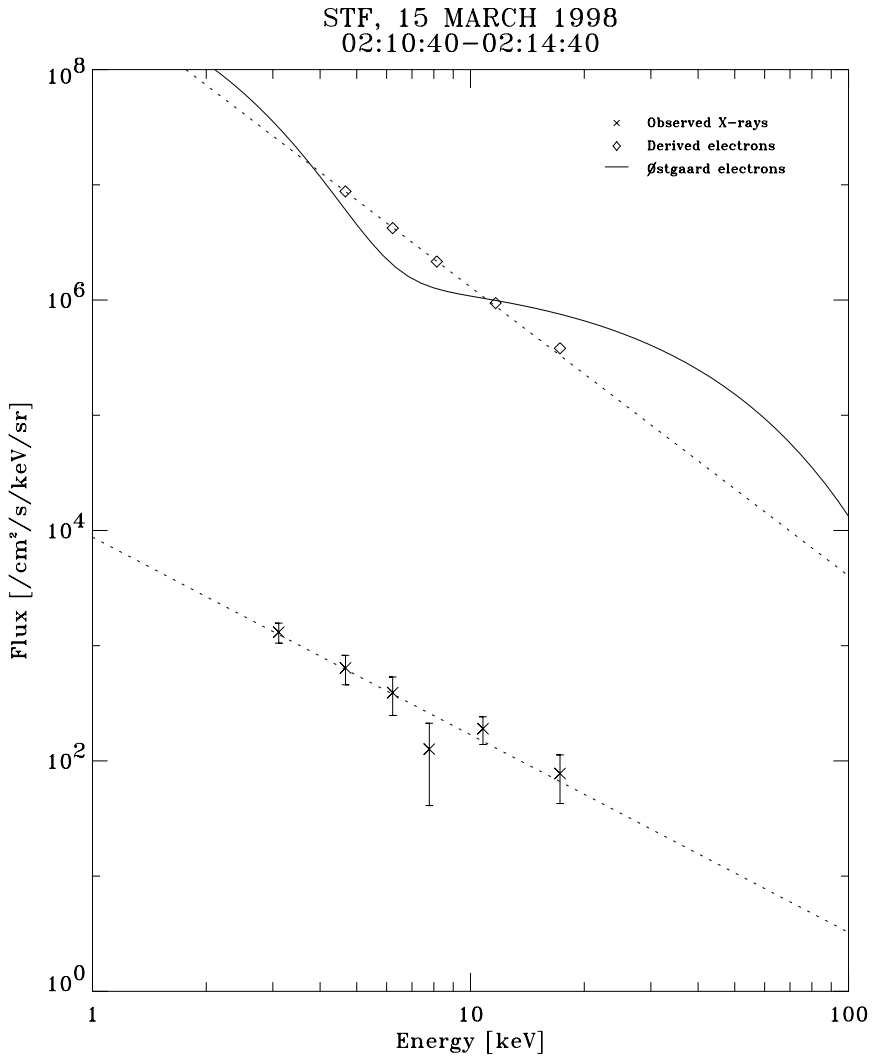

Figure 4.12: **Observed X-rays and deconvoluted electrons, 15 March 1998, 02:10:40–02:14:40 UT at Kangerlussuaq. X**: Observed X-ray fluxes with 1 σ error bars. $\diamond$**:** Deconvoluted electron fluxes. **Dashed lines** are power law fits to the spectra. **Solid line:** electron spectrum derived by the method of Østgaard et al. (2000). All fluxes are in units of [#/cm^2/keV/s/sr]. Both axes are logarithmic.

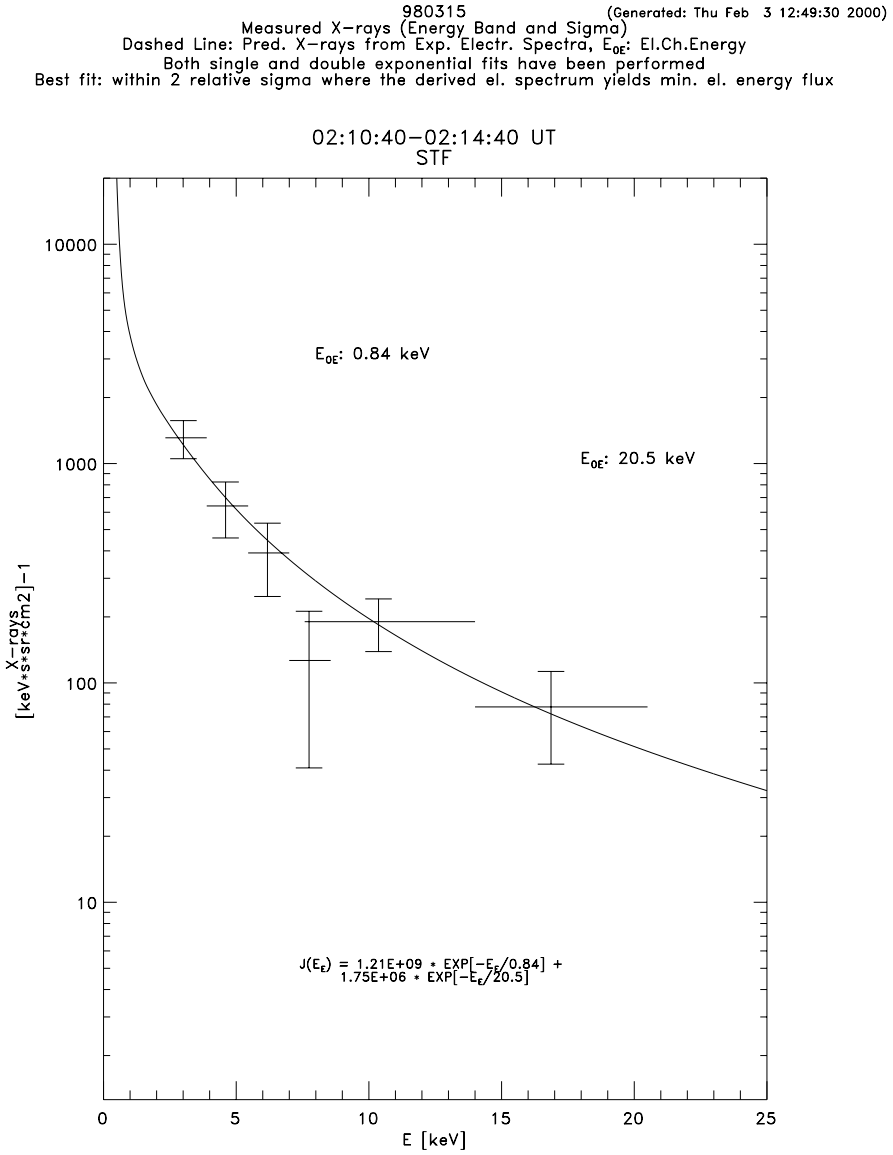

Figure 4.13: **Observed and predicted X-rays, 15 March 1998, 02:10:40–02:14:40 UT at Kangerlussuaq.** Widths of the energy bins are indicated by the horizontal lines of the symbols, whereas the vertical lines are 1 σ error bars. The solid line shows the predicted X-ray spectrum from the best fitting electron spectrum found from a pre-calculated database by a least squares fitting method. The characteristic energies of the two components of the double exponential electron spectrum and the expression for the electron energy spectrum in units of [electrons/cm^2/keV/s/sr] is given. Semi-logarithmic plot. (Courtesy of Nikolai Østgaard).

the curvature of the ionosphere must be taken into account. Let z denote the zenith angle and $s(z)$ denote the oblique path length from the ground to the ionospheric altitude h. The horizontal distance, $d(z)$, in the curved ionosphere is then given by (Detrick & Rosenberg 1990, their Eq. (4)):

$$d(z) = (R_E + h) \arccos\left(\frac{(R_E + h)^2 + R_E^2 - s^2(z)}{2R_E(R_E + h)}\right), \tag{4.18}$$

$$\text{where} \qquad s(z) = \sqrt{(R_E + h)^2 - R_E^2 \sin^2 z} - R_E \cos z.$$

In this case R_E should be taken as the polar radius of the Earth. Figure 4.14

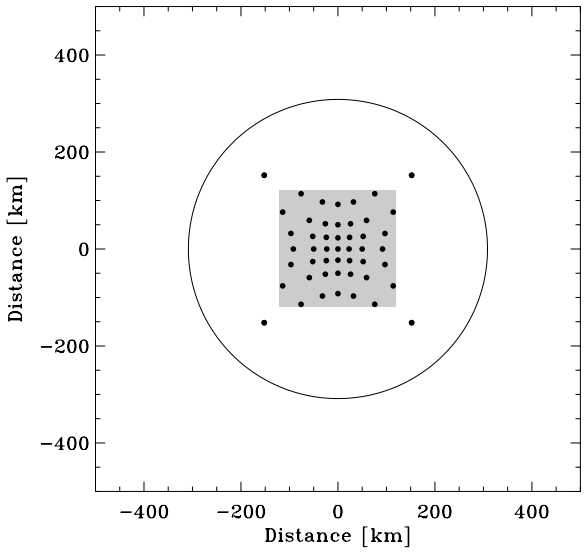

Figure 4.14: **Circle of derived PIXIE flux and field-of-view of imaging riometer.** In the plot is shown horizontal distances in a curved ionosphere at 90 km altitude. The circle is the area for which PIXIE spectra were obtained. For the riometer only the 49 points of maximum sensitivity is shown, but the actual fi eld-of-view is larger, cf. Fig. 3.1. The grey area indicates a fi eld-of-view of 240 by 240 km.

shows the area for which PIXIE fluxes were derived as projected onto the curved ionosphere at 90 km altitude. For comparison the riometer field-of-view is also indicated.

Time series of X-ray fluxes from the PIXIE rear chamber with one minute time resolution are compared with absorption measurements from the imaging riometer (shown with 10 s time resolution) for the two days in March 1998 in Figs. 4.15

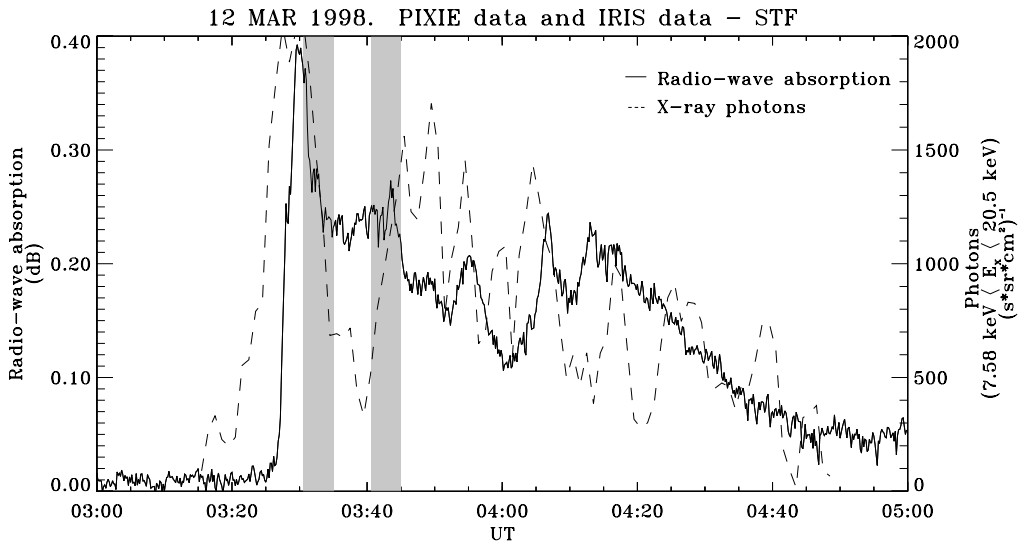

Figure 4.15: **Absorption and X-ray flux over Kangerlussuaq, 12 March 1998. Dashed line:** Integrated X-ray flux from the PIXIE rear chamber in the energy interval 7.58–20.5 keV with one minute time resolution. **Solid line:** Absorption averaged over all 49 beams of the imaging riometer with 10 s time resolution. The two time intervals for which spectra were derived are indicated in grey.

and 4.16. Due to the difference in spatial resolution of the two instruments, the absorption data were averaged over all 49 beams. Making a simple average was considered the best basis for comparison with the much larger field-of-view of PIXIE.

The absorption registered in a riometer beam depends on the spatial extent of the absorbing region as was pointed out by Nielsen & Axford (1977). If the absorption region covers the beam only partly, the absorption will be underestimated. For the narrow beams of an imaging riometer the problem is probably insignificant for the central, zenith pointing beams as the calculation of Hargreaves et al. (1979) suggests. However, the perimeter beams have a considerable zenith angle and the sensitive cross sectional beam area is significant (see Fig. 3.1). These beams might underestimate the absorption if the absorbing region exhibits small-scale structure. But since here it is not the absorption of the small-scale feature that is of consequence for the comparison with PIXIE data, but rather the large-scale average, no correction term (apart from path length correction due to the zenith angle) have been applied to any beams. Such a correction would in any case be a precarious affair as the small-scale morphology of the absorption re-

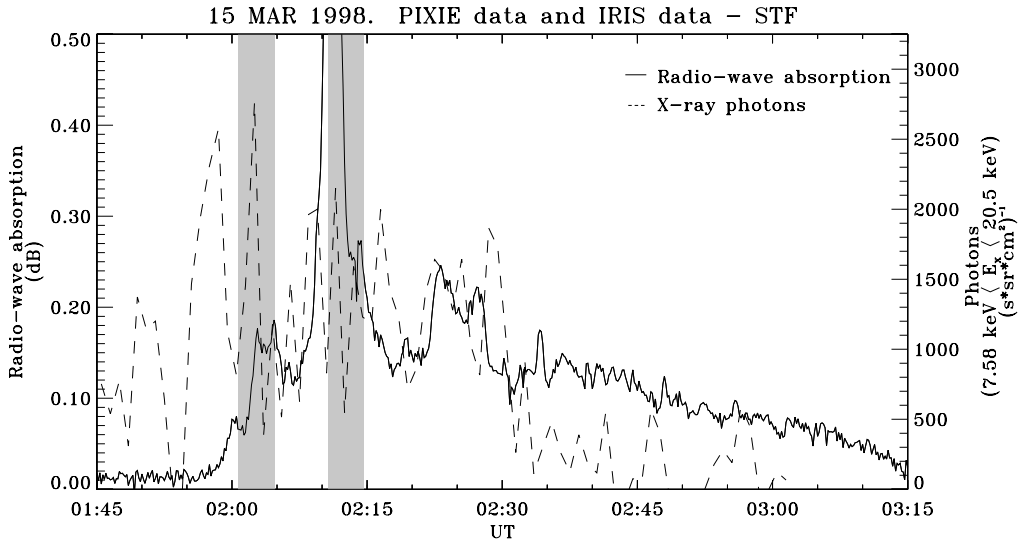

Figure 4.16: **Absorption and X-ray flux over Kangerlussuaq, 15 March 1998. Dashed line:** Integrated X-ray flux from the PIXIE rear chamber in the energy interval 7.58–20.5 keV with one minute time resolution. **Solid line:** Absorption averaged over all 49 beams of the imaging riometer with 10 s time resolution. The two time intervals for which spectra were derived are indicated in grey.

gions seen by the edge beams is unknown. In cases where the absorbing region has arc structure, a spatial form, e.g. a Gaussian strip with limited latitudinal extent but widely stretched in longitude is a reasonable assumption, and corrections could be applied.

From the derived electron spectra the expected riometer absorption can be calculated. The results are presented in Table 4.2. The values for expected riometer absorption were obtained by model calculations performed by Arve Aksnes at the University of Bergen, Norway, using a model[3] (Aksnes et al. 2002) developed by Dan Detrick at the University of Maryland, College Park, and based on a model which was written and validated by Rich Vondrak and co-workers (Vondrak & Baron 1976; Vondrak & Sears 1978; Vondrak & Robinson 1985). This model was

[3]The model is described in detail in an unpublished document (Detrick 1997). (The model, which has been refi ned and modifi ed over time, in want of a proper name is referred to as Mangle: a name derived from the names of Rich Vondrak's models Tangle and Untangle for calculating the atmospheric effects of precipitating electrons and deriving electron spectra, respectively. In preparation of a proposal for riometry on Mars the code was modifi ed by Dan Detrick to handle calculations also for Martian conditions and thus acquired the initial M.)

Table 4.2: Derived and measured absorption

Date	Time [UT]	Absorption derived[a]		Absorption
		Power law[b]	Exponential[b]	Measured
12 March 1998	03:30:30–03:35:00	0.34 dB	0.39 dB	0.27 dB
12 March 1998	03:40:40–03:45:00	0.30 dB	0.44 dB	0.24 dB
15 March 1998	02:00:40–02:04:40	0.32 dB	0.66 dB	0.13 dB
15 March 1998	02:10:40–02:14:40	0.33 dB	0.72 dB	0.48 dB

[a] From model calculations courtesy of Arve Aksnes.

[b] Shape of incident electron spectrum.

in turn based on work by Rees (1963) and Berger et al. (1970; 1972). From an incident electron spectrum it calculates energy deposition and different atmospheric effects. For the present work the interesting output is the calculated instrumental responses for riometers and photometers for specific input electron spectra.

A result of the model calculations is that the height of maximum absorption for the studied time intervals is 85–91 km in accordance with the assumed reference height of 90 km for the imaging riometer.

The absorption values presented in Table 4.2 were calculated for the energy interval 0.1–100 keV. In this interval the spectra, which are a sum of two exponentials, have slightly higher fluxes than the power law spectra which explains the higher absorption values. For the first entry the exponential spectrum did not have a high-energy tail, and the two calculated absorption values are very close. For 12 March 1998 the absorption calculated from the power law spectra fit nicely with the measured absorption in the time intervals. For the 15 March 1998 the value is overestimated for the first time interval and underestimated for the second. It is evident from Fig. 4.16 that the energetic electron event as observed by PIXIE has an earlier onset than detected by the riometer, and the explanation for the discrepancies most likely has to do with the different fields-of-view for the two instruments. This can be investigated by looking at the morphology of the events.

Riometer data can be represented in different ways emphasizing different features. Time series of two-dimensional absorption images like Figs. 4.17 and 4.18 are very useful for obtaining information on morphology, movement and many other features with good temporal and spatial resolution. For studying these pa-

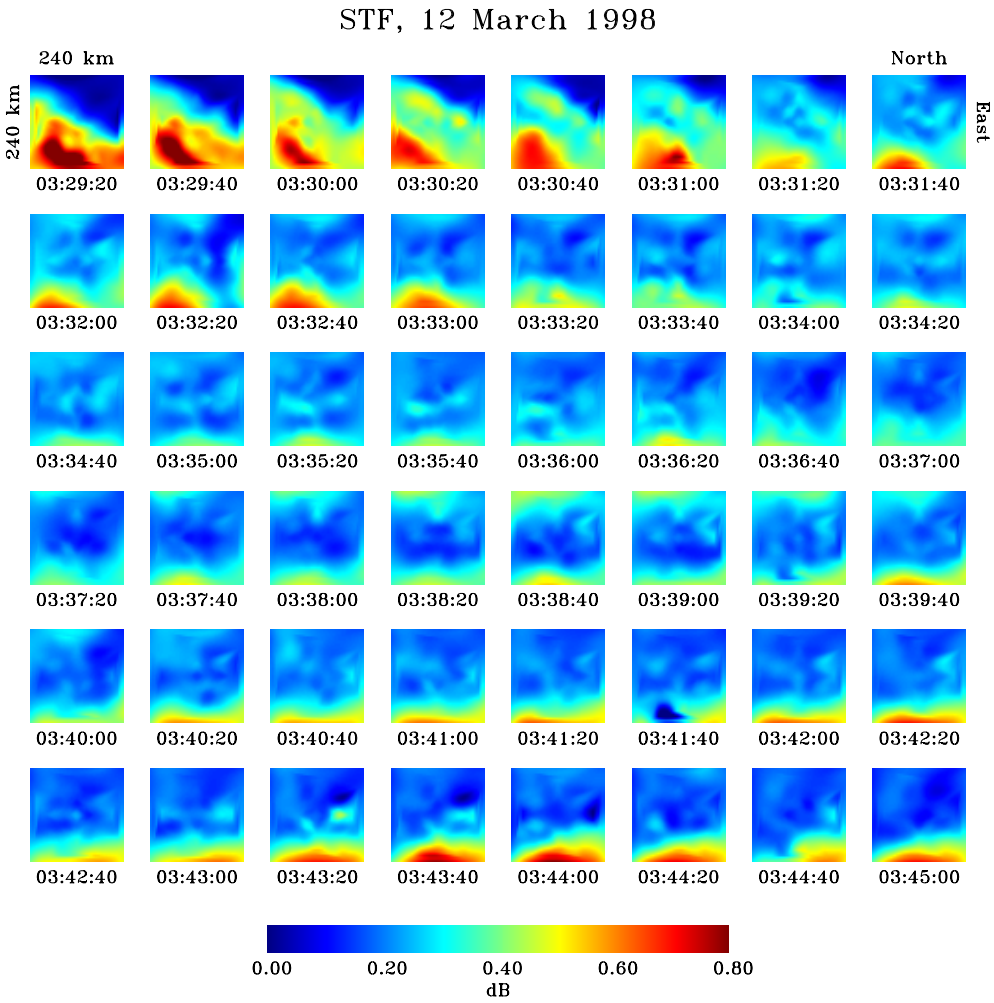

Figure 4.17: **Time series of absorption images from Kangerlussuaq, 12 March 1998.** Each image covers 240 by 240 km. Geomagnetic north is up, east is right. The colour bar gives the absorption intensity. UT time stamps are given below each image.

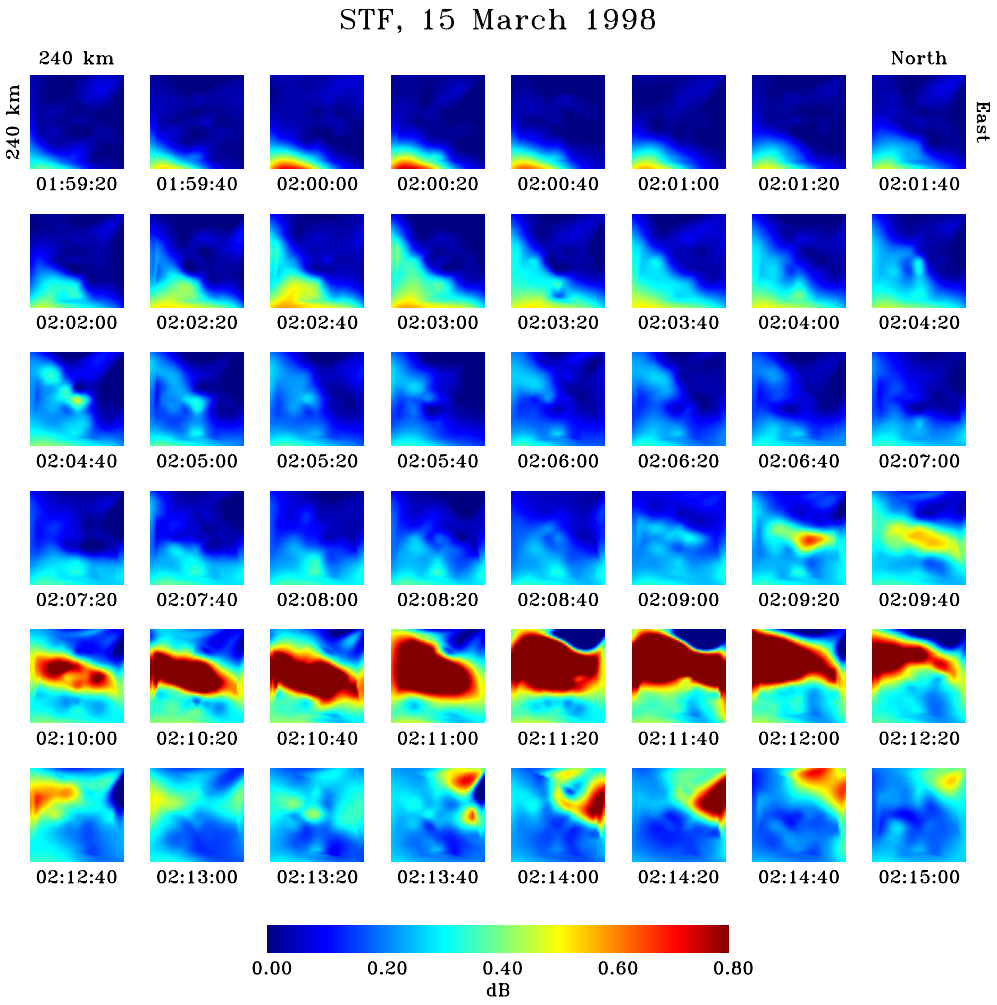

Figure 4.18: **Time series of absorption images from Kangerlussuaq, 15 March 1998.** Each image covers 240 by 240 km. Geomagnetic north is up, east is right. The colour bar gives the absorption intensity. UT time stamps are given below each image.

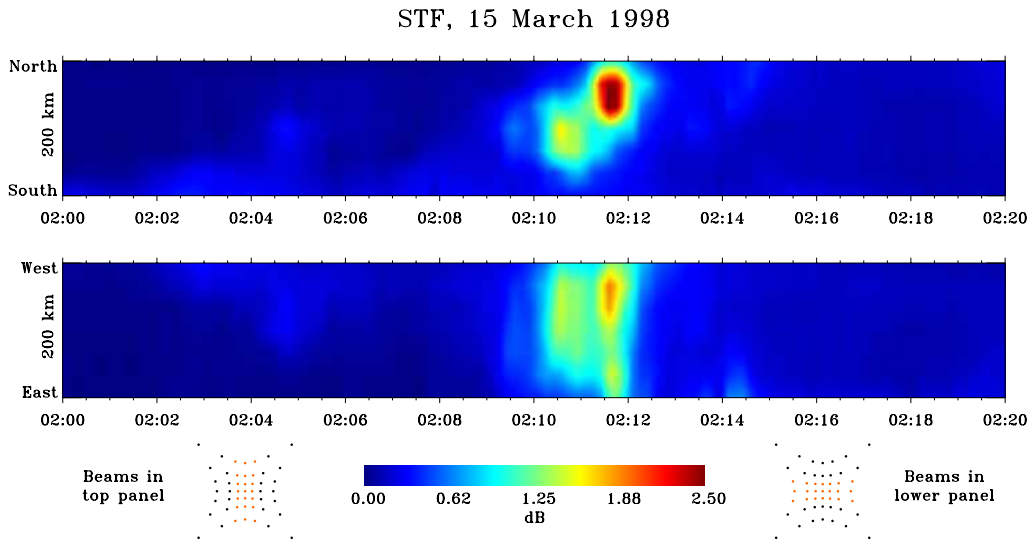

Figure 4.19: **Absorption keogram from Kangerlussuaq, 15 March 1998.** The keogram has time along the x axis and one spatial dimension along the y axis while the colour bar gives the absorption intensity. In the upper panel the three central north-south rows of beams (indicated in the lower left of the legend) are averaged into one north-south row of beams. A time series is created by making a sideways stacked plot of the one-dimensionally collapsed data. Likewise for the lower panel where the east-west spatial information is obtained from the three central east-west rows of beams (indicated in the lower right of the legend).

rameters over longer periods of time, e.g. throughout a whole substorm, the data is more conveniently shown in the keogram format (described below) which is particularly good for tracking movements and intensifications. For these plot types setting the upper and lower limits of the colour scale is very important for emphasizing different features in the same images, as is always the case when representing data as colour images.

Absorption images as those in Figs. 4.17 and 4.18 are obtained by two-dimensional interpolation and extrapolation of the irregular grid of 7×7 pixels (where the absorption measurements of each beam is ascribed to the point of maximum sensitivity rather than to an area). Adjustable parameters are the projection height and the extent of the resulting regular grid (the field-of-view of the image). If extrapolation is unwanted the resulting grid should not exceed the dimensions

200 by 200 km for an altitude of 90 km. In Fig. 4.14 the 240 by 240 km field-of-view at 90 km used here is shown together with the original irregular grid.

The keogram (see Fig. 4.19) has time along the x axis and one spatial dimension along the y axis while the colour code gives the absorption. In its simplest form the keogram is made up as a sideways stacked plot of a single row of beams, such as the central row of north-south beams. This plot type is very convenient for detecting poleward or equatorward motion of features. Using just one beam row gives a very limited spatial sampling in the east-west direction, though, and it is often appropriate to combine the three central rows for each time step, such as in Fig. 4.19: In the upper panel the three central north-south rows of beams are averaged into one north-south row of beams. A time series is created by making a sideways stacked plot of the one-dimensionally collapsed data. Likewise for the lower panel where the east-west spatial information is obtained from the three central east-west rows of beams.

For 12 March 1998 we see in the images of Fig. 4.17 that even if the southern beams much of the time observe stronger absorption, there is a still a significant level of absorption over the full field-of-view during the two time intervals of interest.

For 15 March 1998 the absorbing region in the first time interval covers half or less than half of the field-of-view. Absorption is first seen in the southern beams and then propagates northward and eastward. It is conceivable that energetic electron precipitation is taking place mainly equatorward of the riometer, but within the field-of-view of PIXIE, giving rise to the observed difference in onset times. During the second time interval the sudden and intense increase in absorption in an approximately east-west oriented arc dominates the riometer data. The arc is of limited latitudinal extent, and the most intense absorption (exceeding 3 dB) occurred localized within the poleward moving arc, see the keogram in Fig 4.19. This means that in the larger field-of-view of PIXIE this localized energetic electron event will contribute relatively less.

To test the idea that the PIXIE data is dominated by activity in the southern part of the field-of-view, especially during the first time interval, the PIXIE time series data of 15 March 1998 is plotted in Fig. 4.20 together with data from a single riometer beam: the central one in the southern-most row which is typical for the two southern-most rows. Better agreement is indeed seen, and the absorption values for this single beam in the two time intervals are 0.31 and 0.28 dB, respectively, in accordance with the calculated absorption values presented in Table 4.2.

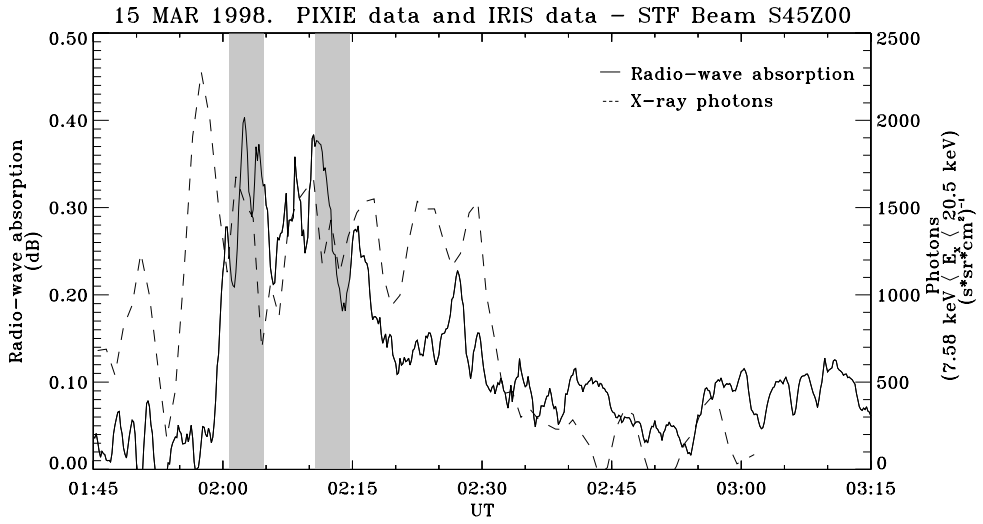

Figure 4.20: **Absorption and X-ray flux over Kangerlussuaq, 15 March 1998. Dashed line:** Integrated X-ray flux from the PIXIE rear chamber in the energy interval 7.58–20.5 keV. **Solid line:** Absorption for a single beam of the imaging riometer: the central beam in the most equatorward row. The two time intervals for which spectra were derived are indicated in grey.

4.6 Conclusion

The scheme for deconvolution of electron energy spectra from X-ray measurements presented in this chapter could in the future become a valuable tool for global characterization of precipitating electrons which carry vital information about magnetospheric processes and enable testing of storm and substorm theories.

Modern solid state X-ray detectors with high energy resolution properties, such as the CdZnTe X-ray imager (Budtz-Jorgensen et al. 2001) originally designed for the Atmospheric X-ray Observatory which was proposed to the Danish Small Satellite Programme by Torsten Neubert, would constitute an excellent and very affordable means of monitoring high-energy electron precipitation with all the advantages of X-rays measurements such as the immunity to contamination from sunlight, airglow and precipitating ions.

Chapter 5

Conjugate event study

Given the ground-based resources of the two institutions where my research was carried out, Solar-Terrestrial Physics Division of the Danish Meteorological Institute and Institute for Physical Science and Technology of the University of Maryland, College Park, finding X-rays events occurring over imaging riometer and magnetometer stations in Greenland or Antarctica was emphasized. Perigee passes last about 30 minutes of each 18 hour orbit and the high spatial and temporal resolution possible makes comparisons with ground-based data favourable. Unfortunately none of the perigee passes through the first 32 months of the mission while the rear chamber was functional where promising for a correlated study of X-ray and ground-based activity.

Instead an unusually intense high-energy precipitation event occurring on 6 August 1998 at high-latitude was chosen for study. The event was intriguing because PIXIE observed a localized high-intensity burst of X-rays while the geomagnetically conjugate imaging riometers in Iqaluit and South Pole both detected very strong absorption events (Christensen et al. 2003). This chapter is dedicated to the analysis of this event which was most likely a consequence of a burst of reconnection in the magnetotail initiating an earthward plasma flow which might have experienced a further energization of electrons in the encounter of an acceleration mechanism above the ionosphere. Such events provide valuable information about magnetospheric source regions and physical processes which can impose constraints on substorm theories and the nature of magnetosphere-ionosphere coupling.

5.1 Geomagnetic conjugacy

Locations connected by the same magnetic field line are geomagnetically conjugate. Stations at such sites are expected to record similar events during globally disturbed conditions like substorms, as they are connected to the same magnetospheric source regions. But the geomagnetic field is highly variable on a daily and seasonal basis in addition to the effect of storm and substorm disturbances. So two stations designed and located to be conjugate will not be so all the time. The higher the magnetic latitude, the fewer are the daily hours of conjugacy. When the stations are on open field lines they can still record events that are very alike if they connect through field lines to the same magnetospheric source region.

Determining the conjugacy of stations is dependent on the accuracy of the geomagnetic model used and its capability to realistically handle disturbed conditions. Apart from concerns about the exactness of the conjugacy, hemispherical asymmetry arises from ionospheric conductivity differences (Newell et al. 1996).

Conjugacy surveys of auroral zone stations have been conducted by many authors. E.g. Hajkowicz (1990) conducted a study of 161 sudden increases of riometer absorption from three years of data, and Wu et al. (1991) studied 60 events of substorm-related overhead passes of a westward electrojet from one year of magnetometer data from the high-latitude conjugate stations South Pole and Iqaluit.

Electron microburst groups which are of small scale size and demand subsecond time resolution have been observed conjugately by a balloon-borne X-ray detector in the northern hemisphere and the riometer at Siple Station, Antarctica (Rosenberg et al. 1980; Siren et al. 1980).

Stenbaek-Nielsen & Otto (1997) presented a re-analysis of previously published conjugacy studies based on auroral all-sky images from conjugate aircraft flights between 1967 and 1971. The authors argued that while diffuse aurora is conjugate, discrete aurora might well be non-conjugate. If discrete aurora is related to the field-aligned current in the acceleration region in the near-Earth magnetosphere, observed hemispherical differences can be explained by an inter-hemispherical field-aligned current component created by the penetration of the IMF B_y component into the magnetosphere. The direction of the inter-hemispherical current will depend on the IMF B_y orientation. For B_y negative brighter aurora at higher latitude would be expected for the northern hemisphere, and vice versa for negative B_y, in qualitative agreement with the observations reported by the authors, even if the statistics are very limited.

Inter-hemispherical asymmetries reported by Vorobjev et al. (2001) based

on 10 events show the opposite dependence on IMF B_y, but these authors also stressed the importance of the IMF B_x component, not investigated by Stenbaek-Nielsen & Otto (1997).

5.2 Overview of the event of 6 August 1998

The subject under investigation here is a very intense event of energetic electron precipitation at high geomagnetic latitude, about 74°. Magnetic latitudes are given in CGM coordinates[1] throughout. The event took place on 6 August 1998 in the dusk sector at 2259 UT and lasted about 10 minutes. It occurred at the poleward edge of the poleward expanding bulge or westward travelling surge of an ongoing substorm.

A geomagnetic storm was initiated by a sudden impulse at 0736 UT on 6 August 1998. At noon the final hourly D_{st} index, see Fig. 5.1, reached a minimum of -138 nT, and at 23 UT it had recovered to -93 nT. Over the six days displayed a

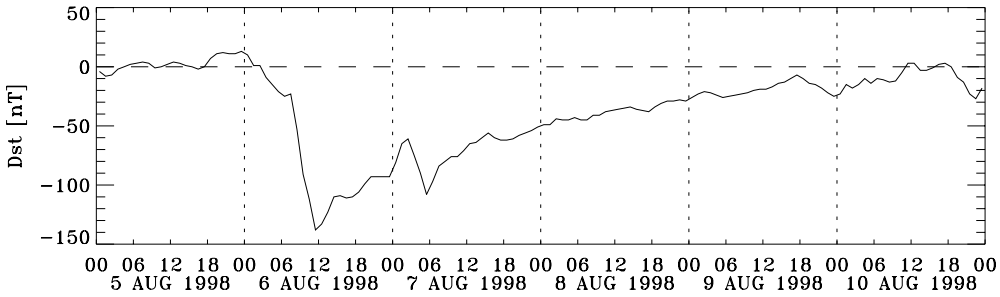

Figure 5.1: **D_{st} on 5–10 August 1998.** The development of the D_{st} index during the geomagnetic storm initiated by a sudden impulse at 0736 UT on 6 August 1998. Time is UT. Final hourly values of the D_{st} index were provided by World Data Center C2 for Geomagnetism, Kyoto University, Japan.

classic D_{st} development of a geomagnetic storm is seen with an initial compression phase of positive D_{st} excursion, followed by the storm main phase during which D_{st} decreased as the ring current was built up and finally the long recovery phase where ring current particles were slowly lost while D_{st} gradually increased toward zero.

Solar wind data from the WIND satellite are displayed in Fig. 5.2. The data

[1] See Appendix A.

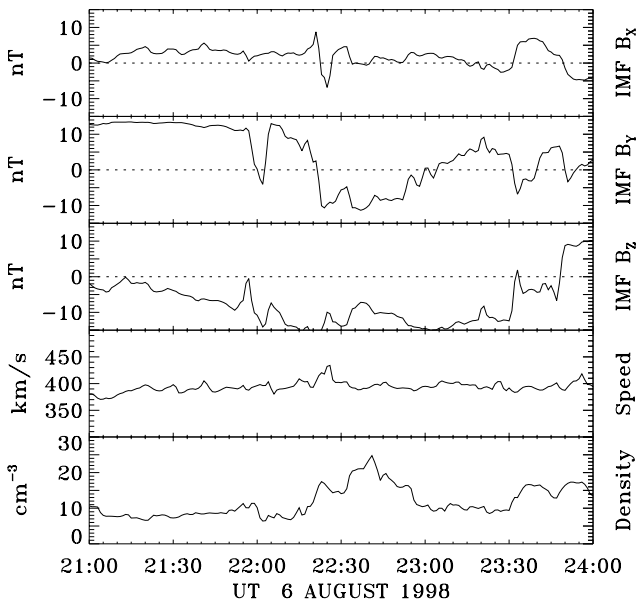

Figure 5.2: **Solar wind data 21–24 UT, 6 August 1998.** From the WIND spacecraft located at (91, 11, -3 R_E GSE). Ballistic propagation of the data to 12 R_E distance was applied, giving a time lag of 22 minutes. **Panel 1–3:** X, Y and Z GSM components of the interplanetary magnetic field. **Panel 4:** Solar wind bulk speed. **Panel 5:** Solar wind ion density. WIND data were obtained from CDAWeb and provided by R. Lepping at NASA/GSFC (Magnetic Field Investigation) and R. Lin at UC Berkeley (3D Plasma Analyzer).

has been shifted to a position 12 R_E in front of the Earth (the approximate magnetopause distance). The ballistic propagation resulted in a 22 minute time lag of the data measured by the WIND spacecraft located at (91, 11, -3 R_E GSE). Thus situated upstream of the Earth the satellite was in a good position for monitoring solar wind changes that could have an impact on the magnetosphere.

After more than eleven hours of strongly southward IMF, the field turned northward at 1300 UT and the geomagnetic activity level became quiet while the IMF stayed northward or close to zero. After 2115 UT the IMF became persistently southward and a period of strongly negative B_z followed. Such prolonged periods of southward IMF will cause a high rate of dayside magnetic reconnec-

tion resulting in a large amount of magnetic flux being transported to the nightside where it will give rise to a highly unstable magnetotail configuration. Such a situation is very likely to result in an unloading of the energy in one or more substorms.

Prior to the substorm during which the event to be studied occurred, an auroral brightening was observed. Images from Polar/UVI showed emissions appearing at 2224 UT in the MLT[2] midnight region coincident with a large abrupt change in IMF B_y and an enhancement in the solar wind density. Subsequently the emission region drifted eastward and expanded poleward. No X-ray emissions were detected by PIXIE at this time.

At 2242 UT a much more intense event started with a particle injection observed at geosynchronous orbit. At this time there was a further enhancement in the solar wind density, but otherwise no significant changes in the solar wind were observed. This event developed into a fully-fledged substorm with classical features: rapid poleward expansion, development of a bulge and a westward travelling surge and eastward drift of emission features.

The initial injection was seen at 2242 UT as a dispersionless signature in the electron fluxes by the geosynchronous satellite 1990-095 situated at 1950 MLT. Differential electron fluxes from this and two other LANL satellites are displayed in Fig. 5.3. Five minutes later, at 2247 UT, the injection was seen as a dispersed signal at LANL-97A located at 0301 MLT. The injected electrons drifted further eastward and at 2249 UT the dispersed signal was detected by 1994-084 at 0521 MLT.

At the location where the particles are injected, all fluxes will increase simultaneously, as was seen by by the LANL satellite in the evening sector. Subsequently injected electrons will drift eastward, and their drift velocity will depend an their energy, so that the more energetic electrons will reach the two LANL satellites in the early morning sector first, and less energetic electrons will arrive later. The observed drift time corresponds to 18 minutes for a full orbit around the Earth.

A simple drift time calculation can be performed with the relation (Østgaard et al. 1999b):

$$E = \frac{C}{Lt}, \tag{5.1}$$

where the energy E of the particles is given in MeV, the L parameter in R_E and the drift time t for a full orbit around the Earth in minutes. The constant C is 44 for equatorial pitch angles of 90°, and 66 for equatorial pitch angles $< 10°$ (precipitating particles). Using the value 44 for trapped particles a drift time of

[2]See Appendix A.

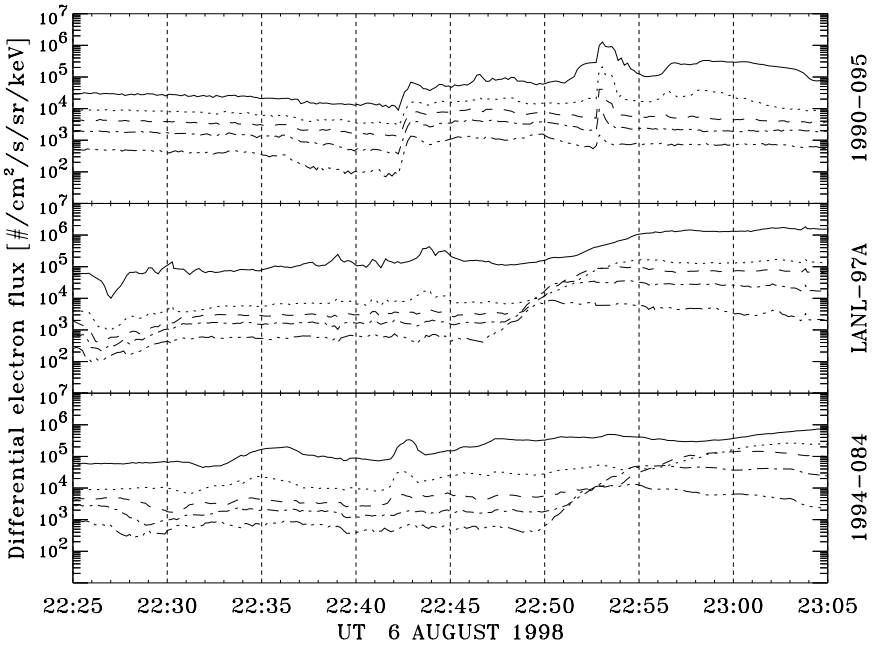

Figure 5.3: **Geosynchronous differential electron fluxes, 6 August 1998.** The data are from three geostationary LANL satellites: **Top panel:** 1990-095 was located at 1950 MLT at 2242 UT. **Middle panel:** LANL-97A was located at 0301 MLT at 2247 UT. **Bottom panel:** 1994-084 was located at 0521 MLT at 2249 UT. Differential electron energy fluxes were recorded in five energy bins: **Solid line:** 50–75 keV. **Dotted line:** 75–105 keV. **Dashed line:** 105–150 keV. **Dash-dotted line:** 150–225 keV. **Dash-dot-dot-dot line:** 225–315 keV. LANL energetic particle data were provided by G. Reeves, Los Alamos National Laboratory, USA.

18 minutes is obtained for a particle energy of 370 keV. This corresponds fairly well with the maximum energy 315 keV of the highest energy bin.

At this time the Geotail satellite resided in the inner magnetosphere very close to the equatorial plane at (-9, 0.8, 0.6 R_E GSE). At about 2242 UT Geotail observed the initiation of a dipolarization of the magnetic field, see Fig. 5.4, and at 2245 UT it observed an increase in particle energies (data not shown), both typical signatures of substorm onset.

In the ensuing substorm precipitating electrons were of high enough energy to create bright X-ray aurora from the dusk sector and into the morning sector. The flux enhancement observed at geosynchronous orbit at 2253 UT by 1990-095 corresponded to an auroral brightening which could be seen in images from

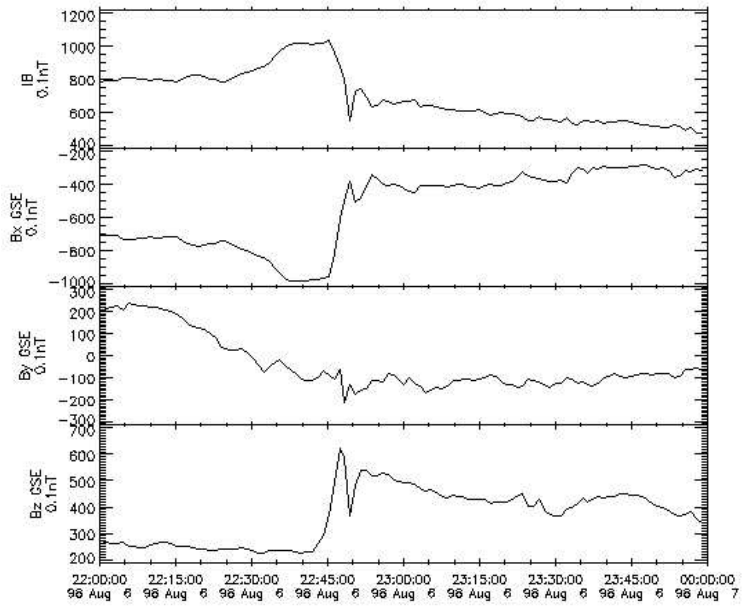

Figure 5.4: **Geotail magnetic field data, 6 August 1998. Panel 1:** Total magnetic field. **Panels 2–4:** X, Y and Z GSE components of the magnetic field. Units on the y axis are tenths of nT. Geotail was located at (-9, 0.8, 0.6 R_E GSE). Geotail magnetic field data were obtained through CDAWeb and provided by S. Kokubun, STELAB, Nagoya University, Japan.

Polar/UVI.

The intense transient precipitation event to be discussed in the following occurred in the dusk sector at 2259 UT in the late expansion phase of the substorm. No particle injections were observed at that time by the magnetospheric monitors.

5.3 Images from PIXIE and Polar/UVI

Figure 5.5 shows five-minute integration images from the PIXIE rear chamber. The first three images show the classical development of a substorm after onset, as seen in the high-energy regime depicted by the X-ray aurora. Expansion and eastward drift of the emission region is seen. The last three images show the sudden appearance and subsequent fading of a localized high-intensity energetic electron precipitation event.

From one-minute images, see Fig. 5.6, the onset and duration of the X-ray event were determined. These images are noisy as the time resolution is pushed

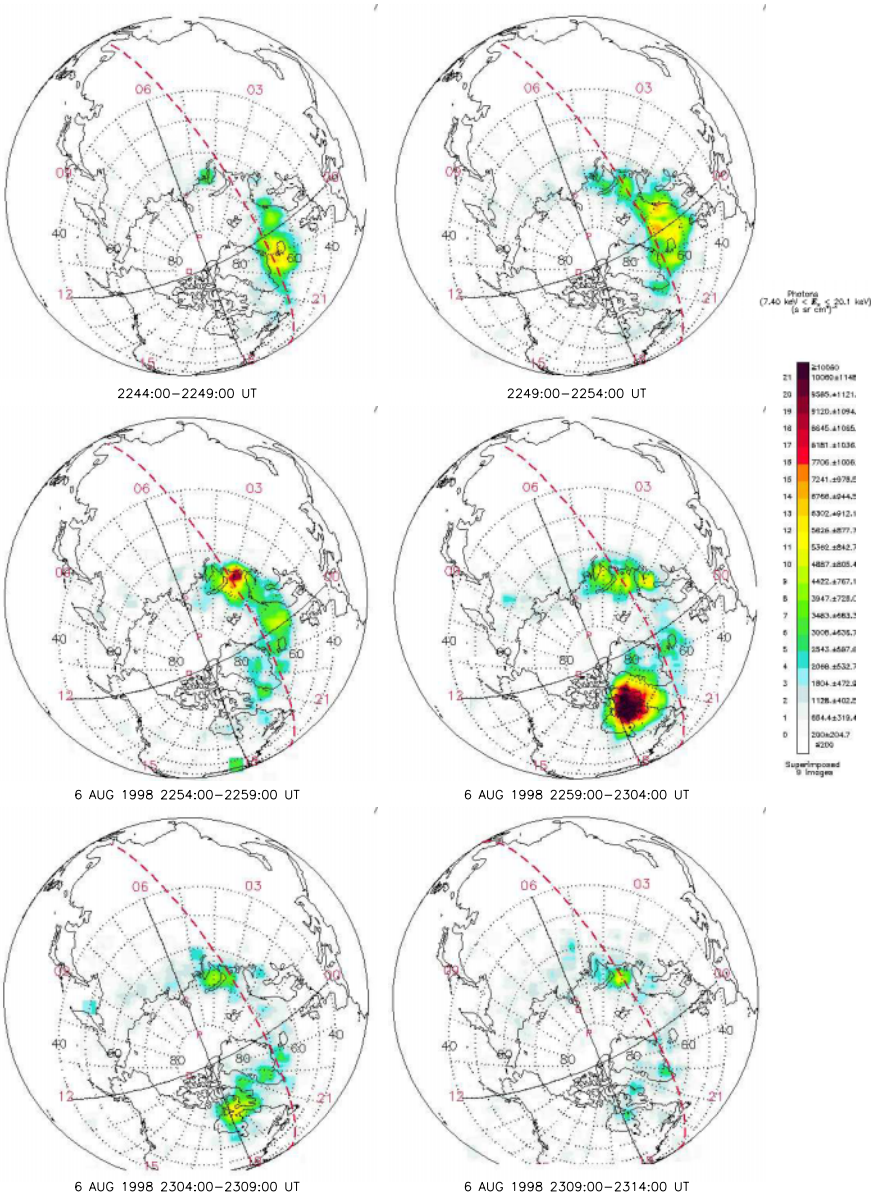

Figure 5.5: **Five minute resolution images from PIXIE, 6 August 1998.** Five minute integrations of X-rays in the energy interval 7.40–20.1 keV. The time interval is indicated under each image. The colour scale gives the X-ray intensity in units of photons/cm^2/s/sr in the energy interval. The grid shows CGM latitude and MLT. The terminator is indicated with a dashed red line. Courtesy of Nikolai Østgaard.

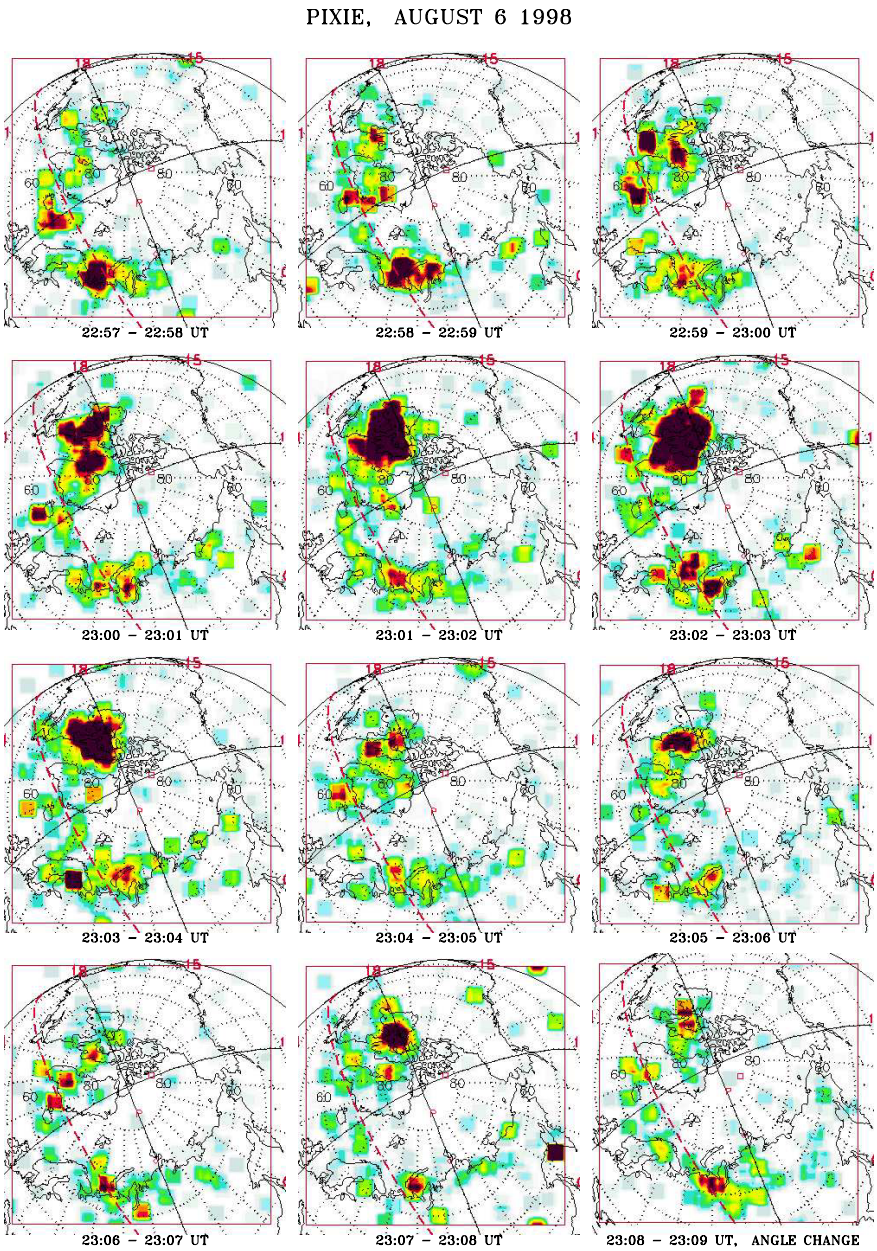

Figure 5.6: **One minute resolution images from PIXIE, 6 August 1998.** One minute integrations of X-rays in the energy interval 7.40–20.1 keV. The time interval is indicated under each image. The colour scale gives the X-ray intensity from 0 to 7000 photons/cm^2/s/sr in the energy interval. The grid shows CGM latitude and MLT. The terminator is indicated with a dashed red line. Courtesy of Nikolai Østgaard.

to the limit, but they allow for a better temporal and spatial analysis of the event. They show that the onset was at 2259 UT and the precipitation was most intense at 2300–2304 UT. At 2309 UT it had faded away. There is some evidence in the one-minute images that the precipitation region expanded westward and poleward in the first four minutes, 2259–2303 UT.

In images from UVI, see Fig. 5.7, the event looks remarkably different. In

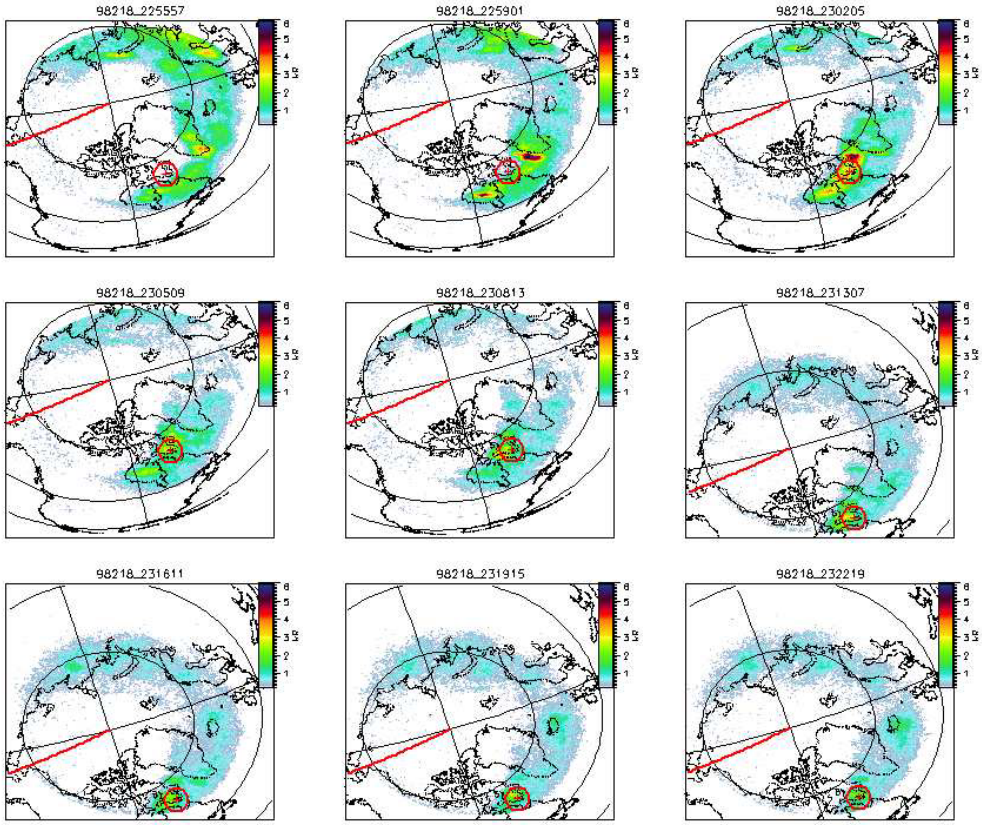

Figure 5.7: **Images from Polar/UVI, 6 August 1998.** 36 s integrations in the LBHl band with time stamps marking the beginning of the interval. The colour code gives the emission intensity in kR. The location of Iqaluit is marked with a red cross and a circle. The circle indicates the area for which spectral information about the precipitating electrons are derived. The solid black lines are a geographic grid with latitudes 50° and 70° shown. The noon meridian is indicated with a red line. Courtesy of Glynn Germany.

the UV images the event does not have the isolated semblance it does in the X-ray images. Rather it appears as an intense brightening of the poleward expanding eveningside aurora. Likely the bright emissions were caused by the progression of

a westward travelling surge; the long time interval (about three minutes) between images makes it hard to distinguish whether the movement was mainly poleward or westward.

In the first image, 2255 UT, emissions are seen equatorward of Iqaluit whose location is marked by a cross in a circle. In the second image, 2259 UT, the eveningside emissions reach farther poleward and the northern edge is situated immediately south of the station. By the time of the next image, at 2302 UT, an intense arc of emissions is seen over the station. Emissions linger over the station for the next 20 minutes, but with reduced brightness.

The different appearance of the event in the two wavelength regimes indicates that the precipitating electrons causing the brightening are of higher energy than those responsible for the emissions seen south of Iqaluit prior to the event and those creating the aurora lingering over the station after the event has subsided.

5.4 Imaging riometer data

Below are presented data from the conjugate stations Iqaluit in arctic Canada and South Pole station at the geographic south pole in Antarctica.

The locations of imaging riometers and magnetometer stations in Greenland and arctic Canada are shown in Fig. 5.8, as well as the conjugate position of South Pole. The conjugate position is shown as calculated with CGM coordinates (unaffected by diurnal effects or solar wind conditions) and as obtained by a calculation with T96[3] for the conditions of the studied event. It is evident that the stations of Iqaluit and South Pole are closely conjugate, and the conjugacy is improved for the solar wind conditions experienced during the event on 6 August 1998. The longitude of the conjugate point is very sensitive to IMF B_y which varied gradually from -10 nT 20 minutes before the event to +10 nT 20 minutes after. At 23 UT B_y was zero, and this was the value used in the calculations.

The recordings from the two imaging riometers are remarkably alike, both in timing, morphology and absorption intensity. Figure 5.9 shows concurrent time series of absorption images from Iqaluit and South Pole during the event.

In both hemispheres an arc-shaped absorption region about 100 km in latitudinal width and roughly aligned along the geomagnetic east-west direction is observed.

[3]The T96 (see p. 32) model result was obtained via the web pages of NASA's National Space Science Data Center.

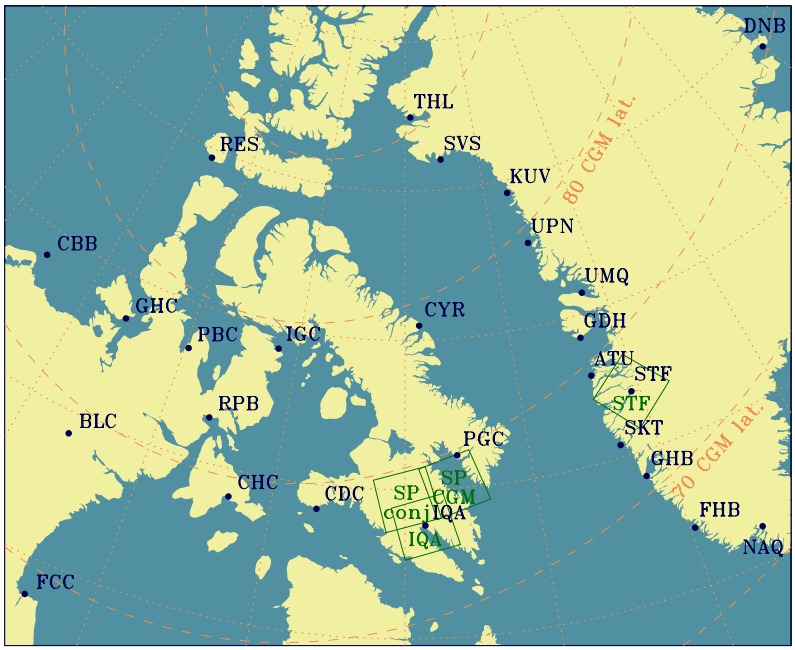

Figure 5.8: **Stations in western Greenland and arctic Canada. Dots** mark the location of magnetometer stations and their abbreviated names are given in dark blue. **Open squares** indicate the 250 by 250 km field-of-view of imaging riometers, including the conjugate position of the South Pole riometer in CGM coordinates (marked 'SP CGM'), and in a more accurate T96 calculation (marked 'SP conj') which takes current solar wind conditions at 23 UT 6 August 1998 into account. **Dotted lines** constitute a geographic grid with 5° divisions in latitude and 10° in longitude. **Dashed lines** are CGM contours of geomagnetic latitude.

The arc exhibits small-scale structure down to the spatial resolution of the riometer, i.e. a few tens of km. The sudden intensification seen in both hemispheres at 2301:48 UT occurred in a spatially confined region within the arc. Thus it was clearly a temporal feature and not the effect of a precipitation region moving into the field-of-view.

The arc itself did, however, move poleward with a velocity of 1.5 km/s determined from the progression of the poleward edge across the field-of-view. This speed is in agreement with that of poleward expansion of auroral absorption spikes (Nielsen 1980) and typical substorm speeds of poleward expansion (Akasofu 1964).

Ground magnetometer recordings from the two stations are consistent with a

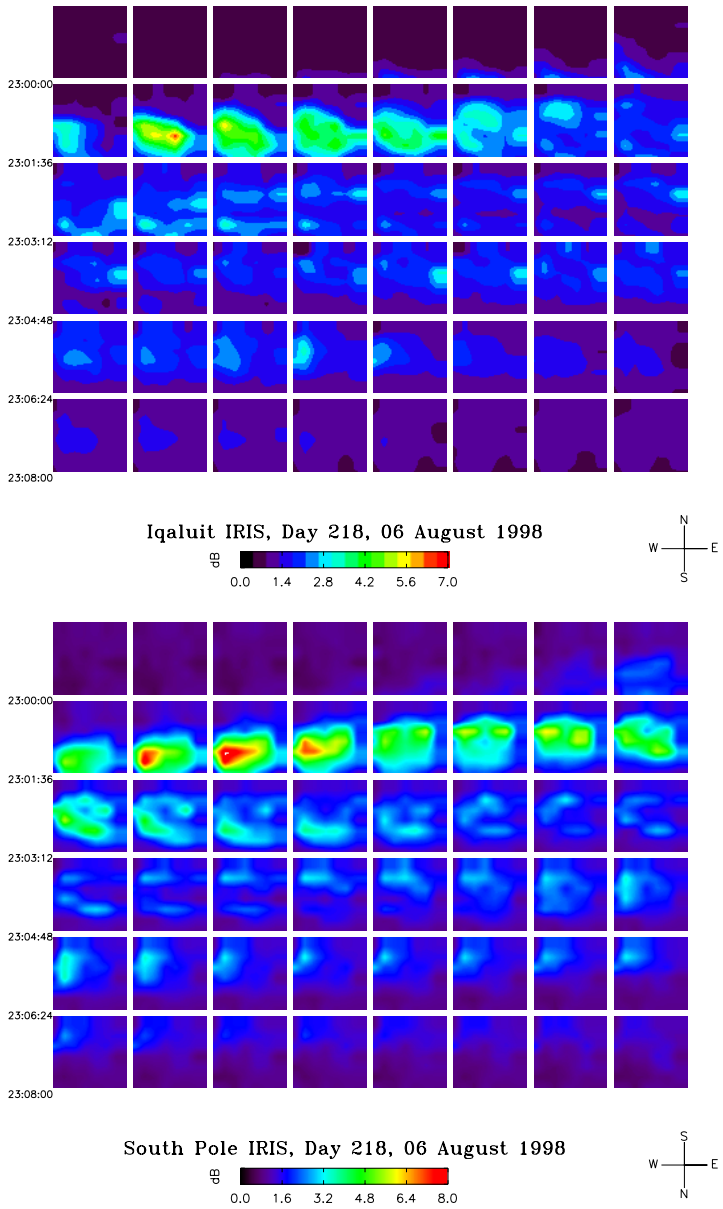

Figure 5.9: **Time series of absorption images on 6 August 1998.** Data from the conjugate riometers in Iqaluit (**top**) and South Pole (**bottom**). Poleward is up and east is to the right in both cases. The colour scale gives absorption intensity in dB; note that the scales differ slightly. Time resolution is 12 s. The time interval covered is 2300:00–2309:24 UT. Courtesy of Jim Etter.

westward current moving poleward over the stations (Christensen et al. 2003).

The maximum absorption reached during the event exceeded 7 dB in a few beams in both hemispheres, reaching as high as 9 dB at South Pole. Such high absorption levels are rare.

Figure 5.10 compares X-ray intensity in a circle of 570 km radius over Iqaluit with absorption from the two conjugate riometers. The recordings from the 49

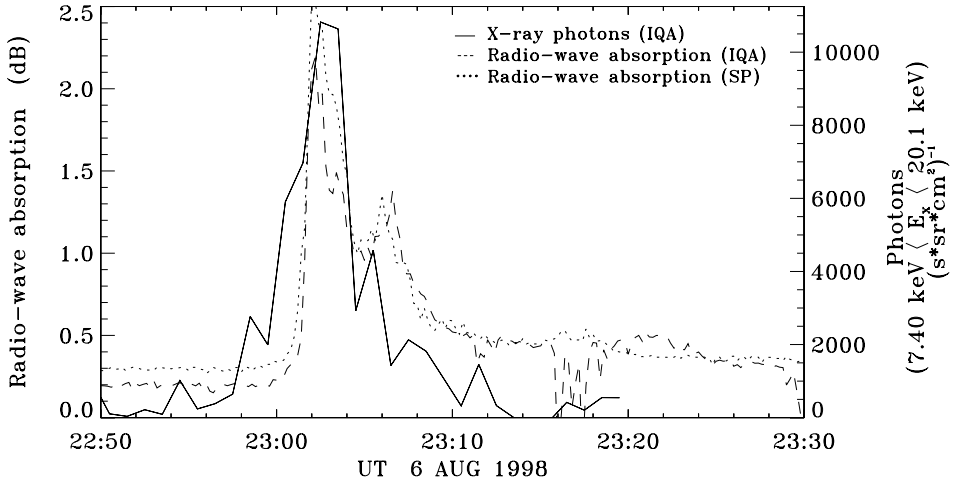

Figure 5.10: **X-ray flux and absorption intensity, 6 August 1998. Solid line:** Integrated X-ray flux from the PIXIE rear chamber in the energy interval 7.4–20.1 keV in a 570 km circle over Iqaluit. **Dashed line:** Iqaluit and **dotted line:** South Pole imaging riometer recordings averaged over all 49 beams.

beams of each imaging riometer are combined in a simple average. The PIXIE data is from the rear chamber, covering energies from 7.40 to 20.1 keV and the time resolution is one minute. The correlation between the three data sets is high, supporting the view that the energetic electron precipitation is confined to a relatively small region covered by both the riometer and PIXIE field-of-view.

5.5 Energy of the precipitating electrons

Unfortunately the duty cycling of the power supply of the PIXIE front chamber is so disadvantageous that data are unavailable from 2300–2306 UT, i.e. during the intense part of the event. Before and after this time interval it was attempted to obtain X-ray spectra, but the quality was too poor. The spectra were subject

to high noise levels and showed non-monotonous behaviour and were in the end deemed unreliable.

Instead spectral parameters for the precipitating electrons are derived from other sources: from UVI for the northern hemisphere and from ground-based observations for the southern hemisphere.

5.5.1 Electron energy derived from UVI data

By combining UV images obtained with the two specially designed filters LBHl and LBHs spectral information about the precipitating electrons can be derived (see Section 3.9).

As demonstrated the event was characterized by rapid movement and intensification occurring on a short time scale. Since the UVI alternates between filters, the image pairs for deducing diagnostic line ratios were not simultaneous. Therefore a rather large spatial area, a circle of 370 km radius, was used to better ascertain that the same emission features were sampled.

Results for an assumed Maxwellian electron energy spectrum show a hardening during the intense event with a mean energy of 20 keV at 2302 UT and 10 keV before and after this time.

5.5.2 Electron energy from ground-based observations

South Pole station is equipped with a multitude of ground-based instruments, including a 30 MHz broad-beam riometer and photometers measuring the [O I] 630.0 nm and N_2^+ 427.8 nm emission lines. The field-of-view of the broad-beam riometer is 55°, as defined by the beam width at which the perimeter sensitivity is 3 dB lower than the maximum (zenith) sensitivity. Very strong absorption events taking place just outside this field-of-view are still able to give a significant response, however. The photometers are hard-collimated to a 60° field-of-view to enable good comparison with the broad-beam riometer. The field-of-view of the broad-beam antenna corresponds roughly to the central nine beams of the imaging riometer, cf. Fig. 3.1.

Data from the two photometers and the 30 MHz riometer are presented in the first three panels of Fig. 5.11. The intensity ratio of the two auroral emission lines at 630.0 nm and 427.8 nm is correlated to the energy of the precipitating electrons. Rees & Luckey (1974) did model calculations for Maxwellian spectra of characteristic energies between 0.3 and 10 keV. Extrapolating their results to slightly

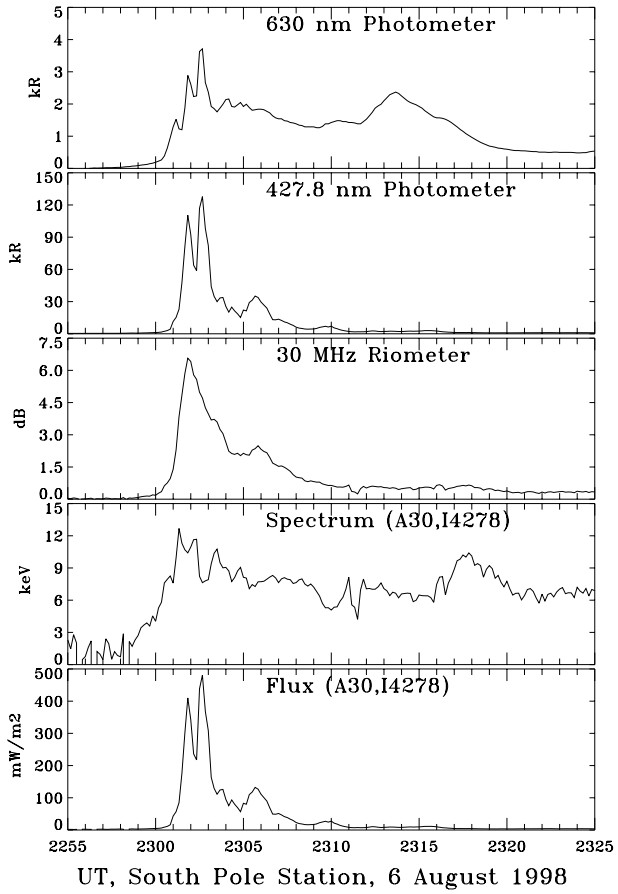

Figure 5.11: **Data from South Pole photometers and riometer, 6 August 1998. Panel 1:** Intensity of 630.0 nm emissions. **Panel 2:** Intensity of 427.8 nm emissions. **Panel 3:** Absorption intensity data from 30 MHz broad-beam riometer. **Panel 4:** Model calculation of the characteristic energy of the precipitating electrons, assuming an exponential spectrum. **Panel 5:** Model calculation of the energy flux of precipitating electrons. Courtesy of Dan Detrick.

higher energies, a characteristic energy of 15 keV is found from the auroral line ratio at 2302 UT. This corresponds to a mean energy of 30 keV.

The 110 s lifetime of the metastable [O I] 630.0 nm transition (see p. 27) makes it somewhat unreliable in an event characterized by rapid movement and changes in intensity. Using model calculations of the ionospheric effects of precipitating electrons the electron energy spectrum can be derived from radio-wave absorption and N_2^+ 427.8 nm intensity instead.

The model (see p. 87) was run by Dan Detrick at the University of Maryland for a series of input spectra, Maxwellian as well as exponential, with characteristic energies in the range 1–100 keV and total energy fluxes between 10^{-5} and 10^{6} mW/m^2. The output was 30 MHz broad-beam riometer absorption and intensity of the 427.8 nm emission. The results for exponential spectra are shown in Fig. 5.12.

Tabulated output for an assumed spectral shape can be used as a database to determine the spectral characteristics of the precipitating electrons based on the observables from the ground-based installations. For the observational data for this event the model results for an exponential electron energy spectrum are displayed in the two last panels of Fig. 5.11 showing characteristic energy and total energy flux, respectively. At the peak of the 30 MHz riometer absorption at 2302 UT the resulting characteristic energy is 10.5 keV and the total energy flux is 400 mW/m^2, corresponding to an electron flux of 2.3×10^{9} cm^2/kev/s. After the peak the characteristic energy is 6–8 keV for at least 15 minutes. A spectral hardening occurring at the peak in intensity is less pronounced than for the UVI-based calculations.

PIXIE detected a directional X-ray flux of 900 ± 150 cm^2/kev/s/sr from a zenith angle of 38°.2. Using results from Walt et al. (1979) for $\alpha = 10$ keV and an emission angle relative to vertical down, $\theta_\gamma = 140°$ the expected electron flux is 1.8×10^{9} cm^2/s/sr in good agreement with the derived electron flux at the conjugate site.

The double-peaked nature of the photometer data where the riometer absorption has a single broader peak is likely due to movement into and out of the field-of-view of the photometers, whereas the riometer maintains sensitivity beyond the nominal field-of-view. This introduces an uncertainty in the results of the model calculations.

5.6 The source of electrons

One is lead to speculate about the cause of the transient, intense electron precipitation at such high latitude. The energy of the electrons was not established with the desired accuracy since the X-ray data could unfortunately not be incorporated in the calculations, but a hardening of the spectrum at 2302 UT (at the time where X-ray and UV emissions and radio-wave absorption peaked) was demonstrated.

One might speculate whether the event could have been due to much more

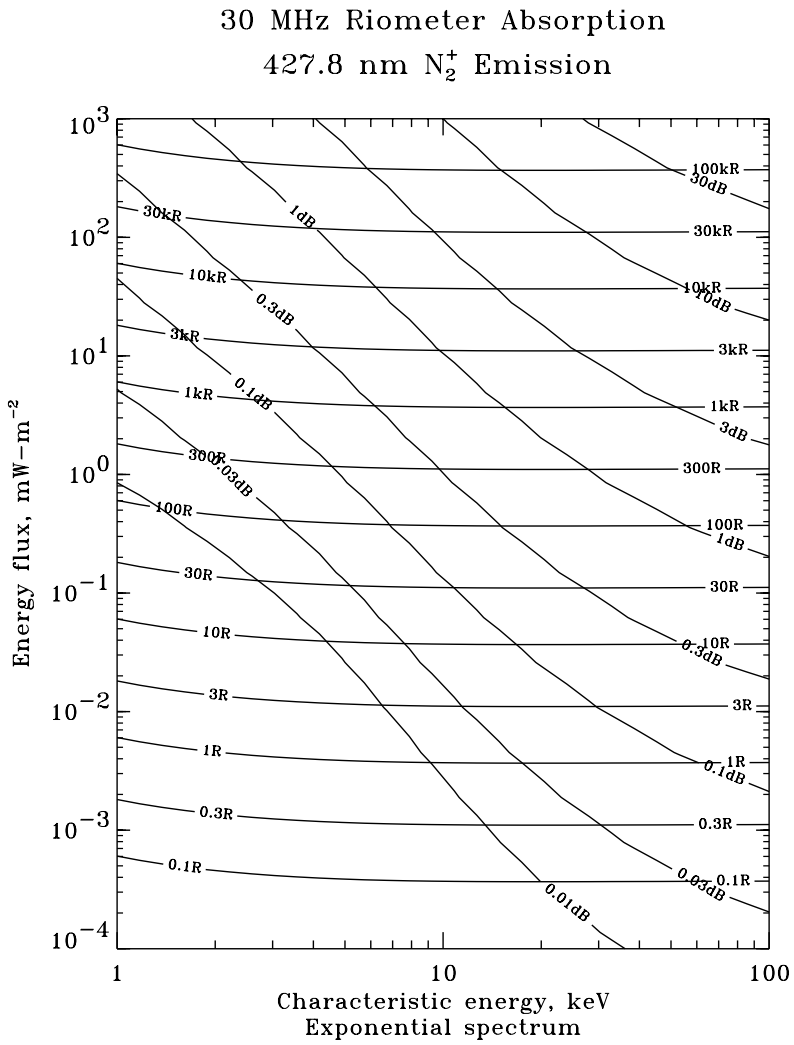

Figure 5.12: **Model calculations of radio-wave absorption and N_2^+ 427.8 nm intensity.** For input exponential electron spectra model calculations are run for characteristic energies in the range 1–100 keV and total energy fluxes between 10^{-5} and 10^6 mW/m^2. The resulting 30 MHz broad-beam riometer absorption and emission intensity at 427.8 nm are plotted as functions of the input spectral parameters. Courtesy of Dan Detrick.

energetic electrons than the above results indicate. A group at Aerospace Corporation have observed X-rays of very high energies at similar magnetic latitude (Bernard J. Blake, private communication). The X-rays were detected by the SAMPEX satellite (see p. 54). How such energetic electrons can be present at L = 14 remains a mystery, though.

Lorentzen et al. (2000) studied an X-ray event at similar MLT and in the same phase of a substorm as the present study. The electrons responsible for the X-ray production were relativistic. The event occurred at subauroral latitude and was likely due to pitch-angle scattering of radiation belt electrons caused by resonance with electromagnetic ion cyclotron mode waves. In the pseudo-trapping (or maybe even open field-line) regime of the present study this explanation cannot be invoked to account for the electron source, though.

Newell (2000) analyzed 1049 sharp electron flux enhancements events from a DMSP satellite. From their spectral characteristics the author found that all such events were associated with acceleration processes rather than with source plasma sheet density variations. One possible acceleration mechanism is by wave-particle interactions.

Another possibility is that downward acceleration of electrons can be achieved by a field-aligned potential drop. Creation of such a potential drop likely involves a feedback mechanism such as that described by Atkinson (1970): Conductivity enhancements due to particle precipitation tend to localize the field-aligned currents in the region of enhanced conductivity. This will lead to more intense currents and thus more precipitation which will further intensify the field-aligned currents. A potential drop can now be created by an instability developing because of an insufficient supply of magnetospheric electrons to sustain the upward field-aligned currents.

A similar mechanism that can give rise to a quickly growing and subsequently quickly decaying field-aligned potential was proposed by Stauning (1998) in an analysis of an event rather similar to the one studied here. From substorm modelling based on imaging riometer data and data from more than 80 polar region magnetometer stations he concluded that the very strong absorption observed at Kangerlussuaq was most likely caused by precipitation of magnetospheric electrons accelerated repeatedly through transient potentials of 10–30 kV. Olsson et al. (1996) derived potential drops of 10–15 keV for two westward travelling surge events.

From magnetometer data in the Canadian, Greenland and Scandinavian sectors maps of equivalent ionospheric plasma drift were constructed by Peter

Stauning by plotting the horizontal perturbation vectors rotated 90° counterclockwise. The data were interpolated and extrapolated to construct vector field plots with five minute intervals such as those shown in Fig. 5.13.

At 2230 UT the IMF B_y had just made a rapid change from strongly positive to strongly negative and the flow pattern began to change. The nearly circular dusk cell which had previously been seen began to elongate and its centre moved equatorward. At 2250 UT the antisunward flow across the polar cap started increasing in strength and strong electrojet flows were seen.

Figure 5.13 depicts the flow pattern around the time of the transient precipitation event. The dusk circulation cell shrank from a very elongated shape at 2255 UT to a less pronounced elongation at 2305 UT, greatly reducing the extent of the reversal boundary.

At this time there were no abrupt variations in the solar wind conditions which could be thought to initiate it. The IMF B_y had been increasing gradually for about 20 minutes when it became positive at 23 UT. It continued its gradual increase for some 20 minutes afterwards. This is likely to have caused a rearrangement of the magnetospheric configuration at a time characterized by very strong electrojet currents and cross polar cap flow causing strong shear at the boundary of flow reversal.

Around 23 UT Iqaluit was situated about 5° latitude poleward of the reversal boundary, a region where strong upward field-aligned currents were likely to occur, especially considering the highly disturbed conditions. It is thus conceivable that rearrangement of the magnetospheric flow could give rise to a field-aligned potential drop which accelerated the precipitating electrons responsible for the transient X-ray emissions and radio-wave absorption event.

A positive feedback mechanism such as that proposed by Stauning (1998) could be involved: A field-aligned potential drop associated with an intense upward current will affect the horizontal potential structures because of conductivity enhancements brought about by the precipitating electrons. Assuming the current is constant, the ionospheric potential will decrease. This will increase the field-aligned potential in a positive feedback. Alternatively the ionospheric potential can be considered constant. In this case the current will be increased and so also the potential drop, again creating a positive feedback.

The precipitation will cause an upward flux of secondary and back-scattered electrons which will weaken the potential drop, as will also the diffusion from the ambient plasma to the depleted acceleration region. This weakening of the potential drop will lead to another positive feedback mechanism where the decreasing

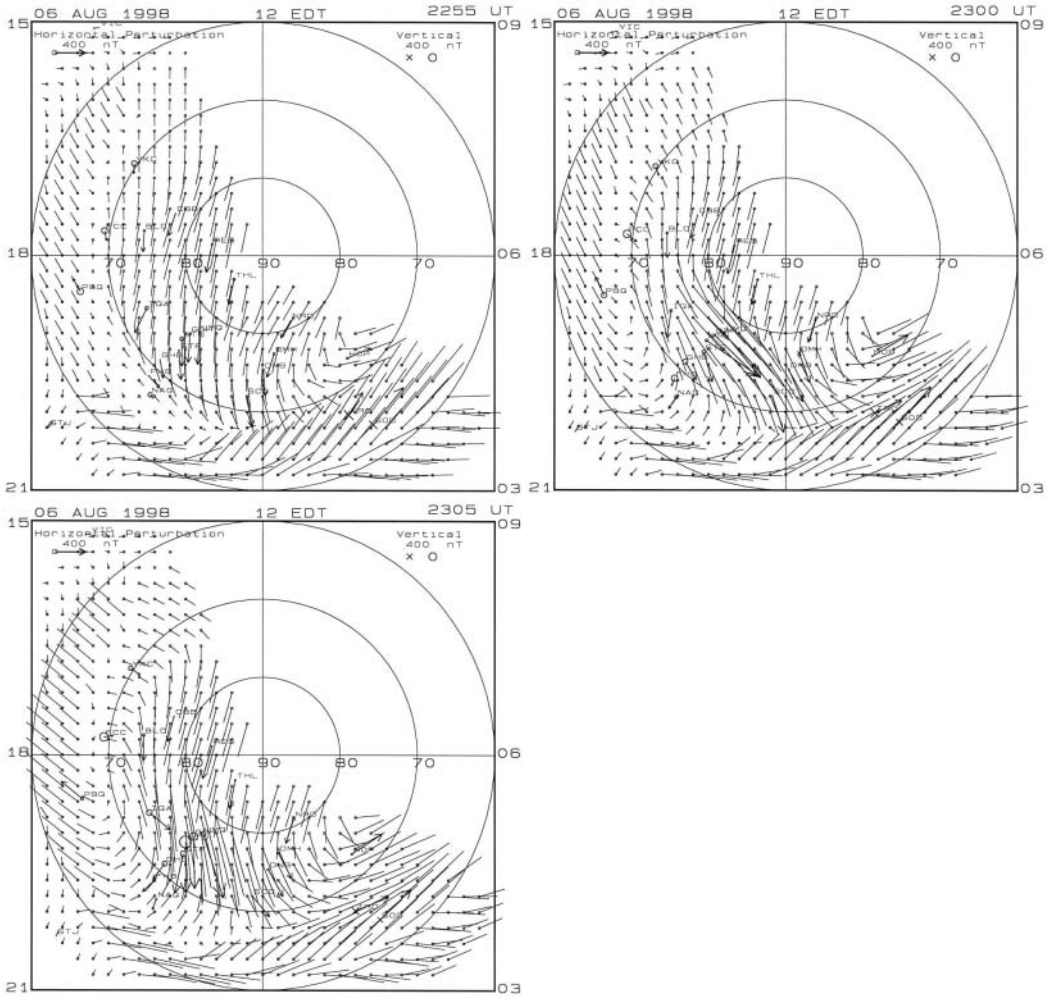

Figure 5.13: **Plots of equivalent ionospheric circulation, 6 August 1998.** Plotted are horizontal magnetic perturbation vectors rotated 90° counterclockwise. Data (shown with arrows) were interpolated and extrapolated and plotted at grid points indicated with a circle. The maps are for 2255 UT (**upper left**), 2300 UT (**upper right**) and 2305 UT (**bottom**). The coordinate grid is geomagnetic, using so-called eccentric dipole coordinates. Courtesy of Peter Stauning.

precipitating electron flux will lead to smaller ionospheric conductivities which by reversing the above arguments will lead to further degradation of the field-aligned potential drop.

This will lead to transient events since the accelerating mechanism will grow rapidly in strength, but will also decay quickly. The timing is likely to be determined by the Alfv´en velocity, giving rise and decay times of the order a few to a few tenth of seconds assuming an altitude of 1–2 R_E of the acceleration region (Stauning 1998).

The absorption peaks from both Iqaluit and South Pole have FWHM (full width at half maximum) of 10–20 s. In some beams several absorption enhancements follow the first and most intense spike. These also have FWHM of 10–20 s and are separated by about 30 s. As long as field-aligned currents of unstably high density persist, a new accelerating potential drop can be created after the previous one has vanished. It is conceivable from the time scales involved that bouncing electrons could have triggered the proposed feedback mechanism several times.

The magnetospheric source of electrons is probably related to a transient reconnection event in the magnetotail. Plasma heating and acceleration associated with bursts of reconnection is thought to be the cause of bursty bulk flow events. These are spatially localized enhancements in the flow in the near-Earth and mid-tail plasma sheet on a time scale of 10 minutes. Embedded in these flow enhancements are velocity peaks of about one minute duration called flow bursts (Angelopoulos et al. 1992).

Flow bursts have been demonstrated to be closely associated with several types of auroral activations, also at high geomagnetic latitude.

Fairfield et al. (1999) reported auroral brightenings near the poleward boundary of the auroral oval in connection with fast earthward magnetotail flow bursts.

Nakamura et al. (2001) selected 31 flow burst events from Geotail data and all turned out to be correlated with some auroral activation. For high-latitude activations the flow bursts were detected in the mid-tail region beyond 15 R_E. They were mainly observed during the recovery phase of a substorm when the reconnection region had probably moved so far tailward that earthward flows could not penetrate deep into the inner magnetosphere.

Ieda et al. (2001) identified 24 clear plasmoid signatures in data from Geotail and found that all were associated with auroral brightenings, if sometimes rather weak ones. Their data suggested that these brightenings were due to earthward flow bursts initiated by the reconnection event, rather than with the plasmoid or flux rope itself.

In the present case of 6 August 1998 Geotail was likely to have been in the central plasma sheet at the time of the event, a position which should be very good for detecting such events. Geotail did not detect any flow bursts around 23 UT on 6 August 1998, however. Since the event took place late in the substorm expansion phase, the reconnection region was likely to have retreated tailward. Thus a flow burst might not have penetrated into the innermost magnetotail and would not have given rise to particle flux enhancements neither at the position of Geotail at a distance of 9 R_E nor at geosynchronous orbit.

Moreover the event occurred in the evening sector around 19 MLT whereas the Geotail spacecraft was close to midnight. The transient nature and the probably limited spatial extent of bursty bulk flows makes it likely that if a flow burst caused the energetic precipitation event, it would have gone undetected by Geotail.

5.7 Conclusion

This chapter presented an analysis of a very intense electron precipitation event which caused a violent X-ray burst at high-latitude and gave rise to very strong and remarkably similar radio-wave absorption features in both hemispheres. The event was likely initiated by an earthward flow burst caused by a transient reconnection event in the magnetotail, and it was probably intensified by an acceleration mechanism present above the ionosphere.

The identification of similar events, especially if simultaneously detected by a magnetotail probe, is desirable. Rare events such as this are important for testing storm and substorm theories which have weaknesses in their description of the coupling between magnetospheric processes and their ionospheric manifestations. Extreme cases impose constraints on e.g. magneto-hydrodynamic models whose calculation results in the end must be able to account for the observed electron fluxes and energies.

Chapter 6

Conclusion

With the potential prospect of a Danish miniature Earth-observing X-ray imager in mind, a scheme for determining energy spectra of the precipitating electrons responsible for the X-ray production was devised. The deconvolution technique based on principles developed for solar X-rays was extended to take photon emission angles into account. The method is independent of assuming a specific spectral shape for either electrons or X-rays.

The scheme was validated with data from the Polar Ionospheric X-ray Imaging Experiment (PIXIE) on the Polar satellite. For the low spectral resolution of the PIXIE data, presumptions about the spectral shape turned out to be inescapable, however.

Comparisons were made between PIXIE data and data from ground-based riometers which are sensitive to precipitating electrons with energies exceeding about 10 keV, much the same as the PIXIE rear chamber which detected X-rays in the range 7–20 keV, approximately. The riometer field-of-view is somewhat smaller than the spatial resolution of PIXIE when Polar is close to apogee over the northern polar region, but nevertheless good correspondence was found between time series of X-ray data and radio-wave absorption measurements. Further validation of the X-ray inversion technique was accomplished by comparison of riometer measurements with expected radio-wave absorption intensities from model calculations based on the electron spectrum derived from the X-ray spectrum. Satisfactory agreement was observed between data and calculations.

An in-depth study was performed of a spectacular intense X-ray event occurring at high-latitude in the evening sector during the late expansion phase of a substorm on a day of storm-time magnetospheric conditions. Data from a multitude of instruments were compiled for a thorough description of the event: PIXIE

and Polar/UVI provided global images, geosynchronous satellites and the Geotail spacecraft contributed in situ particle and magnetic field measurements, solar wind parameters were obtained from the WIND satellite, and data from ground-based riometers, photometers and numerous magnetometers provided information about processes in the ionosphere.

The transient, localized enhancement in precipitating energetic electron flux, characterized by a temporarily hardening spectrum, was probably caused by an earthward flow burst in the magnetotail, possibly in connection with an accelerating mechanism present above the ionosphere.

Events such as this can throw light on the coupling between magnetospheric processes and their auroral manifestations which is not entirely satisfactorily described by present magnetospheric models.

Despite the limitation inherent in the low X-ray count rates which forces considerations about compromises and trade-offs between spectral, temporal and spatial resolution, bremsstrahlung X-rays are excellent for remote sensing of energetic auroral events. With an X-ray imager characteristics of the precipitating electrons can be remotely determined much more efficiently than by in situ particle measurements since large areas are probed concurrently, with the possibility of spatial coverage up to the full auroral oval, depending on the platform of the detector. X-rays are not contaminated by sunlight, airglow or the presence of proton aurora.

Future missions flying state of the art X-ray imagers such as a CnZnTe detector (Budtz-Jorgensen et al. 2001) could globally monitor energetic electron precipitation utilizing the X-ray inversion technique presented here. Especially if combined with a UV imager enabling characterization of the electrons of lower energy this holds the prospect of becoming a powerful tool for constraining theories of magnetospheric processes as well as determining ionospheric effects such as conductivities and energy deposition which have important applications in space weather.

Improved monitoring of energetic electron precipitation and better understanding of the processes generating them would enable more accurate space weather forecasts which predict the severity of magnetic disturbances and hence allows precautions to be taken with respect to the ensuing possible damaging effects on spacecraft in orbit, extended power and pipe lines, radio communications and trans-polar air flights.

Appendix A

Coordinates

Depending on the solar-terrestrial phenomenon studied, different coordinate system are appropriate for ordering data or describing physical processes. Those of main importance for magnetospheric and ionospheric physics are described here.

A.1 Geocentric solar ecliptic coordinates

Geocentric solar ecliptic (GSE) coordinates are often used to describe satellite orbits and solar wind and IMF data from monitors in the vicinity of the Earth. The x-axis points from the Earth to the Sun. The y-axis lies in the ecliptic plane pointing towards dusk (so the orbital motion of the Earth is in the negative y-direction). The z-axis is parallel to the ecliptic pole.

A.2 Geocentric solar magnetospheric coordinates

Geocentric solar magnetospheric (GSM) coordinates are convenient for describing the solar wind-magnetosphere interactions and the structure and processes of the magnetospheric regions. Therefore the parameters often given in GSE coordinates are also often given in GSM coordinates: orbital parameters and data from satellites in geospace. It is therefore necessary to check which coordinates are used as there is no default when working with satellite data. The GSM x-axis is like the GSE x-axis pointing from the Earth to the Sun. The z-axis is perpendicular to the x-axis and lies in the plane defined by the x-axis and the geomagnetic dipole axis. The z-axis points northward, but is generally not parallel to neither the rotational nor the dipole axis. The y-axis is defined so the system is orthogonal and is

thus perpendicular to the dipole. The y-axis is perpendicular to the geomagnetic dipole, so the dipole axis lies in the x-z plane. The z-axis is defined so the system is orthogonal and the positive z-axis direction is northward.

A.3 L shell and invariant latitude

Equivalent to the well-known geographic latitude of a point one can similarly define the magnetic latitude based on the direction of the dipole axis instead of the rotational axis. For ground-based and low-altitude observations the invariant latitude and the concept of L shells have been widely used. A point in space is defined by the dipole field line on which is lies. This field line is traced to the magnetic equatorial plane (perpendicular to the dipole axis) and the distance between the equatorial crossing to the centre of the Earth is called L and is measured in Earth radii. The magnetic latitude of the point where this field line intersects the surface of the Earth is called the invariant latitude, Λ. For a point on the surface the magnetic dipole latitude, λ equals Λ.

A.4 Corrected geomagnetic coordinates

The idea of defining magnetic coordinates based on the field line through the point is convenient, but a dipole field is not a very accurate description of the geomagnetic field. For corrected geomagnetic coordinates (CGM) a more appropriate model is used for the geomagnetic field when assigning magnetic latitude and longitude to a point. The International Association of Geomagnetism and Aeronomy recommends for scientific use the international geomagnetic reference field (IGRF) model. This empirical representation of the Earth's magnetic field is the main or core field (without external sources), and is based on ground magnetic observations and in two cases (Magsat in 1980 and Ørsted in 2000) also on accurate magnetic satellite observations. The coefficients for the spherical harmonics of the model are updated every five years. The CGM coordinates of a point in space is defined by tracing the IGRF field line through the point to the geomagnetic dipole equator and then trace backwards along a dipole field line to the same altitude. The dipole magnetic coordinates of the latter point is assigned to the starting point. CGM coordinates are not well defined close to the magnetic equator.

When using geomagnetic coordinates magnetic local time (MLT) is often given instead of longitude. For dipole coordinates MLT is the angle between the

midnight meridional plane and the meridional plane containing the point in question. CGM coordinates are not orthogonal, and MLT must be redefined. The UT time when the local CGM meridian of a point crosses the magnetic equator at midnight local time is used as a reference point. MLT can be calculated as the UT time offset by this local MLT midnight in UT.

A.5 Altitude adjusted CGM

Altitude adjusted corrected geomagnetic coordinates (AAGCM) differs from CGM coordinates in two important ways. Firstly, points lying on the same field line have the same magnetic latitude and longitude. Like for CGM coordinates the IGRF field line is traced from the starting point to the equator, but when returning along a dipole field line it is traced all the way to the surface, not to the starting altitude. Secondly, certain steps are taken to overcome the difficulties in the near-equatorial region where the coordinates are problematic. Still the accuracy is lower here. For mapping magnetospheric source regions to ionospheric phenomena it is very convenient that two points on the same field line have the same latitude and longitude. Note that for points on the surface of the Earth the AACGM coordinates are identical to the CGM coordinates.

A.6 Local coordinates

Ground-based magnetic variations are measured in coordinates which are defined locally, i.e. at a specific point on the Earth's surface like the position of the observatory. Three systems are used: a local geographic and two similarly defined local magnetic coordinate systems. For all the z-axis points vertically downward. For the XYZ system the x-axis points toward geographic north, while the y-axis is eastward. For the HEZ system the H-direction is towards the north magnetic pole while E is orthogonal to H and roughly eastward. The HDZ system is defined similarly to the HEZ system, but caution is needed since H here is the total horizontal component of the field while D defines the declination, i.e. the angle between the horizontal field direction and the direction towards magnetic north.

Appendix B

Geomagnetic indices

Magnetic indices are based on ground magnetic measurements and are empirically formed to characterize a specific parameter, as 'an index aims at giving summarised information in a continuous way concerning a more or less complex phenomenon which varies with time' (P. N. Mayaud as quoted by Rangarajan (1989)). Most used are the D_{st}, K_p and AE indices. D_{st} measures the severity of geomagnetic storms and the development of the ring current. K_p is a planetary index measuring the global disturbance level. AE characterizes the disturbance level of the auroral electrojets and thus the substorm intensity.

B.1 The D_{st} index

The D_{st} (storm-time disturbance) index is constructed from magnetograms from low-latitude stations evenly distributed in longitude. After carefully defining and removing the quiet level and daily variations, the residual field from the stations is averaged to give the D_{st} value for each hour. These stations are sensitive to the equatorial ring current and D_{st} provides information on the development of geomagnetic storms. Since storm-time recovery is very slow (of the order one week) it takes great care to define quiet periods for the calibration of the quiet level and daily variations.

B.2 The K_p, a_p and A_p indices

K_p (planetarische Kennziffer) is a quantitative measure of the level of planetary disturbance. For each station a quiet level is defined, and for each three hour in-

terval the difference between the maximum and the minimum excursion is calculated. This maximum disturbance is then translated to a reference value which can range from 0 to 9 with subdivisions to one third of a unit: 0_0, 0_+, 1_-, 1_0, 1_+,..., 8_-, 8_0, 8_+, 9_-, 9_0. When constructing the planetary average from the selected thirteen subauroral stations the subdivisions are interpreted as thirds, i.e. $3_- = 2\frac{2}{3}$. The K_p scale is quasi-logarithmic. There exists a conversion to a linear index, the equivalent amplitude a_p, which ranges from 0 (= 0_0) to 400 (= 9_0). K_p can also be defined as a daily value. The corresponding linear index is called the equivalent daily amplitude, A_p. Because of its global coverage K_p is widely used. It should, however, be mentioned that the coverage is far better in the northern than the southern hemisphere so the index is not completely globally balanced.

B.3 The AL, AU and AE indices

A number of world-wide auroral magnetometer stations are used to construct the auroral electrojet indices. AU is defined at any instant as the maximum positive excursion recorded by any station in the chain as measured relative to the quiet level. Similarly AL is the maximum negative excursion. Thus AU is a measure of the strength of the eastward electrojet and AL of the westward. The difference between the two, AE = AU − AL, approximates the total effect of both electrojets. At extremely disturbed conditions care needs to be taken as the electrojets can move so far equatorward that they are not properly sampled by the standard set of auroral stations.

Appendix C

List of publications

The following publications, posters and talks were brought about by the thesis project. The list includes two independent papers on Ørsted data one of which, the paper 'Mapping of field-aligned currents during northward IMF', was briefly touched upon in Section 2.3.1, whereas I did not find room to cover the paper 'Event Study of High-Energy Electron Precipitation by Comparison of Ørsted Data and Ground-Based Observations' which is a study of field-aligned currents and energetic electron precipitation during a pass of the Ørsted satellite over ground-based stations in Greenland. The performance of the Ørsted charged-particle detector was validated and caution was advised in application of the widely used approximation of infinite field-aligned current sheets which was shown to break down near midnight on this occasion.

All talks mentioned below were given by the author, regardless of who appears as first author below.

Publications in refereed journals

Christensen, T., Østgaard, N., Rosenberg, T. J., Detrick, D. L., Germany, G. A., Stauning, P., 2003, Conjugate High-Intensity Energetic Electron Precipitation at High Latitude, *Annales Geophysicae, in press*

Publications in refereed conference proceedings

Stauning, P., Christiansen, F., Watermann, J., Christensen, T., Rasmussen, O., 2002 Mapping of field-aligned currents during northward IMF, *Proceedings from First International Scientific CHAMP meeting, Potsdam, 23–26 January 2002, in press*

Publications in conference proceedings

Christensen, T., Stauning, P., Christiansen, F., Thayer, J., 2000, Event Study of High-Energy Electron Precipitation by Comparison of Ørsted Data and Ground-Based Observations, *Proceedings of Ørsted International Science Teem Meeting, Grasse, France, May 2–4 2000*

Conference talks

Christensen, T., Elektronnedbør, *Annual Meeting of the Network for Women in Physics in Denmark, Nyborg, Denmark, 1 June 2002*

Stauning, P., Watermann, J., Rasmussen, O., Christensen, T., Papitashvili, V., Observations from ground and from satellites of polar ionospheric effects of the 14 July 2000 solar storm event, *AGU fall meeting, San Francisco, CA., USA, 15–19 December 2000*

Popular talks

Christensen, T., Rumvejr og Nordlys, *Orion Planetarium, Jels, Denmark, 11 March 1999*

Christensen, T., Rumvejr og Nordlys, *Dansk Geofysisk Selskab, Copenhagen, Denmark, 1 October 2002*

Conference posters (first-author only)

Christensen, T., Energetic Electron Precipitation, *Danish Physical Society Annual Meeting, Nyborg, Denmark, 30–31 May 2002*

Christensen, T., Østgaard, N., Rosenberg, T. J., Detrick, D., Germany, G. A., Stauning, P., Conjugate High-Intensity Energetic Electron Precipitation at High Latitude, *EGS General Assembly, Nice, France, 22–26 April 2002*

Christensen, T., Østgaard, N., Rosenberg, T. J., Stauning, P., Germany, G. A., Watermann, J., A Conjugate Study of a Localized High-Energy Precipitation Event in the Evening Sector, *AGU fall meeting, San Francisco, CA., USA, 10–14 December 2001*

Christensen, T., Stauning, P., Thayer, J., Ørsted and Ground-Based Observations of High-Energy Electron Precipitation, *AGU fall meeting, San Francisco, CA., USA, 15–19 December 2000*

Christensen, T., Stauning, P., Thayer, J., High-energy electron precipitation study using Ørsted satellite and ground-based data, *Danish Physical Society Annual Meeting, Nyborg, Denmark, 8–9 June 2000*

Christensen, T., Stauning, P., Christiansen, F., Thayer, J., Event study of high-energy electron precipitation by comparison of Ørsted data and ground-based observations, *Ørsted International Science Team meeting, Grasse, France, 2–4 May 2000*

Christensen, T., Stauning, P., Christiansen, F., Thayer, J., High-energy electron precipitation from correlated satellite and ground-based observations, *EGS XXV General Assembly, Nice, France, 25–29 April 2000*

Christensen, T., Stauning, P., Christiansen, F., Neubert, T., Papitashvili, V. and Wu, J.-G., High-Energy Electron Precipitation and Field-Aligned Currents in the Cusp Region Measured From Ørsted Satellite and Correlated Ground-Based Observations of Ionospheric Convection and Absorption, *22nd General Assembly of the International Union of Geodesy and Geophysics, Birmingham, UK, 19–30 July 1999*

Christensen, T., Stauning, P., Wu, J.-G. and Neubert, T., Correlated Measurements of High-Energy Electron Precipitation and Field-Aligned Currents From Ørsted Satellite and Convection and Absorption Observations From Ground, *European Geophysical Society XXIV General Assembly, The Hague, The Netherlands, 19–23 April 1999*

Appendix D

Summary in Danish: Resumé af afhandlingen

Det fantastisk smukke og ærefrygtindgydende lysfænomen nordlys opstår som følge af vekselvirkningen mellem solvinden og Jordens magnetosfære. Magnetosfæren er den nære del af rummet der ligger ovenover atmosfæren, og som er domineret af Jordens magnetfelt der afbøjer solvindspartiklerne og således beskytter os mod deres potentielt ødelæggende bombardement. Solvinden bærer magnetisk flux stammende fra solen med sig, og dette interplanetare magnetfelt vekselvirker med Jordens magnetfelt hvor de støder ind i hinanden på dagsiden i omtrent 12 jordradiers afstand. Denne vekselvirkning giver anledning til en overførsel af energi i form af magnetisk flux som lagres på natsiden hvor magnetosfæren trækkes ud i en lang hale. Denne energitilførsel vil igangsætte processer i magnetohalen som accelererer de plasmapartikler der befinder sig i disse områder. Ladede partikler er med deres nyligt tilførte energi i stand til at trænge ned i den øvre atmosfære, og deres sammenstød med atmosfærens atomer og molekyler anslår disse til højere energitilstande. Når atomerne og molekylerne efterfølgende henfalder til deres grundtilstande, forårsages de lysudsendelser der udgør nordlyset. De ladede partikler er bundet til at følge Jordens magnetfeltlinjer og ledes af disse til høje breddegrader. Derfor forekommer nordlyset omkring Jorden i et bælte der indbefatter de nordligste regioner i Skandinavien, Rusland, Canada og Alaska. Tilsvarende findes et bælte om den sydlige halvkugle hvor sidestykket sydlys forekommer.

Fjernmåling af atmosfærisk røntgenstråling kan med fordel benyttes til studier af energirig elektronnedbør. Røntgenstråling har den fordel at det kan observeres døgnet rundt. Observationerne er upåvirkede af lysforurening fra solen eller fra

den lysudsendelse der hele tiden finder sted i ionosfæren når ioner indfanger elektroner og danner neutrale atomer og ioner. Men røntgennordlyset har ikke stor intensitet, og det kan være nærmest umuligt at opnå gode signal-støjforhold uden at gå på kompromis med den spektrale, den rumlige eller den tidsmæssige opløsning.

Røntgenstråling dannes i små 100 kilometers højde og vil absorberes i atmosfæren inden det når jordoverfladen. En mindre del vil udsendes i retninger opefter og kan undslippe atmosfæren. For at detektere røntgennordlyset må instrumenter monteres på raketter, balloner eller satellitter.

Ved påbegyndelsen af dette arbejde var der udsigt til at en dansk mikrosatellit med opsendelse i 2003 kunne blive udset til at bære et røntgenkamera til bl.a. nordlysstudier. Med denne mulighed for øje startede udviklingen af en procedure til bestemmelse af nedbørselektroners energispektre ud fra optagelser af røntgenspektre. Metoden er baseret på astrofysiske principper udviklet med det formål at studere røntgenstråler fra solen, og den er blevet udvidet til at omfatte de udsendte fotoners vinkelfordeling.

Metodens gyldighed blev afprøvet ved sammenligning med en anden velkendt procedure for udledning af røntgenspektre som er baseret på en database af omhyggelige modelberegninger. Til formålet benyttedes optagelser fra røntgeninstrumentet PIXIE på satellitten Polar der flyver i en elliptisk bane hvor det en stor del af tiden er muligt at observere hele nordlyszonen på en gang. God overensstemmelse kunne konstateres, og teknikken blev yderligere stadfæstet ved sammenligning mellem røntgenoptagelser og jordbaserede data fra en riometerinstallation i Kangerlussuaq (tidligere Søndre Strømfjord) i Grønland. Et riometer måler absorptionen af den galaktiske radiobaggrund. Denne radiostråling vil lide et vist tab på sin vej ned gennem ionosfæren, og absorptionen er et mål for indholdet af frie elektroner i ionosfæren. Ved sammenligning mellem optagelser fra PIXIE og absorptionsmålinger blev rigtigheden af de udledte spektre atter bekræftet.

En grundig analyse af en begivenhed med kraftig, men afgrænset røntgenstråling af omtrent ti minutters varighed blev præsenteret. Data fra mange kilder blev indsamlet for at forstå hvad der kunne give anledning til så intens elektronnedbør ved så høj breddegrad. Fænomenet forekom på en dag hvor magnetosfæren var præget af voldsomme forstyrrelser i solvinden. Store energimængder oplagret i magnetohalen blev udladet i en kraftig substormproces. Substorme er et almindeligt forekommende fænomen, men denne var temmelig kraftig og sandsynligvis har forskellige ting spillet sammen. Det er ganske tænkeligt at en magnetisk omkonfigurering i halen sent i substormens ekspansionsfase har givet anledning til at plasma er blevet accelereret ind mod Jorden. På magnetfeltlinjerne, der fører

elektronerne til høje breddegrader, har der været gunstige forhold for dannelse af en feltrettet spændingsforskel der kunne accelerere elektronerne yderligere.

Begivenheder som denne kan kaste lys på koblingen mellem magnetosfæren og ionosfæren som de nuværende magnetosfæremodeller har svært ved at redegøre tilfredsstillende for.

Fremtidige satellitter udstyret med højteknologiske røntgenkameraer, som eksempelvis den nyudviklede faststofdetektor der er blevet foreslået af et dansk forskerhold (Budtz-Jorgensen et al. 2001), vil være i stand til at udføre global overvågning af energirig elektronnedbør ved hjælp af den i denne afhandling præsenterede inversionsteknik for røntgenspektre. Specielt i kombination med data fra et UV-kamera der kan afsløre egenskaberne af de mindre energirige elektroner, har metoden potentialet til at blive et solidt værktøj der dels ville kunne bidrage til en bedre forståelse af fysiske processer i magnetosfæren, dels kunne give oplysninger om ændringer i ionosfærens ledningsevne og energitilførsel hvilket har stor relevans i forbindelse med vurdering af truslen fra geomagnetisk uvejr. Forbedrede varsler af geomagnetiske forstyrrelser kan give operatører tid til at tage forholdsregler for at undgå skader på satellitter og på langstrakte rørledninger og højspændingsnet samt tage højde for forstyrrelser af radiokommunikation og GPS-signaler og undgå øgede strålingsdoser for flypersonale på ruter henover polområderne.

Bibliography

Akasofu, S.-I. 1964, *The development of the auroral substorm,* Planet. Space Sci. 12, 273–282

Akasofu, S.-I. 1968, *Polar and Magnetospheric Substorms,* D. Reidel Publishing Company, Dordrecht, Holland

Aksnes, A., Stadsnes, J., Bjordal, J., Østgaard, N., Vondrak, R. R., Detrick, D. L., Rosenberg, T. J., Germany, G. A., Chenette, D. 2002, *Instantaneous ionospheric global conductance maps during an isolated substorm,* Ann. Geophys. 20, 1181–1191

Angelopoulos, V., Baumjohann, W., Kennel, C. F., Coroniti, F. V., Kivelson, M. G., Pellat, R., Walker, R. J., Lühr, H., Paschmann, G. 1992, *Bursty bulk flows in the inner central plasma sheet,* J. Geophys. Res. 97, 4027–4039

Atkinson, G. 1970, *Auroral arcs: Results of the interaction of a dynamic magnetosphere with the ionosphere,* J. Geophys. Res. 75, 4746–4755

Baker, D. N., Anderson, R. C., Zwickl, R. D., Slavin, J. A. 1987, *Average plasma and magnetic field variations in the distant magnetotail associated with near-Earth substorm effects,* J. Geophys. Res. 92, 71–81

Baker, D. N., Klimas, A. J., Vassiliadis, D., Pulkkinen, T. I., McPherron, R. L. 1997, *Reexamination of driven and unloading aspects of magnetospheric substorms,* J. Geophys. Res. 102, 7169–7177

Baker, D. N., Pulkkinen, T. I., Angelopoulos, V., Baumjohann, W., McPherron, R. L. 1996, *Neutral line model of substorms: Past results and present view,* J. Geophys. Res. 101, 12 975–13 010

Baker, D. N., Pulkkinen, T. I., Büchner, J., Klimas, A. J. 1999, *Substorms: A global instability of the magnetosphere-ionosphere system,* J. Geophys. Res. 104, 14 601–14 611

Berger, M. J., Seltzer, S. M. 1972, *Bremsstrahlung in the atmosphere,* J. Atmos. Terr. Phys. 34, 85–108

Berger, M. J., Seltzer, S. M., Maeda, K. 1970, *Energy deposition by auroral*

electrons in the atmosphere, J. Atmos. Terr. Phys. 32, 1015–1045

Biskamp, D. 2000, *Magnetic Reconnection in Plasmas*, Cambridge University Press, Cambridge, United Kingdom

Bohr, N. 1915, *On the decrease of velocity of swiftly moving electrified particles in passing through matter*, Phil. Mag. 30, 581–612

Bohr, N. 1948, *The penetration of atomic particles through matter*, Kgl. Danske Videnskabernes Selskab Mat.-Fys. Medd. XVIII, 8, 1–144

Bransden, B. H., Joachain, C. J. 1983, *Physics of Atoms and Molecules*, Longman Scientific and Technical, England

Brekke, A., Egeland, A. 1979, *Nordlyset — fra mytologi til romforskning*, Grøndahl & Søn Forlag A.s., Norge

Brekke, A., Egeland, A. 1980, *Ancient Norwegian literature in relation to the auroral oval*, in C. S. Deehr and J. A. Holtet (eds.), Exploration of the Polar Upper Atmosphere, pp 431–442, D. Reidel Publishing Company, Dordrecht, Holland

Brown, J. C. 1971, *The deduction of energy spectra of non-thermal electrons in flares from the observed dynamic spectra of hard X-ray bursts*, Solar Phys. 18, 489–502

Budtz-Jorgensen, C., Kuvvetli, I., Westergaard, N. J., Jonasson, P., Reglero, V., Eyles, C., Neubert, T. 2001, *The CZT X-ray imager on AXO*, Astrophys. Space Sci. 276, 281–289

Burch, J. L., Mende, S. B., Mitchell, D. G., Moore, T. E., Pollock, C. J., Reinisch, B. W., Sandel, B. R., Fuselier, S. A., Gallagher, D. L., Green, J. L., Perez, J. D., Reiff, P. H. 2001, *Views of Earth's magnetosphere with the IMAGE satellite*, Science 291, 619–624

Christensen, T., Østgaard, N., Rosenberg, T. J., Detrick, D. L., Germany, G. A., Stauning, P. 2003, *Conjugate high-intensity energetic electron precipitation at high latitude*, Ann. Geophys. in press

Clauer, C. R. 1994, *Solar wind control of high latitude dayside current systems*, in J. A. Holtet and A. Egeland (eds.), Physical Signatures of Magnetospheric Boundary Layer Processes, pp 29–41, Kluwer Academic Publishers, Dordrecht, The Netherlands

Coroniti, F. V., McPherron, R. L., Parks, G. K. 1968, *Studies of the magnetospheric substorm. 3. Concept of the magnetospheric substorm and its relation to electron precipitation and micropulsations*, J. Geophys. Res. 73, 1715–1722

Cowley, S. W. H., Morelli, J. P., Lockwood, M. 1991, *Dependence of convective flows and particle precipitation in the high-latitude ionosphere on the x and y*

components of the interplanetary magnetic field, J. Geophys. Res. 96, 5557–5564

Detrick, D. L. 1997, *Modelling Ionospheric Effects of Energy Deposition into the Atmosphere by Energetic Particles*, Unpublished, University of Maryland, College Park, MD, USA

Detrick, D. L., Rosenberg, T. J. 1990, *A phased-array radiowave imager for studies of cosmic noise absorption*, Radio Sci. 25, 325–338

Dungey, J. W. 1961, *Interplanetary magnetic field and the auroral zones*, Phys. Rev. Lett. 6, 47–48

Elwert, G. 1939, *Verschärfte Berechnung von Intensität und Polarisation im kontinuerlichen Röntgenspektrum*, Ann. Physik 34, 178–208

Elwert, G., Haug, E. 1969, *Calculation of bremsstrahlung cross sections with Sommerfeld-Maue eigenfunctions*, Phys. Rev. 183, 90–105

Fairfield, D. H., Mukai, T., Brittnacher, M., Reeves, G. D., Kokubun, S., Parks, G. K., Nagai, T., Matsumoto, H., Hashimoto, K., Gurnett, D. A., Yamamoto, T. 1999, *Earthward flow bursts in the inner magnetotail and their relation to auroral brightenings, AKR intensifications, geosynchronous particle injections and magnetic activity*, J. Geophys. Res. 104, 355–370

Fano, U., Koch, H. W., Motz, J. W. 1958, *Evaluation of bremsstrahlung cross sections at the high-frequency limit*, Phys. Rev. 112, 1679–1683

Frey, H. U., Mende, S. B., Carlson, C. W., Gérard, J.-C., Hubert, B., Spann, J., Gladstone, R., Immel, T. J. 2001, *The electron and proton aurora as seen by IMAGE-FUV and FAST*, Geophys. Res. Lett. 28, 1135–1138

Garcia, H. A. 1994, *Temperature and hard X-ray signatures for energetic proton events*, Astrophys. J. 420, 422–432

Germany, G. A., Parks, G. K., Brittnacher, M., Cumnock, J., Lummerzheim, D., Spann, J. F., Chen, L., Richards, P. G., Rich, F. J. 1997, *Remote determination of auroral energy characteristics during substorm activity*, Geophys. Res. Lett. 24, 995–998

Germany, G. A., Torr, D. G., Richards, P. G., Torr, M. R., John, S. 1994a, *Determination of ionospheric conductivities from FUV auroral emissions*, J. Geophys. Res. 99, 23 297–23 305

Germany, G. A., Torr, M. R., Torr, D. G., Richards, P. G. 1994b, *Use of FUV auroral emissions as diagnostic indicators*, J. Geophys. Res. 99, 383–388

Golub, L., Pasachoff, J. M. 2001, *Nearest Star — The Surprising Science of Our Sun*, Harvard University Press, Cambridge, MA, USA

Gonzalez, W. D., Joselyn, J. A., Kamide, Y., Kroehl, H. W., Rostoker, G., Tsu-

rutani, B. T., Vasyliunas, V. M. 1994, *What is a geomagnetic storm?*, J. Geophys. Res. 99, 5771–5792

Hajkowicz, L. A. 1990, *The dynamics of a steep onset in the conjugate auroral riometer absorption*, Planet. Space Sci. 38, 127–134

Hardy, D. A., Gussenhoven, M. S., Brautigam, D. 1989, *A statistical model of auroral ion precipitation*, J. Geophys. Res. 94, 370–392

Hardy, D. A., Gussenhoven, M. S., Holeman, E. 1985, *A statistical model of auroral electron precipitation*, J. Geophys. Res. 90, 4229–4248

Hargreaves, J. K. 1992, *The solar-terrestrial environment*, Cambridge University Press, Cambridge, United Kingdom

Hargreaves, J. K., Chivers, H. J. A., Nielsen, E. 1979, *Properties of spike events in auroral radio absorption*, J. Geophys. Res. 84, 4245–4250

Hones, Jr., E. W. 1977, *Substorm processes in the magnetotail: Comments on 'On hot tenous plasmas, fireballs, and boundary layers in the Earth's magnetotail' by L. A. Frank, K. L. Ackerson, R. L. Lepping*, J. Geophys. Res. 35, 5633–5640

Hones, Jr., E. W. 1979, *Transient phenomena in the magnetotail and their relation to substorms*, Space Sci. Rev. 23, 393–410

Hones, Jr., E. W., Baker, D. N., Bame, S. J., Feldman, W. C., Gosling, J. T., McComas, D. J., Zwickl, R. D., Slavin, J. A., Smith, E. J., Tsurutani, B. T. 1984, *Structure of the magnetotail at 200 $R_{\rm E}$ and its response to geomagnetic activity*, Geophys. Res. Lett. 11, 5–7

Ieda, A., Fairfield, D. H., Mukai, T., Saito, Y., Kokubun, S., Liou, K., Meng, C.-I., Parks, G. K., Brittnacher, M. J. 2001, *Plasmoid ejection and auroral brightenings*, J. Geophys. Res. 106, 3845–3857

Iijima, T., Potemra, T. A. 1976, *Field-aligned currents in the dayside cusp observed by Triad*, J. Geophys. Res. 81, 5971–5979

Imhof, W. L., Spear, K. A., Hamilton, J. W., Higgins, B. R., Murphy, M. J., Pronko, J. G., Vondrak, R. R., McKenzie, D. L., Rice, C. J., Gorney, D. J., Roux, D. A., Williams, R. L., Stein, J. A., Bjordal, J., Stadsnes, J., Njoten, K., Rosenberg, T. J., Lutz, L., Detrick, D. 1995, *The polar ionospheric X-ray imaging experiment (PIXIE)*, Space Sci. Rev. 71, 385–408

Jackson, J. D. 1998, *Classical Electrodynamics*, Third edition, John Wiley & Sons, Inc., New York, USA

Johns, C. M., Lin, R. P. 1992, *The derivation of parent electron spectra from bremsstrahlung hard X-ray spectra*, Solar Phys. 137, 121–140, Erratum 1992, Solar Phys. 142, 219

Kamide, Y. 1988, *Electrodynamical Processes in the Earth's Ionosphere and*

Magnetosphere, Kyoto Sangyo University Press, Kyoto, Japan

Kamide, Y., Baumjohann, W. 1993, *Magnetosphere-Ionosphere Coupling*, Springer-Verlag, Berlin, Germany

Kivelson, M. G., Russell, C. T. (eds.) 1995, *Introduction to Space Physics*, Cambridge University Press, Cambridge, United Kingdom

Koch, H. W., Motz, J. W. 1959, *Bremsstrahlung cross-section formulas and related data*, Rev. Mod. Phys. 31, 920–955

Kopka, H., Daly, P. W. 1995, *A Guide to LaTeX 2ε – Document Preparation for Beginners and Advanced Users*, Second edition, Addison-Wesley Publishing Company, Wokingham, England

Lee, C. M., Kissel, L., Pratt, R. H., Tseng, H. K. 1976, *Electron bremsstrahlung spectrum, 1–500 keV*, Phys. Rev. A 13, 1714–1727

Lodge, O. 1902, *Mr. Marconi's results in day and night wireless telegraphy*, Nature 66, 222

Lorence, L. J. 1992, *CEPXS/ONELD version 2.0: A discrete ordinates code package for general one-dimensional coupled electron-photon transport*, IEEE Trans. Nucl. Sci. 39, 1031–1034

Lorentzen, K. R., McCarthy, M. P., Parks, G. K., Foat, J. E., Millan, R. M., Smith, D. M., Lin, R. P. 2000, *Precipitation of relativistic electrons by interaction with electromagnetic ion cyclotron waves*, J. Geophys. Res. 105, 5381–5389

Luhmann, J. G. 1976, *Auroral electron spectra in the atmosphere*, J. Atmos. Terr. Phys. 38, 605–610

Luhmann, J. G. 1977, *Auroral bremsstrahlung spectra in the atmosphere*, J. Atmos. Terr. Phys. 39, 595–600

Luhmann, J. G., Blake, J. B. 1977, *Calculations of soft auroral bremsstrahlung and K_α line emission at satellite altitude*, J. Atmos. Terr. Phys. 39, 913–919

Lui, A. T. Y. 1996, *Current disruption in the Earth's magnetosphere: Observations and models*, J. Geophys. Res. 101, 13 067–13 088

Lui, A. T. Y. 2001, *A multiscale model for substorms*, Space Sci. Rev. 95, 325–345

Matthews, D. L., Rosenberg, T. J., Benbrook, J. R., Bering III, E. A. 1988, *Dayside energetic electron precipitation over the South Pole (λ = 75°)*, J. Geophys. Res. 93, 12 941–12 945

McDiarmid, I. B., Burrows, J. R., Budzinski, E. E. 1975, *Average characteristics of magnetospheric electrons (150 eV to 200 keV) at 1400 km*, J. Geophys. Res. 80, 73–79

McPherron, R. L. 1970, *Growth phase of magnetospheric substorms*, J. Geophys. Res. 75, 5592–5599

McPherron, R. L. 1995, *Magnetospheric dynamics*, in M. G. Kivelson and C. T. Russell (eds.), Introduction to Space Physics, pp 400–458, Cambridge University Press, Cambridge, United Kingdom

McPherron, R. L., Russell, C. T., Aubry, M. P. 1973, *Satellite studies of magnetospheric substorms on august 15, 1968. 9. Phenomenological model for substorms*, J. Geophys. Res. 78, 3131–3149

Mende, S. B., Frey, H. U., Lampton, M., Gérard, J.-C., Hubert, B., Fuselier, S., Spann, J., Gladstone, R., Burch, J. L. 2001, *Global observations of proton and electron auroras in a substorm*, Geophys. Res. Lett. 28, 1139–1142

Nakamura, R., Baker, D. N., Yamamoto, T., Belian, R. D., Bering III, E. A., Benbrook, J. R., Theall, J. R. 1994, *Particle and field signatures during pseudobreakup and major expansion onset*, J. Geophys. Res. 99, 207–221

Nakamura, R., Baumjohann, W., Brittnacher, M., Sergeev, V. A., Kubyshkina, M., Liou, K. 2001, *Flow bursts and auroral activations: Onset timing and foot point location*, J. Geophys. Res. 106, 10 777–10 789

Newell, P. T. 2000, *Reconsidering the inverted-V particle signature: Relative frequency of large-scale electron acceleration events*, J. Geophys. Res. 105, 15 779–15 794

Newell, P. T., Meng, C.-I. 1992, *Mapping the dayside ionosphere to the magnetosphere according to particle precipitation characteristics*, Geophys. Res. Lett. 19, 609–612

Newell, P. T., Meng, C.-I. 1994, *Ionospheric projections of magnetospheric regions under low and high solar wind pressure conditions*, J. Geophys. Res. 99, 273–286

Newell, P. T., Meng, C.-I., Lyons, K. M. 1996, *Suppression of discrete aurorae by sunlight*, Nature 381, 766–767

Nielsen, E. 1980, *Dynamics and spatial scale of auroral absorption spikes associated with the substorm expansion phase*, J. Geophys. Res. 85, 2092–2098

Nielsen, E., Axford, W. I. 1977, *Small scale auroral absorption events associated with substorms*, Nature 267, 502–504

Ohtani, S.-I. 2001, *Substorm trigger processes in the magnetotail: Recent observations and outstanding issues*, Space Sci. Rev. 95, 347–359

Olsson, A., Eriksson, A. I., Janhunen, P. 1996, *On the current-voltage relationship in auroral breakups and westwards-travelling surges*, Ann. Geophys. 14, 1265–1273

Osterbrock, D. E. 1989, *Astrophysics of Gaseous Nebulae and Active Galactic Nuclei*, University Science Books, California, USA

Østgaard, N., Bjordal, J., Stadsnes, J., Thorsen, E. 1999a, *PIXIE data processing at the University of Bergen*, Tech. Rep. 1999-05, University of Bergen, Bergen, Norway

Østgaard, N., Stadsnes, J., Bjordal, J., Germany, G. A., Vondrak, R. R., Parks, G. K., Cummer, S. A., Chenette, D. L., Pronko, J. G. 2001, *Auroral electron distributions derived from combined UV and X-ray emissions*, J. Geophys. Res. 106, 26 081–26 089

Østgaard, N., Stadsnes, J., Bjordal, J., Vondrak, R. R., Cummer, S. A., Chenette, D. L., Parks, G. K., Brittnacher, M. J., McKenzie, D. L. 1999b, *Global-scale electron precipitation features seen in UV and X rays during substorms*, J. Geophys. Res. 104, 10 191–10 204

Østgaard, N., Stadsnes, J., Bjordal, J., Vondrak, R. R., Cummer, S. A., Chenette, D. L., Schulz, M., Pronko, J. G. 2000, *Cause of the localized maximum of X-ray emission in the morning sector: A comparison with electron measurements*, J. Geophys. Res. 105, 20 869–20 883

Østgaard, N., Vondrak, R. R., Gjerloev, J. W., Germany, G. A. 2002, *A relation between the energy deposition by electron precipitation and geomagnetic indices during substorms*, J. Geophys. Res. 10.1029/2001JA002003

Papitashvili, V. O., Christiansen, F., Neubert, T. 2002, *A new model of field-aligned currents derived from high-precision satellite magnetic field data*, Geophys. Res. Lett. 10.1029/2001GL014207

Parks, G. K. 1991, *Physics of Space Plasmas*, Addison-Wesley Publishing Company, Redwood City, CA, USA

Paulsen, A. 1879, *Naturkræfterne, deres love og vigtigste anvendelser — Tredie bind*, P. G. Philipsens Forlag, Copenhagen, Denmark

Potemra, T. A. 1994, *Sources of large-scale Birkeland currents*, in J. A. Holtet and A. Egeland (eds.), Physical Signatures of Magnetospheric Boundary Layer Processes, pp 3–27, Kluwer Academic Publishers, Dordrecht, The Netherlands

Rangarajan, G. K. 1989, *Indices of geomagnetic activity*, in J. A. Jacobs (ed.), Geomagnetism — Volume 3, p. 323ff, Academic Press Limited, London, United Kingdom

Rees, M. H. 1963, *Auroral ionization and excitation by incident energetic electrons*, Planet. Space Sci. 11, 1209–1218

Rees, M. H. 1964a, *Ionization in the Earth's atmosphere by aurorally associated bremsstrahlung X-rays*, Planet. Space Sci. 12, 1093–1108

Rees, M. H. 1964b, *Note on the penetration of energetic electrons into the Earth's atmosphere*, Planet. Space Sci. 12, 722–725

Rees, M. H. 1989, *Physics and chemistry of the upper atmosphere*, Cambridge University Press, Cambridge, United Kingdom

Rees, M. H., Luckey, D. 1974, *Auroral electron energy derived from ratio of spectroscopic emissions. 1. Model computations*, J. Geophys. Res. 79, 5181–5186

Robinson, R. M., Vondrak, R. R. 1994, *Validation of techniques for space based remote sensing of auroral precipitation and its ionospheric effects*, Space Sci. Rev. 69, 331–407

Rosenberg, T. J., Detrick, D. L., Venkatesan, D., van Bavel, G. 1991, *A comparative study of imaging and broad-beam riometer measurements: The effect of spatial structure on the frequency dependence of auroral absorption*, J. Geophys. Res. 96, 17 793–17 803

Rosenberg, T. J., Siren, J. C., Lanzerotti, L. J. 1980, *High time resolution riometer and X-ray measurements of conjugate electron precipitation from the magnetosphere*, Nature 283, 278–280

Rostoker, G. 1998, *On the place of the pseudo-breakup in a magnetospheric substorm*, Geophys. Res. Lett. 25, 217–220

Rostoker, G., Akasofu, S.-I., Foster, J., Greenwald, R. A., Kamide, Y., Kawasaki, K., Lui, A. T. Y., McPherron, R. L., Russell, C. T. 1980, *Magnetospheric substorms—definitions and signatures*, J. Geophys. Res. 85, 1663–1668

Russell, C. T., McPherron, R. L. 1973, *The magnetotail and substorms*, Space Sci. Rev. 15, 205–266

Schunk, R. W., Nagy, A. F. 2000, *Ionospheres: Physics, Plasma Physics and Chemistry*, Cambridge University Press, Cambridge, United Kingdom

Seltzer, S. M., Berger, M. J. 1974, *Bremsstrahlung in the atmosphere at satellite altitudes*, J. Atmos. Terr. Phys. 36, 1283–1287

Shiokawa, K., Baumjohann, W., Haerendel, G., Paschmann, G., Fennell, J. F., Friis-Christensen, E., Lühr, H., Reeves, G. D., Russell, C. T., Sutcliffe, P. R., Takahashi, K. 1998, *High-speed ion flow, substorm current wedge, and multiple Pi 2 pulsations*, J. Geophys. Res. 103, 4491–4507

Silverman, S. M. 1980, *On the literature of the aurora in Nordic countries*, in C. S. Deehr and J. A. Holtet (eds.), Exploration of the Polar Upper Atmosphere, pp 443–448, D. Reidel Publishing Company, Dordrecht, Holland

Siren, J. C., Rosenberg, T. J., Detrick, D., Lanzerotti, L. J. 1980, *Conjugate ob-*

servation of electron microburst groups by bremsstrahlung X ray and riometer techniques, J. Geophys. Res. 85, 6760–6768

Smith, D. M., Lin, R. P., Anderson, K. A., Hurley, K., Johns, C. M. 1995, *High-resolution spectra of 20–300 keV hard X-rays from electron precipitation over Antartica*, J. Geophys. Res. 100, 19 675–19 685

Smith, Z., Dryer, M., Ort, E., Murtagh, W. 2000, *Performance of interplanetary shock prediction models: STOA and ISPM*, J. Atmos. Solar-Terr. Phys. 62, 1265–1274

Stauning, P. 1998, *Substorm modeling based on observations of an intense high-latitude absorption surge event*, J. Geophys. Res. 103, 26 433–26 452

Stauning, P. 2002, *Field-aligned ionosperic current systems observed from the Magsat and Ørsted satellites during northward IMF*, Geophys. Res. Lett. in press

Stauning, P., Christiansen, F., Watermann, J., Christensen, T., Rasmussen, O. 2002, *Mapping of field-aligned current patterns during northward IMF*, in Proceedings from First International Scientific CHAMP meeting, Potsdam, 23-26 Jan. 2002, in press

Stenbaek-Nielsen, H. C., Otto, A. 1997, *Conjugate auroras and the interplanetary magnetic field*, J. Geophys. Res. 102, 2223–2232

Thorsen, E. 1998, *Utvikling av programvare for behandling og analyse av målinger fra røntgenkameraet PIXIE på Polar-satellitten*, Master's thesis, University of Bergen, Bergen, Norway

Torr, M. R., Torr, D. G., Zukic, M., Johnson, R. B., Ajello, J., Banks, P., Clark, K., Cole, K., Keffer, C., Parks, G., Tsurutani, B., Spann, J. 1995, *A far ultraviolet imager for the international solar-terrestrial physics mission*, Space Sci. Rev. 71, 329–383

Tseng, H. K., Pratt, R. H., Lee, C. M. 1979, *Electron bremsstrahlung angular distributions in the 1–500 keV energy range*, Phys. Rev. A 19, 187–195

Tsyganenko, N. A. 1987, *Global quantitative models of the geomagnetic field in the cislunar magnetosphere for different disturbance levels*, Planet. Space Sci. 35, 1347–1358

Tsyganenko, N. A. 1989, *A magnetospheric magnetic field model with a warped tail current sheet*, Planet. Space Sci. 37, 5–20

Tsyganenko, N. A. 1995, *Modeling the Earth's magnetospheric magnetic field confined within a realistic magnetopause*, J. Geophys. Res. 100, 5599–5612

Vondrak, R., Robinson, R. 1985, *Inference of high-latitude ionization and conductivity from AE-C measurements of auroral electron fluxes*, J. Geophys. Res.

90, 7505–7512

Vondrak, R. R., Baron, M. J. 1976, *Radar measurements of the latitudinal variation of auroral ionization*, Radio Sci. 11, 939–946

Vondrak, R. R., Sears, R. D. 1978, *Comparison of incoherent scatter radar and photometric measurements of the energy distribution of auroral electrons*, J. Geophys. Res. 83, 1665–1667

Vorobjev, V. G., Yagodkina, O. I., Sibeck, D., Liou, K., Meng, C.-I. 2001, *Aurora conjugacy during substorms: Coordinated Antarctic ground and Polar ultraviolet observations*, J. Geophys. Res. 106, 24 579–24 591

Walt, M., Newkirk, L. L., Francis, W. E. 1979, *Bremsstrahlung produced by precipitating electrons*, J. Geophys. Res. 84, 967–973

Weimer, D. R. 2001, *Maps of ionospheric field-aligned currents as a function of the interplanetary magnetic field derived from Dynamics Explorer 2 data*, J. Geophys. Res. 106, 12 889–12 902

Winckler, J. R., Peterson, L. 1957, *Large auroral effect on cosmic-ray detectors observed at 8 g/cm^2 atmospheric depth*, Phys. Rev. 108, 903–904

Winckler, J. R., Peterson, L., Arnoldy, R., Hoffman, R. 1958, *X-rays from visible aurorae at Minneapolis*, Phys. Rev. 110, 1221–1231

Wu, Q., Rosenberg, T. J., Lanzerotti, L. J., Maclennan, C. G., Wolfe, A. 1991, *Seasonal and diurnal variation of the latitude of the westward auroral electrojet in the nightside polar cap*, J. Geophys. Res. 96, 1409–1419

DANISH METEOROLOGICAL INSTITUTE

Scientific Reports

Scientific reports from the Danish Meteorological Institute cover a variety of geophysical fields, i.e. meteorology (including climatology), oceanography, subjects on air and sea pollution, geomagnetism, solar-terrestrial physics, and physics of the middle and upper atmosphere.

Reports in the series within the last five years:

No. 97-1
E. Friis Christensen og C. Skøtt: Contributions from the International Science Team. The Ørsted Mission - a pre-launch compendium

No. 97-2
Alix Rasmussen, Sissi Kiilsholm, Jens Havskov Sørensen, Ib Steen Mikkelsen: Analysis of tropospheric ozone measurements in Greenland: Contract No. EV5V-CT93-0318 (DG 12 DTEE):
DMI's contribution to CEC Final Report Arctic Trophospheric Ozone Chemistry ARCTOC

No. 97-3
Peter Thejll: A search for effects of external events on terrestrial atmospheric pressure: cosmic rays

No. 97-4
Peter Thejll: A search for effects of external events on terrestrial atmospheric pressure: sector boundary crossings

No. 97-5
Knud Lassen: Twentieth century retreat of sea-ice in the Greenland Sea

No. 98-1
Niels Woetman Nielsen, Bjarne Amstrup, Jess U. Jørgensen: HIRLAM 2.5 parallel tests at DMI: sensitivity to type of schemes for turbulence, moist processes and advection

No. 98-2
Per Høeg, Georg Bergeton Larsen, Hans-Henrik Benzon, Stig Syndergaard, Mette Dahl Mortensen: The GPSOS project Algorithm functional design and analysis of ionosphere, stratosphere and troposphere observations

No. 98-3
Mette Dahl Mortensen, Per Høeg: Satellite atmosphere profiling retrieval in a nonlinear troposphere Previously entitled: Limitations induced by Multipath

No. 98-4
Mette Dahl Mortensen, Per Høeg: Resolution properties in atmospheric profiling with GPS

No. 98-5
R.S. Gill and M. K. Rosengren: Evaluation of the Radarsat imagery for the operational mapping of sea ice around Greenland in 1997

No. 98-6
R.S. Gill, H.H. Valeur, P. Nielsen and K.Q. Hansen: Using ERS SAR images in the operational mapping of sea ice in the Greenland waters: final report for ESA-ESRIN's: pilot projekt no. PP2.PP2.DK2 and 2nd announcement of opportunity for the exploitation of ERS data projekt No. AO2..DK 102

No. 98-7
Per Høeg et al.: GPS Atmosphere profiling methods and error assessments

No. 98-8
H. Svensmark, N. Woetmann Nielsen and A.M. Sempreviva: Large scale soft and hard turbulent states of the atmosphere

No. 98-9
Philippe Lopez, Eigil Kaas and Annette Guldberg: The full particle-in-cell advection scheme in spherical geometry

No. 98-10
H. Svensmark: Influence of cosmic rays on earth's climate

No. 98-11
Peter Thejll and Henrik Svensmark: Notes on the method of normalized multivariate regression

No. 98-12
K. Lassen: Extent of sea ice in the Greenland Sea 1877-1997: an extension of DMI Scientific Report 97-5

No. 98-13
Niels Larsen, Alberto Adriani and Guido DiDonfrancesco: Microphysical analysis of polar stratospheric clouds observed by lidar at McMurdo, Antarctica

No.98-14
Mette Dahl Mortensen: The back-propagation method for inversion of radio occultation data

No. 98-15
Xiang-Yu Huang: Variational analysis using spatial filters

No. 99-1
Henrik Feddersen: Project on prediction of climate variations on seasonel to interannual timescales (PROVOST) EU contract ENVA4-CT95-0109: DMI contribution to the final report:Statistical analysis and post-processing of uncoupled PROVOST simulations

No. 99-2
Wilhelm May: A time-slice experiment with the ECHAM4 A-GCM at high resolution: the experimental design and the assessment of climate change as compared to a greenhouse gas experiment with ECHAM4/OPYC at low resolution

No. 99-3
Niels Larsen et al.: European stratospheric monitoring stations in the Artic II: CEC Environment and Climate Programme Contract ENV4-CT95-0136. DMI Contributions to the project

No. 99-4
Alexander Baklanov: Parameterisation of the deposition processes and radioactive decay: a review and some preliminary results with the DERMA model

No. 99-5
Mette Dahl Mortensen: Non-linear high resolution inversion of radio occultation data

No. 99-6
Stig Syndergaard: Retrieval analysis and methodologies in atmospheric limb sounding using the GNSS radio occultation technique

No. 99-7
Jun She, Jacob Woge Nielsen: Operational wave forecasts over the Baltic and North Sea

No. 99-8
Henrik Feddersen: Monthly temperature forecasts for Denmark - statistical or dynamical?

No. 99-9
P. Thejll, K. Lassen: Solar forcing of the Northern hemisphere air temperature: new data

No. 99-10
Torben Stockflet Jørgensen, Aksel Walløe Hansen: Comment on "Variation of cosmic ray flux and global coverage - a missing link in solar-climate relationships" by Henrik Svensmark and Eigil Friis-Christensen

No. 99-11
Mette Dahl Meincke: Inversion methods for atmospheric profiling with GPS occultations

No. 99-12
Hans-Henrik Benzon; Laust Olsen; Per Høeg: Simulations of current density measurements with a Faraday Current Meter and a magnetometer

No. 00-01
Per Høeg; G. Leppelmeier: ACE - Atmosphere Climate Experiment

No. 00-02
Per Høeg: FACE-IT: Field-Aligned Current Experiment in the Ionosphere and Thermosphere

No. 00-03
Allan Gross: Surface ozone and tropospheric chemistry with applications to regional air quality modeling. PhD thesis

No. 00-04
Henrik Vedel: Conversion of WGS84 geometric heights to NWP model HIRLAM geopotential heights

No. 00-05
Jérôme Chenevez: Advection experiments with DMI-Hirlam-Tracer

No. 00-06
Niels Larsen: Polar stratospheric clouds microphysical and optical models

No. 00-07
Alix Rasmussen: "Uncertainty of meteorological parameters from DMI-HIRLAM"

No. 00-08
A.L. Morozova: Solar activity and Earth's weather. Effect of the forced atmospheric transparency changes on the troposphere temperature profile studied with atmospheric models

No. 00-09
Niels Larsen, Bjørn M. Knudsen, Michael Gauss, Giovanni Pitari: Effects from high-speed civil traffic aircraft emissions on polar stratospheric clouds

No. 00-10
Søren Andersen: Evaluation of SSM/I sea ice algorithms for use in the SAF on ocean and sea ice, July 2000

No. 00-11
Claus Petersen, Niels Woetmann Nielsen: Diagnosis of visibility in DMI-HIRLAM

No. 00-12
Erik Buch: A monograph on the physical oceanography of the Greenland waters

No. 00-13
M. Steffensen: Stability indices as indicators of lightning and thunder

No. 00-14
Bjarne Amstrup, Kristian S. Mogensen, Xiang-Yu Huang: Use of GPS observations in an optimum interpolation based data assimilation system

No. 00-15
Mads Hvid Nielsen: Dynamisk beskrivelse og hydrografisk klassifikation af den jyske kyststrøm

No. 00-16
Kristian S. Mogensen, Jess U. Jørgensen, Bjarne Amstrup, Xiaohua Yang and Xiang-Yu Huang: Towards an operational implementation of HIRLAM 3D-VAR at DMI

No. 00-17
Sattler, Kai; Huang, Xiang-Yu: Structure function characteristics for 2 meter temperature and relative humidity in different horizontal resolutions

No. 00-18
Niels Larsen, Ib Steen Mikkelsen, Bjørn M. Knudsen m.fl.: In-situ analysis of aerosols and gases in the polar stratosphere. A contribution to THESEO. Environment and climate research programme. Contract no. ENV4-CT97-0523. Final report

No. 00-19
Amstrup, Bjarne: EUCOS observing system experiments with the DMI HIRLAM optimum interpolation analysis and forecasting system

No. 01-01
V.O. Papitashvili, L.I. Gromova, V.A. Popov and O. Rasmussen: Northern polar cap magnetic activity index PCN: Effective area, universal time, seasonal, and solar cycle variations

No. 01-02
M.E. Gorbunov: Radioholographic methods for processing radio occultation data in multipath regions

No. 01-03
Niels Woetmann Nielsen; Claus Petersen: Calculation of wind gusts in DMI-HIRLAM

No. 01-04
Vladimir Penenko; Alexander Baklanov: Methods of sensitivity theory and inverse modeling for estimation of source parameter and risk/vulnerability areas

No. 01-05
Sergej Zilitinkevich; Alexander Baklanov; Jutta Rost; Ann-Sofi Smedman, Vasiliy Lykosov and Pierluigi Calanca: Diagnostic and prognostic equations for the depth of the stably stratified Ekman boundary layer

No. 01-06
Bjarne Amstrup: Impact of ATOVS AMSU-A radiance data in the DMI-HIRLAM 3D-Var analysis and forecasting system

No. 01-07
Sergej Zilitinkevich; Alexander Baklanov: Calculation of the height of stable boundary layers in operational models

No. 01-08
Vibeke Huess: Sea level variations in the North Sea – from tide gauges, altimetry and modelling

No. 01-09
Alexander Baklanov and Alexander Mahura: Atmospheric transport pathways, vulnerability and possible accidental consequences from nuclear risk sites: methodology for probabilistic atmospheric studies

No. 02-01
Bent Hansen Sass and Claus Petersen: Short range atmospheric forecasts using a nudging procedure to combine analyses of cloud and precipitation with a numerical forecast model

No. 02-02
Erik Buch: Present oceanographic conditions in Greenland waters

No. 02-03
Bjørn M. Knudsen, Signe B. Andersen and Allan Gross: Contribution of the Danish Meteorological Institute to the final report of SAMMOA. CEC contract EVK2-1999-00315: Spring-to.-autumn measurements and modelling of ozone and active species

No. 02-04
Nicolai Kliem: Numerical ocean and sea ice modelling: the area around Cape Farewell (Ph.D. thesis)

No. 02-05
Niels Woetmann Nielsen: The structure and dynamics of the atmospheric boundary layer

No. 02-06
Arne Skov Jensen, Hans-Henrik Benzon and Martin S. Lohmann: A new high resolution method for processing radio occultation data

No. 02-07
Per Høeg and Gottfried Kirchengast: ACE+: Atmosphere and Climate Explorer

No. 02-08
Rashpal Gill: SAR surface cover classification using distribution matching

No. 02-09
Kai Sattler, Jun She, Bent Hansen Sass, Leif Laursen, Lars Landberg, Morten Nielsen og Henning S. Christensen: Enhanced description of the wind climate in Denmark for determination of wind resources: final report for 1363/00-0020: Supported by the Danish Energy Authority

No. 02-10
Michael E. Gorbunov and Kent B. Lauritsen: Canonical transform methods for radio occultation data

No. 02-11
Kent B. Lauritsen and Martin S. Lohmann: Unfolding of radio occultation multipath behavior using phase models

No. 02-12
Rashpal Gill: SAR image classification using fuzzy screening method

No. 02-13
Kai Sattler: Precipitation hindcasts of historical flood events

No. 02-14
Tina Christensen: Energetic electron precipitation studied by atmospheric x-rays